Forschungsbericht 2014-22

Analysis of aerosol-cloud-interactions over semi-arid and arid subtropical land regions from three different satellite datasets (MODIS, AATSR/ENVISAT, IASI)

Lars Klüser

Deutsches Zentrum für Luft- und Raumfahrt
Deutsches Fernerkundungsdatenzentrum
Oberpfaffenhofen

DLR Deutsches Zentrum für Luft- und Raumfahrt

Herausgeber

Deutsches Zentrum
für Luft- und Raumfahrt e.V.
Bibliotheks- und
Informationswesen
D-51170 Köln
Porz-Wahnheide
Linder Höhe
D-51147 Köln

Telefon (0 22 03) 6 01- 44 44
Telefax (0 22 03) 6 01- 47 47

ISSN 1434-8454

Aerosol-Wolken-Wechselwirkungen, IASI, Wolken, Mineralstaub

Lars KLÜSER
Deutsches Fernerkundungsdatenzentrum, Oberpfaffenhofen

Analyse von Aerosol-Wolken-Wechselwirkungen über semiariden und ariden subtropischen Landgebieten mittels dreier verschiedener Satellitendatensätze (MODIS, AATSR/ENVISAT, IASI)

(veröffentlicht in englischer Sprache)

Dissertation Universität Augsburg
DLR-Forschungsbericht 2014-22, 2014, 113 Seiten, 40 Abbildungen, 18 Tabellen, 206 Literaturstellen, 24.00 €

Indirekte Aerosoleffekte stellen eine der größten Unsicherheiten im derzeitigen Verständnis des Klimasystems dar. Drei verschiedene Satellitendatensätze wurden verwendet, um Aerosol-Wolken-Wechselwirkungen über semiariden und ariden Landgebieten zu analysieren. Ein neuentwickeltes Verfahren zur statistischen Berücksichtigung von Änderungen in der Wolkentemperatur und deren Einfluss auf die Wolkeneigenschaften sowie eine neuentwickelte Methode zur Ableitung von Mineralstaub- und Eiswolkeneigenschaften aus IASI Daten erlauben die Gewinnung weiterer Informationen bezüglich der Aerosoltyp-Abhängigkeit von Aerosol-Wolken-Wechselwirkungen. Für Flüssigwasserwolken wurde der erste indirekte Aerosoleffekt bestätigt. Dieselben Effekte wie für Flüssigwasserwolken wurden auch für Eiswolken gefunden.

Aerosol-cloud-interactions, IASI, clouds, mineral dust

Lars KLÜSER
Deutsches Fernerkundungsdatenzentrum, Oberpfaffenhofen

Analysis of aerosol-cloud-interactions over semi-arid and arid subtropical land regions from three different satellite datasets (MODIS, AATSR/ENVISAT, IASI)

Doctoral Thesis Universität Augsburg
DLR-Forschungsbericht 2014-22, 2014, 113 pages, 40 figs., 18 tabs., 206 refs., 24.00 €

Indirect aerosol effects have been identified as one of the largest uncertainties in the current understanding of the climate. Aerosol cloud interactions over arid and semi-arid land regions have been analysed from three different satellite datasets with respect to aerosol type and cloud phase. A newly developed method to account for variations in cloud top temperature affecting cloud property observations statistically As well as a newly developed dataset from IASI which is sensitive to desert dust and ice clouds only add information about aerosol type sensitivity of aerosol-cloud interactions. For liquid water clouds the first indirect aerosol could be confirmed. For ice phase clouds the same effects as for liquid water clouds are observed.

Forschungsbericht 2014-22

Analysis of aerosol-cloud-interactions over semi-arid and arid subtropical land regions from three different satellite datasets (MODIS, AATSR/ENVISAT, IASI)

Lars Klüser

Deutsches Zentrum für Luft- und Raumfahrt
Deutsches Fernerkundungsdatenzentrum
Oberpfaffenhofen

113 Seiten
40 Bilder
18 Tabellen
206 Literaturstellen

Deutsches Zentrum
DLR für Luft- und Raumfahrt

Institut für Physik
Mathematisch-Naturwissenschaftliche Fakultät
Universität Augsburg

Dissertation
zur Erlangung des Doktorgrades
der Mathematisch-Naturwissenschaftlichen Fakultät
der Universität Augsburg

Analysis of aerosol-cloud-interactions over semi-arid and arid subtropical land regions from three different satellite datasets (MODIS, AATSR/ENVISAT, IASI)

vorgelegt von

Lars Klüser

Dezember 2013

angefertigt am
Deutschen Zentrum für Luft- und Raumfahrt
Oberpfaffenhofen

Gutachter:
Prof. Dr. Michael Bittner
Prof. Dr. Siegfried Horn

Tag der mündlichen Prüfung:
24. April 2014

Abstract

Indirect aerosol effects, i.e. the change of cloud physical properties by aerosol interactions, have been identified as one of the largest uncertainties in the current understanding of the climate system. Despite the uncertainties of the representations of aerosol-cloud interactions in current climate projections, they have large impact on the climate system itself – in terms of the radiation balance, but also in terms of precipitation, and thus vegetation cover, and re-distribution of water throughout the atmosphere. Nevertheless, so far only very few studies of large-scale statistics of aerosol-cloud interactions over land are available. Moreover most studies on the topic cover liquid water clouds only.

Aerosol cloud interactions over arid and semi-arid land regions have been analysed from three different satellite datasets with respect to aerosol type and cloud phase. The regions of the analysis cover Southern Africa, the Sahel domain with the influence of the West African monsoon circulation, the North-Western African Maghreb region and the Arabian Peninsula. These regions have been chosen as they are dominated by one (Maghreb, Arabia) or two (Sahel, Southern Africa) aerosol types and as mineral dust is one of the dominating aerosol types in all of them. The second dominating aerosol type is biomass burning in the Sahel and Southern Africa. These aerosol types can be discriminated by separating the aerosol information into fine mode (biomass burning) and coarse mode (desert dust) aerosol. Thus they can generally also be discriminated from satellite, although these capabilities are limited over land. Over land the diurnal cycle of convection is much stronger and aerosol interactions with deep convective cloud systems over land have been identified to be of great importance not only for precipitation in regions under pressure of desertification, but also with respect to climate change.

For liquid water clouds the well-known first indirect aerosol effect (“Twomey effect”), i.e. higher cloud albedo due to smaller droplet sizes, could be confirmed for all regions, if liquid water path is held constant. Nevertheless, liquid water path has been found to be affected by aerosol presence and the aerosol effect on liquid water path dominates the net effect of aerosols on cloud optical depth. For ice phase clouds the same effects are observed with ice water path controlling the net aerosol effect on optical depth. From thermal infrared retrievals of mineral dust and ice clouds an increase of ice particle size with respect to background conditions has been detected. Together with observations at solar wavelengths the differences can be interpreted as indications for an increase of optically thicker clouds at the cost of cirrus coverage. Although the Twomey effect has been identified to be active in all cases, cloud water path and cloud phase transitions could be identified to be of predominant importance for resulting cloud propertiy changes due to aerosol presence.

The second indirect aerosol effect (“Albrecht effect”) could not be identified from the statistical analysis. Although cloud cover distributions as functions of aerosol optical depth (AOD) indicate an increase of cloud cover with AOD, these could not be related to any other cloud properties including cloud droplet size. Thus the satellite observations do not support the relatively simple formulation of the second indirect aerosol effect (longer cloud lifetime due to drizzle suppression as a consequence of smaller droplets). An aerosol effect on cloud phase has been identified with respect to cloud water path. It could not be confirmed in terms of cloud coverage.

The statistical analysis of cloud macro- and microphysical properties has been performed after the observations have been projected all to the same cloud top temperature distribution. This method allows correcting for effects of the temperature

and moisture fields (meteorological conditions), which otherwise would dominate the statistical results.
It has been shown that aerosol type is important for aerosol cloud interactions in subtropical land regions. Moreover the cloud water path (liquid and ice) has been identified to be a strong constraint on indirect aerosol effects, outweighing e.g. the optical depth increase by droplet size reduction ("Twomey-effect"). It could moreover be shown that aerosol-cloud interactions are also important for ice cloud properties in subtropical land regions, which have yet not fully been addressed in statistical analyses of indirect aerosol effects and consequently in climate projections. Nevertheless, by means of the large-scale statistical analysis, also some deficits of current satellite datasets have been identified, which have to be solved in order to furthermore reduce the uncertainties of indirect aerosol effects.
It has been the first attempt to quantify aerosol-cloud interactions focussed on semi-arid and arid land regions, performing the same kind of analysis to liquid water and ice clouds at the same time with the same methods, comparing results from three different independent satellite datasets, using advanced statistical descriptions of the observed deviations from background in order to account for non-linearity and multimodal or non-Gaussian probability distributions of cloud properties, applying a newly developed method to account for variations in cloud top temperature affecting cloud property observations statistically and also introducing a newly developed dataset from IASI which is sensitive to desert dust and ice clouds only, adding information about aerosol type sensitivity of aerosol-cloud interactions.

Contents

List of figures

List of tables

1 Introduction

"*When we realize that it is possible to produce self-propagating rain or snow storms by artificial nucleation and that similar effects can be produced spontaneously by chain reactions that begin at particular but unpredictable times and places, it becomes apparent that important changes in the whole weather map can be brought about by events which are not at present being considered by meteorologists. We must recognize that it will probably forever be impossible to forecast with any great accuracy weather phenomena that may have beginnings in such spontaneously generated chain rections.*"

from *Langmuir* (1948)

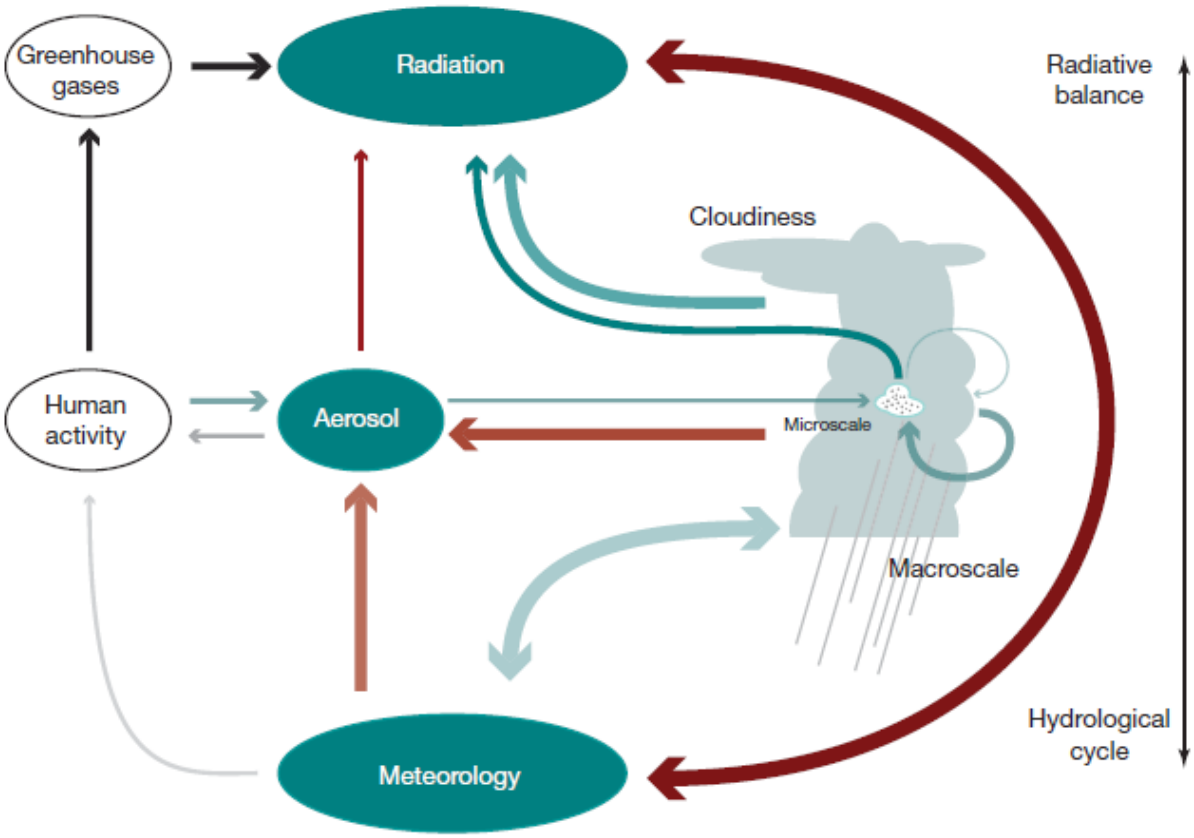

Fig. 1: Schematic overview over aerosol-cloud-interactions in the context of the atmospheric component of the climate system (from *Stevens and Feingold*, 2009).

Aerosols, solid or liquid particles except hydrometeors (cloud droplets or ice crystals) which are suspended in the air, are necessary for the generation of clouds and thus of precipitation – which means redistribution of water. Consequently aerosols play a very important role in the atmospheric branch of the climate system (*Stevens and Feingold*, 2009). Fig. 1 shows an overview of aerosol-cloud-interactions in the climate system and their impact on the hydrological cycle and the radiation balance. This is since long well known in atmospheric sciences. As early as 1948 Irving Langmuir

reported contradictory effects, which artificial aerosol injections into clouds can have. More than 60 years later the topic of cloud property modification by aerosol still attracts scientific interest (*Stevens and Feingold*, 2009).

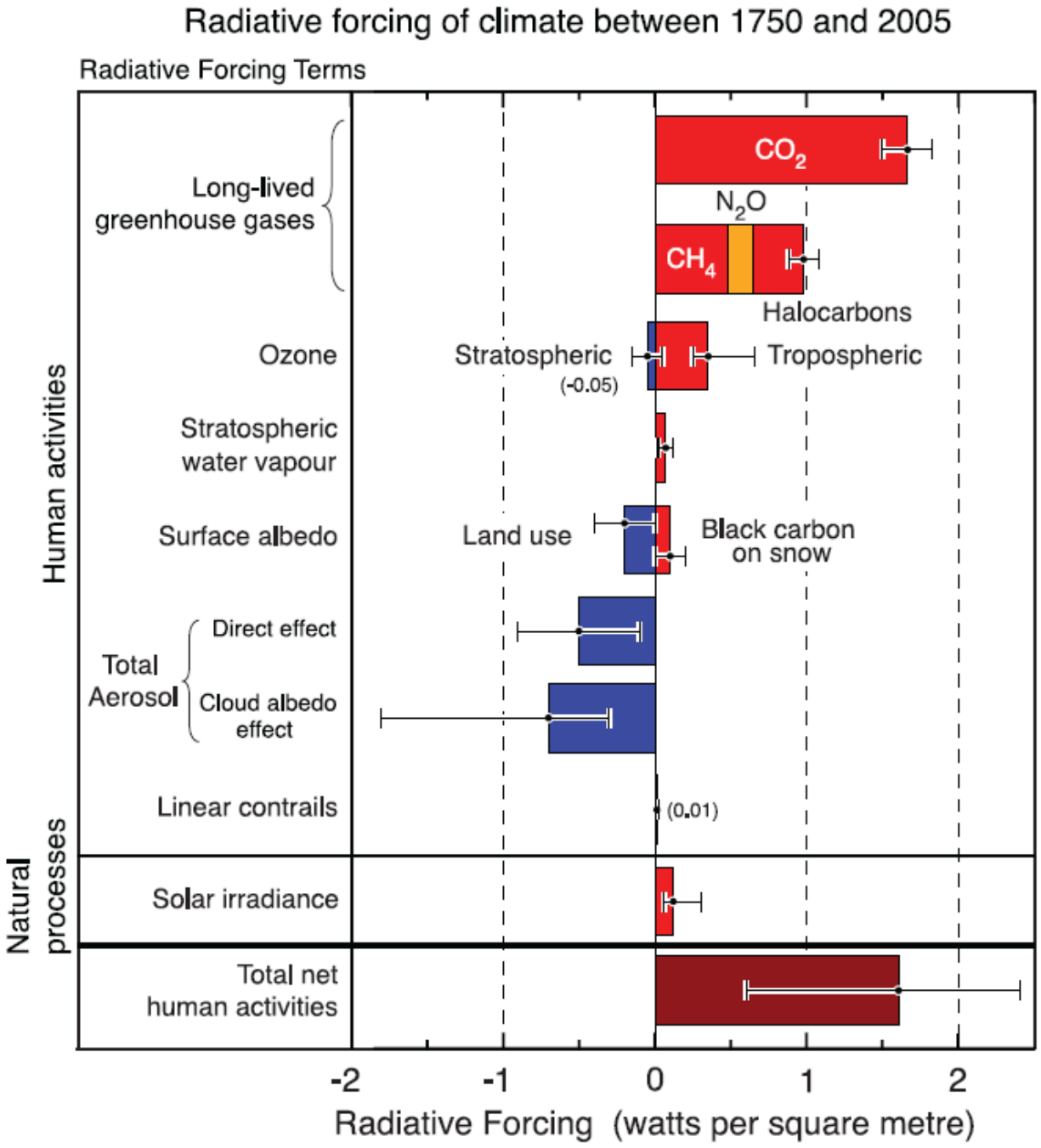

Fig. 2: Radiative forcing of several climate system variables. Aerosol effects on the radiative forcing included in the analysis of the fourth IPCC assessment report have large uncertainties and include only cloud albedo effects as indirect aerosol effect (from *IPCC*, 2007).

The intergovernmental panel for climate change (IPCC) stated in its Fourth Assessment Report (AR4: *IPCC*, 2007) that aerosol-cloud interactions are still one of the major uncertain issues when adressing climate change projection for future scenarios (fig. 2). It is noteworthy that the report only deals with the effect of aerosols

on cloud albedo – the one indirect aerosol effect which has to be regarded as the one best understood. The reported consequences are widespread and the uncertainty in climate modelling also increases the uncertainty in usefulness of mitigation strategies (*IPCC*, 2007). During the last decade the effects of increased aerosol concentrations on several components of the climate system have been adressed by the scientific community (*Ramanathan et al.*, 2001; *Kaufman et al.*, 2002; *IPCC*, 2007). These effects are, besides direct radiative forcing by reflection and absorption of solar radiation (*Ramanathan et al.*, 2001; *IPCC*, 2007), mainly impacts on cloud microphysical properties and thus cloud radiative forcing (called indirect aerosol effects, e.g. *King et al.*, 1999; *Rosenfeld et al.*, 2001; *Kaufman et al.*, 2002). Also effects on the hydrological cycle through modification of the precipitation efficiency have been controversely discussed (*Ramanathan et al.*, 2001; *Rosenfeld et al.*, 2001; *IPCC*, 2007; *Stevens and Feingold*, 2009; *Perlwitz and Miller*, 2010). Although the importance of aerosol cloud interactions is well known there has been only little advance in reducing the uncertainties connected to indirect aerosol effects (*IPCC*, 2001, 2007). One reason is that the net effect of aerosols on clouds and cloud properties is subject to several counteracting aerosol effects (e.g. *Stevens and Feingold*, 2009; *Carslaw et al.*, 2010; *Perlwitz and Miller*, 2010).

Moreover, also the chemical composition of the atmospheric aerosol (aerosol type) influences magnitude and also sign of the respective aerosol effects (e.g. *Ramanathan et al.*, 2001; *Perlwitz and Miller*, 2010). In order to separate the effects of different aerosol types on cloud properties there is thus a need for a differentiation of aerosol types in retrieved aerosol parameters. So far, many observations of aerosol cloud interactions, either ground based or from satellite, do not include variations of aerosol type (e.g. *Lohmann and Feichter*, 2005). It is widely assumed that aerosols suppress precipitation by reduction of cloud droplet sizes (*Rosenfeld et al.*, 2001; *Ramanathan et al.*, 2001; *Lohmann and Feichter*, 2005; *Carslaw et al.*, 2010). Nevertheless the same effect can trigger extreme precipitation events later or elsewhere (*Stevens and Feingold*, 2009) as has already been described by *Langmuir* (1948). Verification of this assumption would, besides accurate precipitation observations, need proper separation of aerosol type (e.g. *Feingold et al.*, 1999; *Ramanathan et al.*, 2001). This has partly been done over ocean (e.g. *Dunion and Velden*, 2004; *Kaufman et al.*, 2005) but hardly over land.

Aerosol type retrieval needs several observations (e.g. at different wavelengths), which have to represent different aerosol types. Such observations are mostly not sufficiently available to completely constrain the ill-posed retrieval problem from many satellite instruments – thus aerosol type retrieval is very difficult.

Although long term time series of reliable cloud observations with satellite date back to the late 1970s, when the first TIROS-N satellite carrying the Advanced Very High Resolution Radiometer (AVHRR) was launched by the US National Oceanic and Atmosphere Administration (NOAA), the reliability of cloud trend analysis from the AVHRR time series has been questioned in recent years (*Evan et al.*, 2007). The main reasons for this concern are the changes in satellite orbits leading to different observation hours. In regions with predominantly convective cloud development this means a change in observed cloud life cycle phase and the observed trend may reflect the change in orbital configuration rather than a physical change in cloud properties (*Evan et al.*, 2007).

The upcoming of observations with the MODerate resolution Imaging Spectro-radiometer (MODIS) and comparable multispectral satellite instruments, about 15 years ago, boosted the availability of observations which in general are capable of qualitative aerosol type separation, at least into two classes. From MODIS

observations aerosol retrieval is also possible over bright reflecting surfaces (*Hsu et al.*, 2004). The European environmental research satellite ENVISAT with a very large payload of instruments dedicated to several earth observation aspects allows exploiting the synergy of the spectrometer SCIAMACHY (Scanning Imaging Absorption Spectrometer for Atmospheric CHartographY) and the Advanced Along Track Scanning Radiometer (AATSR) with novel capabilities for the determination of the aerosol mixture present in the observed scene (*Holzer-Popp et al.*, 2008). The launch of the European Metop satellite in 2006 again was a step forward in remote sensing of the atmosphere, as the payload includes the Infrared Atmospheric Sounding Interferometer (IASI), a new generation of infrared sounding instrument with unpredecented spectral resolution and stability (e.g. *Larar et al.*, 2010). Radiance spectra from IASI can be exploited for mineral dust and ice cloud retrieval independently from solar illumination, thus doubling the observation rate compared to solar wavelength retrievals.

By now satellite instruments have provided datasets large enough for statistical assessment of aerosol cloud interactions over land – also with separation of the observations by aerosol type.

Stevens and Feingold (2009) suggest investigating aerosol-cloud interactions with special focus on cloud lifetime effects in different cloud regimes. Semiarid regions, especially those of Africa, are especially vulnerable to climate change due to strong gradients in water supply and also due to more frequent cultivation of grazing land (e.g. *Jalloh et al.*, 2011). They are influenced by the seasonal intrusion of moist air and accompanying precipitation and long dry seasons in between (e.g. *N'Tchay Mbourou et al.*, 1997). Consequently there is a large interest in understandig aerosol impacts on the different cloud parameters of this specific cloud regime, which will be analysed here. Moreover, due to different hygroscopicity of mineral dust and biomass burning aerosols, especially cloud lifetime effects are suspected to be sensitive to aerosol type. It is currently discussed, which indirect aerosol effects are the most important and how satellite observations of aerosol – cloud cover relationships are to be interpreted (e.g. *Stevens and Feingold*, 2009; *Small et al.*, 2011).

Methods of large-scale (in both, time and space) statistical analysis are applied to different satellite datasets of aerosol and cloud observations in order to assess several impacts of the aerosol concentrations on the cloud state over semi-arid and arid land regions. The results are also used to address indirect aerosol effects on ice clouds, which e.g. are currently not part of the IPCC projections and also to address type dependent aerosol effects.

2 Radiative transfer and remote sensing

Atmospheric constituents can affect the field of electromagnetic radiation mainly by scattering and absorption. Both are summarized as extinction. Solar radiation is scattered by clouds and aerosols and absorbed by water vapour, other trace gases and aerosols. Terrestrial or thermal infrared (IR) radiation (defined here as radiation with wavelengths between 4µm and 50µm following *Petty*, 2006) is scattered or absorbed by mainly silicate dust aerosols and also by clouds, water vapour and other trace gases.
If an extincting (scattering and / or absorbing) medium is characterized by density ρ_m (of gases, cloud droplets or aerosol particles) and the respective mass extinction coefficient k_e at any distance s from the emission source of the radiation the coefficient of extinction is given by

$$\beta_e(s) = \rho_m(s) \cdot k_e \qquad (1)$$

Then radiation of wavelength λ and intensity I propagating through an extincting medium like the atmosphere along the path s with lengths s_1 is attenuated as following

$$I_\lambda(s_1) = I_\lambda(0) e^{-\left(\int_0^{s_1} \beta_e(s) ds\right)} \qquad (2)$$

The integral on the right hand side of eq. (2) is called optical path (sometimes also called optical thickness, but as many authors confuse optical depth and optical thickness, the wording optical path is used here). The vertical optical path, observed along the vertical coordinate z, is the optical depth and thus is defined as

$$\tau = \int_0^{z_1} \beta_e dz \qquad (3)$$

Unlike for clouds, in the case of extinction by aerosols, this quantity most often is denoted as “aerosol optical depth” (AOD). If not declared otherwise, optical depth (for aerosol and clouds) corresponds to a wavelength of 0.55µm (which is the peak wavelength of the Planck-function for solar radiation, e.g. *Petty*, 2006). In infrared spectroscopy quite often wavenumber ν is used for spectral characterisation instead of wavelength λ ($\nu=1/\lambda$).
Thermal infrared radiation is absorbed and also scattered by clouds (for clouds absorption is much stronger then scattering, e.g. *Petty*, 2006). For sufficently high optical depth (τ>10, *Comstock et al.*, 2007) clouds can be assumed as opaque and thus as black bodies in the thermal infrared spectral range (*Petty*, 2006; *Comstock et al.*, 2007). Thus the radiation observed by satellites above cloud tops mainly represents the radiation emitted by the uppermost layer of the cloud, depending on its temperature. This temperature is called cloud-top-temperature (CTT). Radiance observations of satellite instruments are converted into brightness temperature, also called equivalent blackbody temperature, either by inversion of the Planck function at the sensor’s channel central wavelength (*Kidder and Vonder Haar*, 1995; *Petty*, 2006) or by statistical fit models of band integrals of the Planck function taking into account the bandwidth of the instrumental channel. Brightness temperatures of the

atmospheric window spectral region (8-12µm) can be regarded as first-order estimates for the cloud top temperature of opaque clouds (e.g. *Rosenfeld and Lensky*, 1998). More sophisticated cloud property retrieval schemes like e.g. the APOLLO (Avhrr Processing over Land, cLouds and Ocean) scheme, which is also used here, use infrared estimates of the cloud top emissivity to correct for the grey emission of the cloud top in order to retrieve CTT (*Saunders and Kriebel*, 1988; *Kriebel et al.*, 1989; *Kriebel et al.*, 2003).
Cloud cover information is retrieved from a set of instrument channel observations covering both the solar and the thermal infrared spectral range. Most cloud screening algorithms like the APOLLO and the MODIS retrievals used here, consist of a range of threshold tests for solar channel reflectance, thermal channel brightness temperature and brightness temperature difference (BTD) between two IR channels (e.g. *Saunders and Kriebel*, 1988; *Kriebel et al.*, 1989; *Kriebel et al.*, 2003; *Holzer-Popp et al.*, 2008).
The cloud phase can be determined either by a reflectance ratio of solar channels with and without ice absorption (*King et al.*, 1997) or, as most often is done, by infrared brightness temperature tests and the difference of brightness temperatures in channels with weaker and stronger ice absorbtion (e.g. *King et al.*, 1997; *Chylek et al.*, 2006).
From (passive) satellite remote sensing it is not possible to infer the size distribution of cloud droplets for any cloud. Consequently a measure of droplet size is needed which characterizes the distribution and which can be obtained from remote sensing.
Cloud water density ρ_w is derived from the droplet size distribution n(r), the density of liquid water ρ_l and the volume of the droplets $4/3\pi(r_{md})^3$:

$$\rho_w = \int_0^\infty n(r') \frac{4\pi}{3} r'^3 \rho_l dr' \tag{4}$$

while the volume extinction coefficient β_e is given by

$$\beta_e = \int_0^\infty n(r') Q_e(r') \pi r'^2 dr' \tag{6}$$

with size dependent extinction efficiency $Q_e(r)$.
Consequently the mass extinction coefficient determined from β_e/ρ_w (eq. (1)) can be formulated as

$$k_e = \frac{\beta_e}{\rho_w} = \frac{\int_0^\infty n(r) \left[Q_e(r) \pi r^2 \right] dr}{\int_0^\infty n(r) \left[\rho_w \frac{4\pi}{3} r^3 \right] dr} \tag{7}$$

For liquid cloud droplets Q_e can be approximated as $Q_e \approx 2$ (*Petty*, 2006) and eq. (7) simpifies to

$$k_e \approx \frac{3}{2\rho_l r_e} \tag{8}$$

when the effective radius r_e is defined as:

$$r_e = \frac{\int_0^\infty r^3 n(r) dr}{\int_0^\infty r^2 n(r) dr} \quad (9)$$

Equation (9) is the common definition of effective radius as the ratio of third and second moment of the droplet size distribution which is widely used in remote sensing and can be infered directily from the mass extinction coefficient for spherical liquid water cloud droplets. The effective radius is the size parameter for cloud droplets and ice crystals, which is most often retrieved in remote sensing, as radiative transfer is sensitive to the integrated extinction coefficient. One very popular approach of determining cloud optical depth (τ_c) and effective radius (r_e) simultaneaously from satellite observations is the method of *Nakajima and King* (1990).

Orignally described for water clouds only, the *Nakajima and King* (1990) method exploits cloud reflectance at two different wavelengths in the visible and the near-infrared (mostly at 1.6µm or 2.2µm) range. From radiative transfer simulations theoretical reflectance distributions depending on optical depth and effective radius can be calculated (fig. 3). These are then converted into look-up tables for retrieving optical depth and effective radius from a given pair of observed reflectance in the two channels. It is evident that for small optical depth the results become less well-defined, the same is true for very small effective radius. Thus in those cases results a Nakajima/King-type retrieval scheme for optical depth and effective radius will have very high uncertainties. The same methodology can in general also be applied for ice clouds. But while liquid water droplets can be approximated very well as spheres, ice crystals form a large variety of regular and irregular shapes. Thus the radiative transfer calculations also have to account for shape effects of ice crystals (e.g. *Yang and Liou*, 1995).

Also the definition of an ice crystal effective size parameter differs from method to method (*King et al.*, 1997; *McFarquhar and Heymsfield*, 1998; *Yang et al.,* 2005).

For example, *King et al.* (1997) define an effective diameter for ice crystals similarly to *Fu and Liou* (1993) as

$$D_e(L) = \frac{\int_0^\infty LD^2 n(L) dL}{\int_0^\infty LDn(L) dL} \quad (10)$$

where D and L denote the width and the maximum dimension (length in the case of e.g. columns) of the ice crystals, respectively, while n(L) is the size distribution as a function of L.

As they consider a wide range of possible shapes in ice clouds, *Yang et al.* (2005) use another definition for an effective particle size of individual ice crystals, following *Ebert and Curry* (1992):

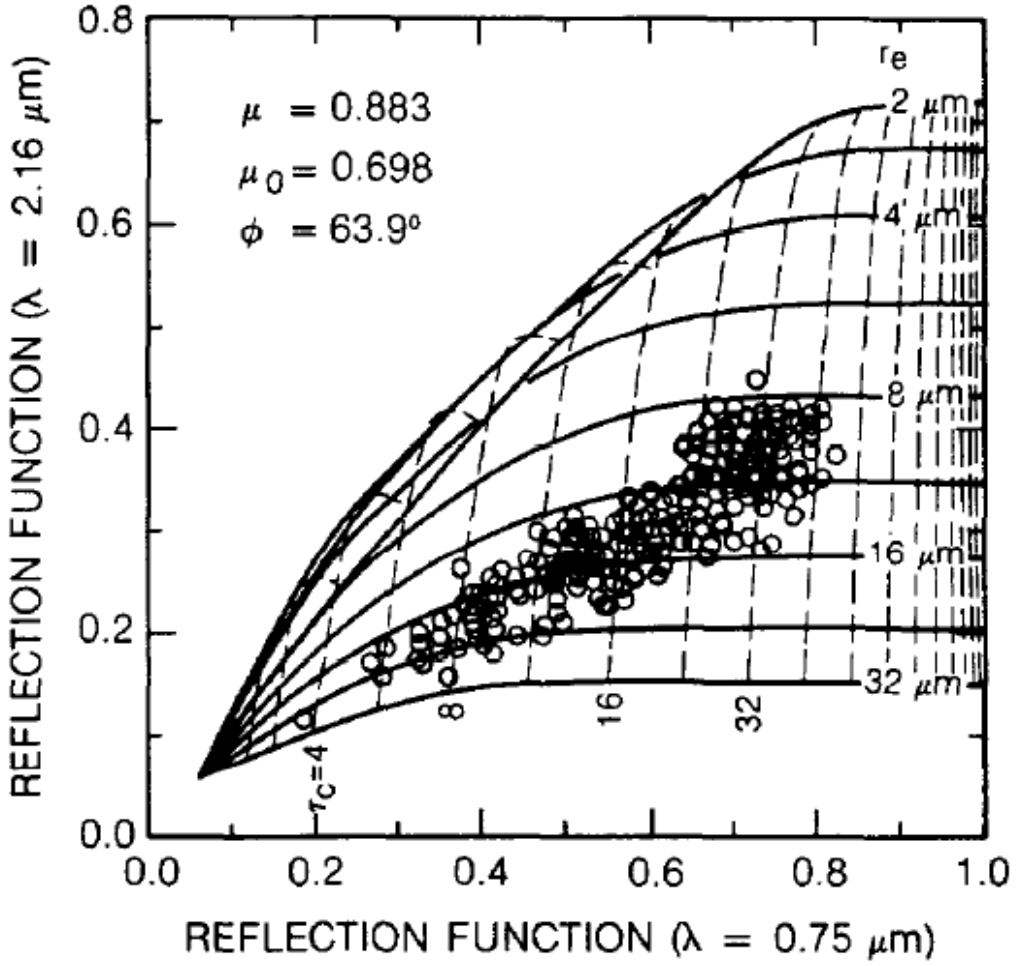

Fig. 3: Reflection at two different wavelengths from stratocumulus water clouds together with isolines for cloud optical depth and effective radius (from *Nakajima and King*, 1990) for given geometry (μ: cosine of viewing angle; μ_0: cosine of sun zenith angle; ϕ: azimuth angle).

$$D_e(L) = \frac{3v(L)}{2a(L)} \qquad (11)$$

L has the same respresentation as in eq. (10) while v and a are the projected area and the volume of the particle, respectively. The effective diameter (or radius) for a population of ice crystals can then be calculated from the effective size (or radius) of the single particles with eq. (11).

Comparisons of *McFarquhar and Heymsfield* (1998) show that the effective diameter definition used by *King et al.* (1997) will result in lower effective diameter than that of *Yang et al.* (2005) for randomly oriented hexagonal columns.

Remote sensing of tropospheric aerosols requires somewhat different retrieval schemes, as they most often have much lower optical depth than clouds. Consequently, they have higher transmittance and thus the radiation observed by satellite transports a strong signal of the underlying ground. Moreover, atmospheric aerosols are very inhomogeneous in terms of particle shape and chemical composition. Thus, each aerosol particle has distinct scattering and absorption properties and treatment in radiative transfer becomes much more complicated than for spherical water droplets. Consequently, for radiative transfer calculations bulk

optical properties of aerosol types (consisting of a variety of species) are applied (*Kokhanovsky and de Leeuw*, 2009)

Aerosol remote sensing over land is furthermore complicated by the highly variable contribution of land surface reflectance to the radiance observed from space. This is of special importance in single-view methods as those used here. Most common is the restriction of retrieval to dark surfaces where the background signal is suffiently small and the aerosol reflectance signal is a major contribution to the observed radiance ("dark target" methods).

Especially for remote sensing of mineral dust other methods have to be added, as dust often is observed over surfaces where "dark target assumptions" as made in many aerosol retrieval schemes do not hold (*Engelstaedter et al.*, 2006; *Kokhanovsky and de Leeuw*, 2009). This disadvantage can be overcome by applying other methods to the aerosol remote sensing data. One of these is the "Deep Blue" method originally developped for the Sea-viewing Wide Fields-of-view Sensor (SeaWiFS) and also applied to MODIS observations (*Hsu et al.*, 2004). It adds observations in the blue portion of the spectrum (at 0.412µm) to the retrieval process. At this wavelength the sensitivity to airborne aerosols is sufficiently high and surface reflectance is quite low also over bright reflecting (desert) surfaces (*Hsu et al.*, 2004; *Kokhanovsky and de Leeuw*, 2009).

In contrast to fine particle aerosols mineral dust also affects thermal infrared observations within the atmospheric IR window between 8µm and 12µm (interrupted by strong O_3 absorption at 9.6µm). Almost all silicate minerals, from which desert dust mostly is composed, show an absorption peak due to a vibrational resonance band of Si-O around 9.5µm. The shoulders of this absorption band reach far into the atmospheric window region not affected by the O_3 absorption (e.g. *Hudson et al.*, 2008a,b). Also some carbonaceous minerals like calcite ($CaCO_3$) present in desert dust have absorption bands in the atmospheric window region (*Hudson et al.*, 2008a). Thus dust remote sensing is also possible with thermal infrared methods (e.g. *Shenk and Curran*, 1974; *Ackerman*, 1997; *Legrand et al.*, 2001; *Evan et al.*, 2006; *Rosenfeld and Lensky*, 2008).

3 Cloud physics and indirect Aerosol effects

3.1 Cloud microphysics

Shape, thermodynamical phase, internal composition and sizes of cloud droplets or (ice) crystals are summarized as the cloud microphysical properties. In the case of water clouds without any frozen fraction it is sufficient to know the droplet size distribution n(r). It is mainly a function of moisture, temperature, availability of cloud condensation nuclei (CCN) and vertical velocity. These parameters are highly variable on a broad sale in time and space. Thus every cloud element is the result of the historical development of its environmental conditions.
From the knowledge of the droplet size distribution integral parameters can be calculated, as the droplet number density N_d, the effective radius and the cloud optical depth (*Pruppacher and Klett*, 1996). When cloud optical depth τ and effective radius r_e are known and spherical droplets with liquid water density ρ_l are assumed, liquid water path (LWP) can be calculated as

$$LWP = \frac{2}{3} \tau \, r_e \, \rho_l \qquad (12)$$

(follows directly from eq. (8), *Petty*, 2006), a way in which LWP is very often determined in remote sensing of clouds from solar radiation. Ice water path (IWP) is determined in the same way with corrections for deviations from the spherical model (e.g. *McFarquhar and Heymsfield*, 1998).
Aerosols and clouds are tightly connected, as the development of cloud droplets depends on the availability of CCN. The amount, size and chemical composition of the CCN determine the rate of super- (or sub-) saturation needed for water vapour condensing on the aerosol or droplet surface ("Raoult" effect, e.g. *Pruppacher and Klett*, 1996; *Laaksonen et al.*,1998). The traditional Köhler theory describes the equilibrium water vapour pressure over growing cloud droplets. Moreover it defines whether or not a droplet is “activated” and thus will grow further spontaneously (*Laaksonen et al.*, 1998). The Köhler theory directly describes the dependence of cloud droplet growth on single aerosol particle (CCN) size and solubility.
Within clouds supercooled liquid droplets of down to -40°C have been observed, normally freezing sets in at temperatures of about -10°C to -15°C (*Langmuir*, 1948; *Haman*, 1976; *Givati and Rosenfeld*, 2004). This occurence of supercooled liquid water can be explained by a lack of suitable ice nucei (IN), which are needed for cloud droplet freezing. At the same humidity over ice particle surfaces supersaturation is larger than over water droplet surfaces (*Langmuir*, 1948) . Thus at suitable humidity levels the ice particles grow at the cost of liquid water droplets reaching large (ice) particle sizes very fast (this is called the "Bergeron-Findeisen" process: *Bergeron*, 1933; *Findeisen*, 1938). These ice particles can rapidly grow sufficiently large to start precipitation.

3.2 Aerosol effects on cloud droplet size

In the case of a high amount of available CCN (polluted conditions), not all cloud droplets grow as Köhler theory would suggest (*Pruppacher and Klett*, 1996). *Warner and Twomey* (1967) and *Warner* (1968) describe the effect that in high levels of pollution (aerosol amount) very small cloud droplets are observed (frequently reported from observations in soot plumes in Australia). There are several reasons

for this behaviour. One is the amount of available water vapour for condensation. It is obvious that the level of super- (or sub-) saturation, expressed as the ratio of available moisture and moisture saturation level resulting from the temperature of the ambient air, strongly depends on the meteorological conditions (moisture supply). Thus, it also depends on the water vapour partial pressure present in the cloud environment (*Pruppacher and Klett*, 1996). As more water vapour condenses, the partial pressure decreases and the equilibrium conditions change. Consequently the amount of condensed water vapour is assumed to stay constant even with more cloud droplets being pesent (*Kaufman et al.*, 2002). Moreover, additionally to cloud droplet growth following Köhler theory, also the collision of cloud droplets changes the droplet size distribution. Coalescence is very important for the formation of large and giant cloud droplets suitable for forming precipitation (*Pruppacher and Klett*, 1996; *Riemer and Wexler*, 2005). Smaller cloud droplets have lower coalescence effectivity (*Gillespie*, 1972; *Ramanathan et al.*, 2001).

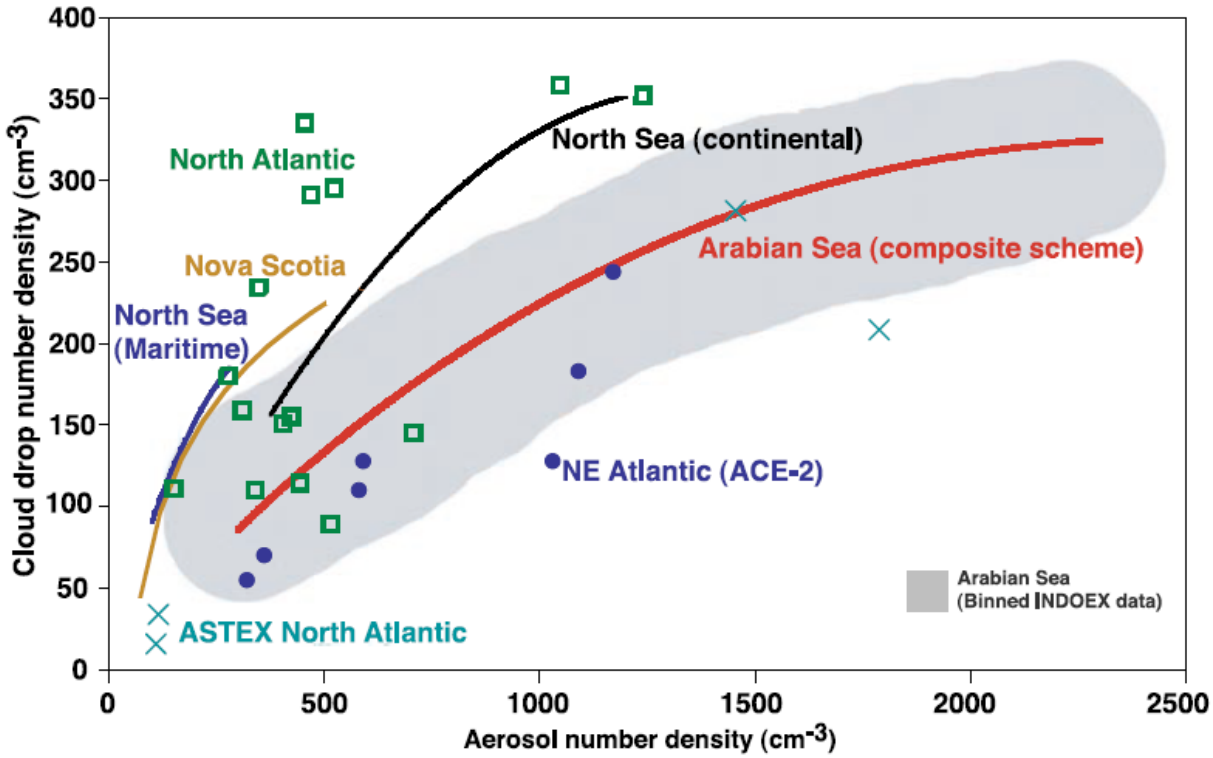

Fig. 4: Cloud drop number density as a function of aerosol number density (from *Ramanathan et al.*, 2001). Symbols represent observations while solid lines are respective fitted curves and the grey-shaded area represents the uncertainty interval of the Arabian Sea composite scheme (see *Ramanathan et al.*, 2001 for details).

Thus, the droplet growth due to coalescence processes is also reduced for smaller liquid water cloud droplets of polluted conditions. The result is a tendency of the liquid water droplets to stay at smaller sizes. Fig. 4 shows aircraft observations of cloud droplet number density and aerosol number density (taken from *Ramanathan et al.*, 2001). It is clearly evident that both are positively correlated. An extreme example of the suppression of droplet growth by the high availaility of CCN is presented for clouds developing in the smoke plumes of 1991 Kuwait oil fires by *Rudich et al.* (2003) from AVHRR observations. They moreover report a dependence on CCN size of this effect with small CCN reducing cloud droplet growth much

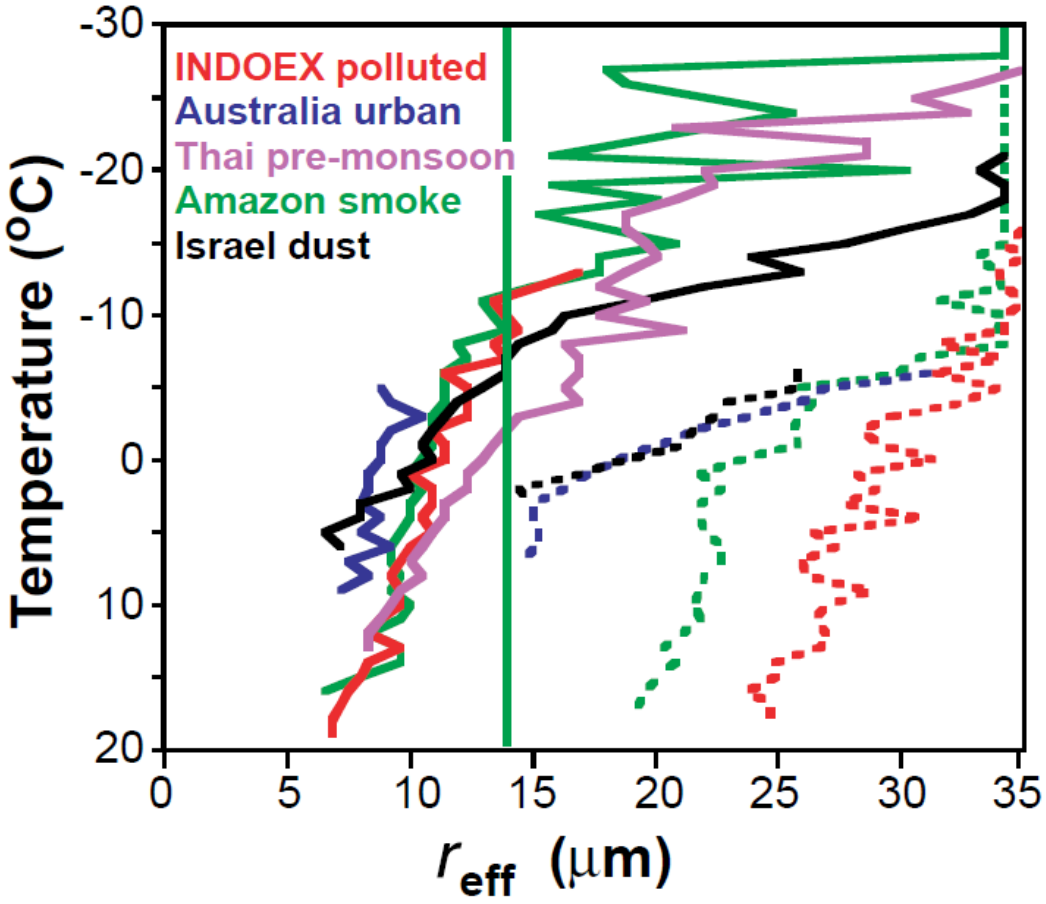

Fig. 5: Satellite retrieved median liquid water cloud effective radius as a function of cloud top temperature for polluted (solid lines) and pristine (dashed lines) conditions from different locations (from *Ramanathan et al.*, 2001).

stronger than giant CCN. Fig. 5 presents satellite retrieved median cloud effective radius as a function of cloud top temperature for polluted (solid lines) and pristine (dashed lines) conditions in several regions of the world (from *Ramanathan et al.*, 2001). For non-glaciated clouds strongly reduced effective radius is observed in all case studies under polluted conditions.

3.3 Aerosol effects on cloud optical depth and albedo

Twomey (1974) and, in more detail, *Twomey* (1977) describe a resulting effect of cloud albedo enhancement by pollution (aerosol) resulting from reduced droplet sizes (often evaluated as reduced effective radius). This effect is often referenced to as the "Twomey effect" or "first indirect aerosol effect". *Twomey* (1977) describes cloud optical depth as a direct and monotonic function of cloud droplet number concentration , itself being a direct function of the number of available CCN, given a sufficient supply with water vapour. Finally the cloud albedo, i.e. the ability of the cloud to reflect solar radiation, is a direct function of the optical depth τ, hence an increase of cloud albedo as a result of high aerosol loads.
While *Twomey* (1977) presents the theoretical basis for reduced cloud droplet sizes and the resulting albedo increase, many observational evidence from case studies has ben presented for this indirect aerosol effect on the radiation blance to be present in nature (e.g. *Kaufman and Fraser*, 1997; *Feingold et al.*, 2001; *Ramanathan et al.*, 2001; *Kaufman et al.*, 2002; *Rosenfeld*, 2006a).

3.4 Different aerosol effects on cloud lifetime

Besides the cloud albedo enhancement reduced droplet sizes also decrease precipitation efficiency (*Albrecht*, 1989; *Rosenfeld et al.*, 2001; *Hui et al.*, 2008) as a consequence of reduced collection efficiency for populations of smaller droplets (*Albrecht*, 1931, *Langmuir*, 1948) . Observations of clouds with the only difference being the reduction of effective radius within the pollution plumes showed precipitation only outside the pollution plumes, not inside. Thus, as the liquid water is not removed from the cloud by precipitation, the liquid water path increases and so does the cloud lifetime (e.g. *Haywood and Boucher*, 2000). As a consequence cloud cover will be increased and cloud top temperature will decrease, as the convective uplift continues (*Rosenfeld et al.*, 2006b). This is the so-called “Albrecht effect” or second indirect aerosol effect. Fig. 6 shows the cloud depth, i.e. its vertical extent from cloud base, as a function of effective radius for different conditions (from *Freud et al.*, 2005). For polluted conditions cloud depth reaches much higher values for relatively small effective radius compared with pristine maritime conditions ("Blue Ocean").

In order to verify the Albrecht effect over ocean from satellite observations, *Han et al.* (2002) present correlation between AVHRR derived AOD and cloud LWP. As for all AVHRR and most other studies, no aerosol species separation is taken into account. Moreover, only liquid water clouds with CTT>273K are used for analysis, which is found very often in the literature. LWP is derived from liquid phase cloud effective radius and cloud optical depth (eq. 12). Three different behaviours of LWP under aerosol influence are found from the correlation analysis: increasing, more or less constant and decreasing LWP. *Sekiguchi et al.* (2003) also present globally negative correlations between aerosol load and effective radius over ocean from AVHRR observations. Moreover they report positive correlations between AOD and both, optical depth and cloud cover. CTT decreases with aerosol particle numbers in their results. Large variations occur between the comparison of correlations observed by AVHRR and by POLDER. Again only water clouds over ocean have been studied here.

The cloud lifetime enhancement has been found to be inconsistent with high resolution model results (*Wang et al.*, 2003; *Ackerman et al.*, 2004; *Jiang and Feingold*, 2006), whereas satellite case studies both supporting (e.g. *Kaufman et al.*, 2005) and rejecting (e.g. *Matsui et al.*, 2006) this hypothesis are found.

Langmuir (1948) reported two different possibilities of cloud development when seeding cumulus clouds with dry ice particles. The clouds may immediately start precipitating due to the provision of giant cloud droplets by large aerosol (dry ice) particles and then dissipate. It is equally possible that precipitation does not immediately start and the clouds rapidly grow to heavy rain storms.

Stevens and Feingold (2009) suggest a couple of "buffers" for aerosol indirect effects, including also stronger precipitation as a consequence of faster cloud growth in the initial phase or reaching of the glaciation layer and thus forming rain through the ice phase. Consequently, in recent years concern arose whether aerosol entrainment really enhances cloud lifetime. *Small et al.* (2009) present evidence from in-situ observations and numerical modelling that pollution leads to a reduction of cloudiness rather than to increased lifetime. They suggest an evaporation-entrainment feedback loop to enhance the entrainment of descending air into the cloud. Thus evaporation is increased, thereby the cloud liquid water is reduced

without precipitation and the cloud lifetime is shortened instead of being enhanced. Effectively the cloud is dried out by evaporative cooling in this case.

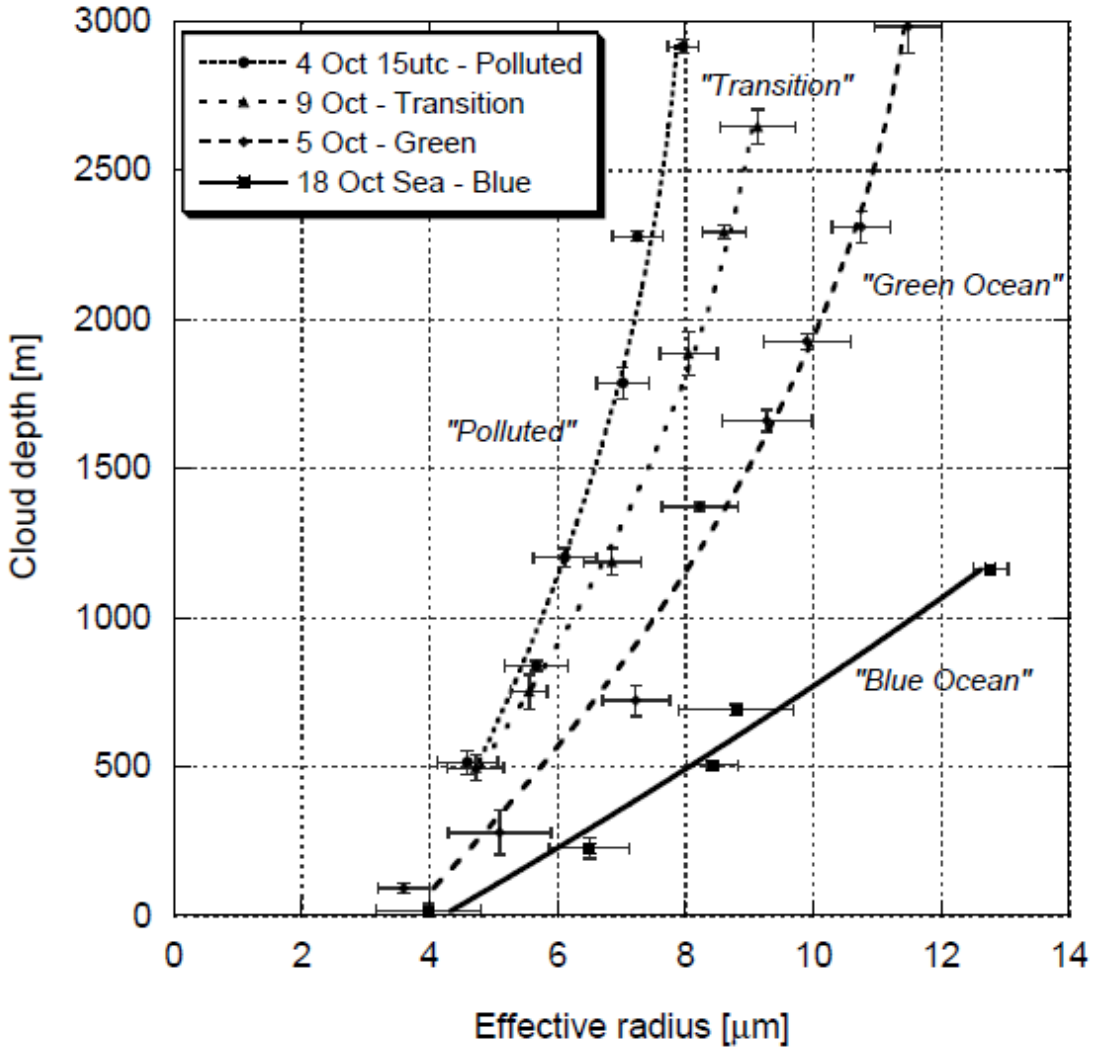

Fig. 6: Cloud depth as a function of effective radius for different pristine and polluted conditions (from *Freud et al.*, 2005).

Analysis of satellite data of clouds embedded in varying concentrations of smoke from fires in the Amazon basin shows that for the thicker clouds an increase in the smoke AOD raises the cloud top temperature and decreases the cloud reflectance, while still reducing droplet size (*Kaufman and Nakajima*, 1993; *Kaufman et al.*, 2002). The simultaneous rise in CTT (descending of cloud top height) and reduction in reflectance indicates the possibility of a reduction in convection, thereby causing a decrease in the updraft speed and in the amount of liquid water available to form the cloud (*Kaufman et al.*, 2002).

There is another mechanism of aerosol cloud interaction counteracting to the lifetime enhancement by the “Albrecht effect”. Absorbing aerosols can initiate a convective stabilisation of the atmosphere by solar heating (*Kaufman and Fraser*, 1997; *Ackerman et al.*, 2000; *Kaufman et al.*, 2002; *Koren et al.*, 2008; *Davidi et al.*, 2009). Moreover the absorption of solar irradiance results in surface cooling (*King et al.*, 1999; *Göttsche and Olesen*, 2009) adding to the reduction of convective instability.

This “semi-indirect effect” (*Kaufman et al.*, 2002) may possibly counteract the cloud lifetime increase by the “Albrecht effect” ("buffered system", *Feingold et al.*, 2005; *Stevens and Feingold*, 2009).
Koren et al. (2008) and *Small et al.* (2011) suggest a microphysical-radiative equilibrium (MRE) to be governed by the balance of microphysical invigoration of convection (lifetime effect) and the convective stabilisation by solar heating. They describe a system of boundary layer convection where microphysical effects are strongest for low and moderate AOD while the stabilisation effect outbalances the invigoration for higher AOD. Nevertheless, as for instance pointed out in *Small et al.* (2011), it is hardly possible to determine the convective stabilisation from satellite alone. As most operational weather models do not include aerosol-radiation-meteorology feedbacks, also numerical modelling as used e.g. in *Small et al.* (2011), despite depicting some evidence for this effect, does not provide a real proof of the atmospheric heating claimed to be responsible for the effect. *Stevens and Feingold* (2009) however also pointed out that some of the effects seen in correlations between cloud cover and aerosol optical depth may be consequences of an opposite impact of clouds on aerosols by swelling of hygroscopic aerosols, which thus under moist conditions, e.g. near clouds or at higher cloud cover, increases AOD (see also *Koren et al.*, 2007).

3.5 Aerosol effects on cloud phase

Langmuir (1948) reports generation of precipitation by cloud seeding with dry ice particles. These are especially suitable as ice nuclei and enhance the freezing efficiency of the cloud droplets. As with the accelerated onset of cloud droplet freezing the Bergeron-Findeisen process works as a supporting feedback, a chain reaction as described in *Langmuir* (1948) sets in and produces cloud ice particles sufficiently large for generation of strong precipitation. The same ice nucleation enhancement effect is reported independently by *Vonnegut* (1947) with silver iodide (AgI) instead of dry ice particles. Thus with aerosol particles well suitable as ice nuclei, convective growth and consequently precipitation enhancement (called “cloud seeding” when aerosol particles are entrained artificially) is also possible (*Langmuir*, 1948; *Givati and Rosenfeld*, 2005).
Especially in the case of mineral dust, these aerosol particles are reported to act as effective ice nuclei, enhancing the freezing of cloud droplets (*Broadley et al.*, 2012) and thus increasing cloud updrafts and cold rain precipitation (e.g. *DeMott et al.*, 2003; *Jenkins et al.*, 2008). But this process is not yet fully understood as there are also cloud observations without enhanced freezing under dust influence (e.g. *Ansmann et al.*, 2008). There is evidence from laboratory measurements that sulphuric coating of dust particles after long-range transport drastically reduces the ice nucleation efficiency of the dust particles (*Möhler et al.*, 2008; *Eastwood et al.*, 2009). Moreover the ice nucleation efficiency of mineral dust depends on its mineralogical composition and the particle size distribution of the dust (*Broadley et al.*, 2012).
By potential increase of cloud water path and a resulting suggested decrease of cloud top temperature (“Albrecht effect”) also more clouds reach freezing levels, thus an increase in cloud ice fraction can also result from other aerosols than mineral dust (*Stevens and Feingold*, 2009). Moreover, *Sassen and Khvorostyanov* (2008) found evidence that also smoke from boreal fires may act as effective ice nuclei and thus impact on cloud phase.

3.6 Indirect aerosol effects and climate

Besides the immediate effect on cloud physical properties indirect aerosol effects also impact on the climate system, mainly through changes of the radiation balance, and also due to changes of precipitation (*IPCC*, 2007).
The so-called “Twomey-effect”, i.e. the cloud albedo increase by reduced droplet sizes causes an increased reflection of solar radiation by cloud and thus a cooling climate effect. An increased cloud cover caused by increased cloud lifetime due to suppressed precipitation (“Albrecht-effect”) is suggested to also have a cooling climate effect, but the net effect also depends on cloud thickness and thus cloud top temperature. Consequently the direction (cooling or warming) of such effect is less understood. Semi-indirect effects by reduced convection due to convective stabilisation of the boundary layer by absorbing aerosols reduce cloud cover and thus act as warming indirect aerosol effects. Invigorated convection by early freezing and additional release of latent heat generate higher anvil outflow cirrus fractions in the case of increased deep convective activity. These cirrus clouds have strongly warming climate effects – especially above semi-arid bright surfaces, where cloud albedo effects are relatively smaller.

4 Motivation and definition of analysis regions

In a critical review of aerosol-cloud-interactions and their understanding *Stevens and Feingold* (2009) pointed out that it will be most effective to analyse indirect aerosol effects in well defined "cloud regimes" rather than globally. These regimes may be sensitive to different effects or at different levels to airborne aerosol. Tropical deep convection over land has been identified as one of the most promising (in terms of identification of indirect aerosol effects) and one of the most sensitive (in terms of consequences for radiation balance and precipitation) cloud regimes by them. Accordingly, relationships between aerosol and cloud properties are analysed in four different selected subtropical regions. These regions are the subsaharan Sahel belt (9°N-18°N, 17°W-30°E), the Southern African Kalahari region including adjacent desert and steppe like the Namib and the Karoo (15°S-30°S, 15°E-35°E), the Arabian Peninsula (20°N-35°N, 35°E-55°E) and the North African Maghreb (20°N-35°N, 20°W-20°E).
Fig. 7 presents the four analysis regions highlighted in the map of annual mean cloud water path from MODIS Aqua observations of 2009.

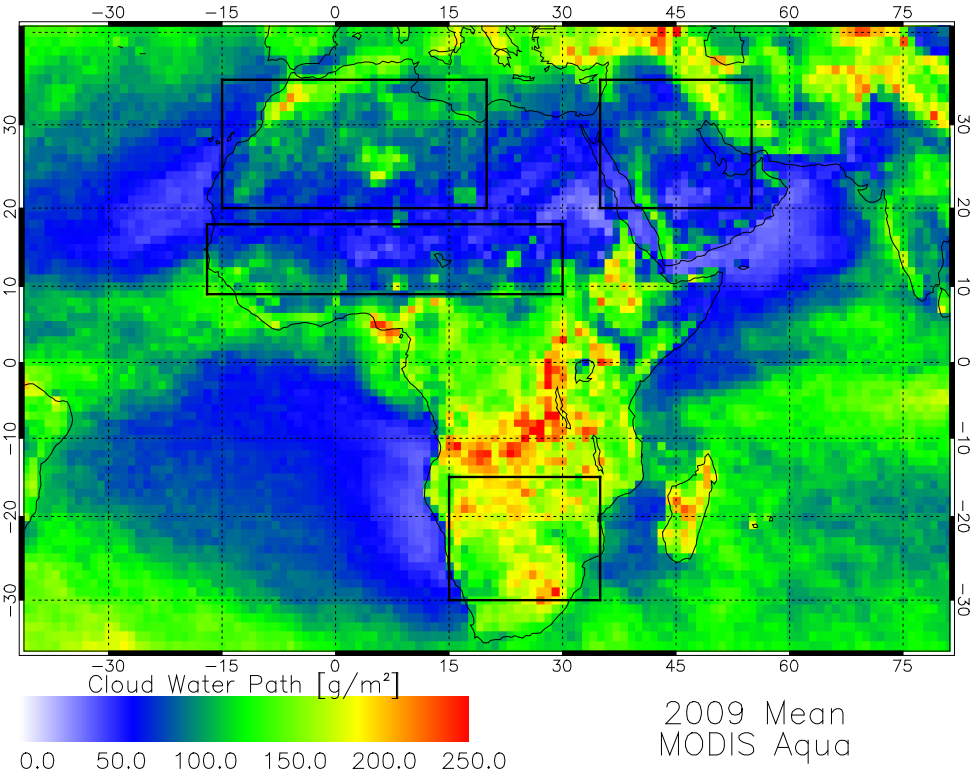

Fig. 7: Annual mean cloud water path from MODIS Aqua for 2009. The black boxes highlight the four analysis regions.

All four analysis regions are either semi-arid or arid (*Laity*, 2008) with strong annual cycles of convection and rainfall. Generation of convective cloud cells and storms due to warm surfaces dominates cloud formation in all regions. Consequently, all four regions show strong diurnal convection cycles. These cloud cells often develop into

mesoscale cloud systems ("MCS", e.g. *Laurent et al.*, 1998; *Mathon et al.*, 2002). Especially in the Western Sahel these convective storms or MCS can organise into squall line systems connected to East-African Waves (e.g. *Fink and Reiner*, 2003). The annual cycle of cloud development and precipitation in the Sahel is governed by the intrusion of the intertropical convergence zone (ITCZ) into the domain (*Mathon et al.*, 2002). In the Western Sahel the monsoon circulation with monsoonal flow from the Gulf of Guinea and dry *Harmattan* winds from the Sahara in the North generates a very high humidity contrast which is for example expressed by the strong dew point temperature gradient defining the innertropical discontinuity (e.g. *Flamant et al.*, 2009).

In the Kalahari region austral summer monsoon from the Indian Ocean advects moisture into the region similarly to West Africa. It is evident from fig. 7 that in the Southern African analysis region annual mean cloud water path is the highest of all four regions. In the two northern regions, Maghreb and Arabia, also frontal clouds connected to transient cyclones contribute to observed convection (e.g. *Alpert and Ziv*, 1989).

Aerosol in all four analysis regions can be seperated mainly into two aerosol types. Mineral dust is present and dominates the coarse mode fraction (particle diameter > 1µm) in all regions while the aerosol fine mode fractions may vary between biomass burning and industrial (especially from the oil industry in Arabia) aerosols. Consequently the separation into two distinct aerosol classes with suggested different influences in cloud development is generally sufficient from satellite.

In the Sahel biomass burning aerosol strongly dominates the fine mode fraction (e.g. *McConnell et al.*, 2008). In Southern Africa the biomass burning aerosol is the predominant aerosol type. In the Maghreb aerosol is mainly mineral dust from the Sahara and also some biomass burning aerosol from wildfires during summer. Mineral dust also dominates Arabian aerosol, but here the fine mode fraction includes industrial aerosols and soot from the oil industry as well as episodically soot from oil fires. Biomass burning aerosol does not significantly contribute to Arabian aerosol loads.

In regions influenced by summer monsoon (Sahel and Southern Africa) aerosol load peaks before the onset of the monsoon, i.e. in the late dry season in spring (March to May in the Sahel, September to November in Southern Africa). In the Maghreb and in Arabia peak aerosol loads are connected to highest windspeeds for dust lifting, thus in the late winter and early spring (February to April).

5 Data

5.1 Aqua MODIS

The MODerate resolution Imaging Spectro-radiometer (MODIS) is operated on the sun-synchronous Terra and Aqua NASA-EOS satellites. Six consecutive years (2004-2009) of MODIS observations from the Aqua satellite are used here. Aqua crosses the equator at 13:30 local solar time in the ascending orbit. The MODIS atmosphere collection 5.1 daily level 3 prouct ("D3") combines aerosol and cloud observation averages at 1° spatial resolution (*Hubanks et al.*, 2008). Cloud observations include cloud cover (seperated into total, liquid and ice), cloud top temperature, cloud effective radius (liquid and ice seperately) and cloud, liquid and ice water path from the standard MODIS level 2 retrievals (*King et al.*, 2003). The definition of ice cloud effective radius follows that of *Fu and Liou* (1993).
MODIS cloud products have been validated during several field campaigns (*King et al.*, 1997). Global comparison with ground based lidar observations show a detection of 83% of all clouds observed by the lidars with the MODIS cloud detection scheme (*Ackerman et al.*, 2008). Cross-validation with spaceborne CALIOP lidar observations shows cloud detection rates of 85%-87% by the MODIS algorithm. MODIS cloud detection works best at daylight condition (95%) and worse at night (~80%). Sensitivity of the cloud detection algorithm is highest for clouds with optical depth larger than 0.4 (*Ackerman et al.*, 2008). On average cloud top height is underestimated by MODIS by about 1.4km due to misclassification of thin cirrus (*Holz et al.*, 2008). Nevertheless, as lidar observations (ground based and from space) are nadir-only point observations, varying representativity of clouds detected by lidar for the MODIS observation as well as viewing angles also impact on detection rates (*Ackerman et al.*, 2008). Comparison with the CLAVR cloud detection scheme for AVHRR shows that with MODIS up to 30% more clouds are detected than with AVHRR (*Heidinger et al.*, 2002).
Cloud optical depth and effective radius have recently been validated for liquid water clouds (stratocumulus) over the Pacific Ocean by comparison with observations of intense research flights of the VOCALS-REx campaign in 2008 (*Painemal and Zuidema*, 2011). Optical depth correlates well with in-situ measurements (ρ=0.83) taking into account spatial variability and three-dimensional effects. MODIS slightly overestimates cloud optical depth with a bias of 1.42. Liquid cloud effective radius also correlates well with aircraft measurements (ρ=0.98), but significantly overestimates cloud top effective radius by 15%-20%. All analysed uncertainty measures are smaller than the differences between MODIS retrieval and measured effective radius. Consequently also MODIS liquid water path exceeds in-situ measurements.
For aerosol retrieval the "dark target retrieval" (*Remer et al.*, 2006; *Levy et al.*, 2007; *Levy et al.*, 2010) is used together with the "Deep Blue" algorithm (*Hsu et al.*, 2004). "Deep Blue" is not fully processed for the analysis period for the Terra-MODIS dataset, hence the use of Aqua only. The expected AOD error of the "dark target" aerosol product is ±(0.05+0.15AOD), as reported in *Remer et al.* (2006) and *Levy et al.* (2010). Globally 69% of MODIS aerosol observations (over land) are found to be within the range of expected error (*Levy et al.,* 2010). The AOD-bias between MODIS and the AErosol RObotic NETwork (AERONET, *Holben et al.*, 1998) is reported to be +0.029 at a correlation of ρ=0.88.
For large parts of the analysis domains the dark target approach does not provide sufficient observations due to the high reflectance of the dry surface. *Hsu et al.*

(2004) developed a method for aerosol remote sensing with SeaWiFS and MODIS also over bright refleting surface ("Deep Blue" method). Here the 0.412µm channel is also exploited due to the higher contrast between aerosol and bright surfaces at this wavelength. Results are found to generally fall into an envelope of ±(0.20AOD) compared to AERONET (*Hsu et al.,* 2004; *Hsu et al.,* 2006). Mineral dust from the Bodélé depression, one of the most active dust source regions world wide (e.g. *Koren et al.*, 2006; *Ben-Ami et al.*, 2010), consists mainly of low density diatomite and eroded diatomite sand (*Bristow et al.*, 2009) and thus may be less absorbing than mineral dust form other sources. Thus dust optical depth from the Bodélé Depresion may be overestimated by the "Deep Blue" method (*Hsu et al.,* 2004).
Aerosol type speciation for the dark target retrievals is done by the fine mode fraction η (*Remer et al.*, 2006). Recent validation results by *Levy et al.* (2010) show that the calculation of fine and coarse mode AOD from η introduces very large uncertainties over land. Moreover the validation shows that the selection of η in the MODIS retrievals is not always justified. *Levy et al.* (2010) show that aerosol particle size information in the "dark target" product is generally binary, fine mode fraction equals either 0.0 or 1.0 in most cases. Thus they conclude that the MODIS retrieval cannot capture the variability of particle size distributions as indicated by AERONET Ångström exponent. In most cases, when MODIS indicates fine mode dominance, this finding agrees with AERONET. On the other side MODIS falsely identifies coarse mode aerosol (dust), thus the fine mode detection is more reliable. The validation has been performed with level 2 data, results are averaged into 1° boxes in the level 3 product. Thus dominating fine mode areosol is assumed here for $\eta < 0.5$ and dominating dust is assumed for $\eta > 0.5$. AOD is not scaled by fine mode fraction (as suggested by *Levy et al.*, 2010), but the respective aerosol type is assumed to dominate the total AOD and thus the binary information only is used.
For the "Deep Blue" observations mineral dust is characterised by AOD > 0.2 and Ångström exponent $\alpha < 0.6$. Ångström exponent is derived from satellite observations following

$$\frac{AOD_{0.44\mu m}}{AOD_{0.87\mu m}} = \left(\frac{0.44\mu m}{0.87\mu m}\right)^{\alpha} \qquad (13)$$

This dust filtering method is motivated by *Dubovik et al.* (2002), who used a similar approach for determining AERONET scenes which very likely show mineral dust. The Ångström exponent threshold of 0.6 is only slightly higher than the value of α=0.5 used for the dust model in the MODIS "dark target" retrieval (and well below the value of α=1.8 for fine mode aerosol, *Levy et al.*, 2010).
For gridboxes with both, "dark target" and "Deep Blue" aerosol retrievals available, AOD is calculated as the average of both. If the "dark target" retrieval indicates fine mode aerosol, this aerosol type is assumed following *Levy et al.* (2010). If coarse mode aerosol is identified by the "dark target" retrieval, the Ångström exponent filering of the "Deep Blue" method is used for the aerosol type assumption.

5.2 ENVISAT

ENVISAT provides observations of the Advanced Along-Track Scanning Radiometer (AATSR) and the SCanning Imaging Absorption spectroMeter for Atmospheric

ChartographY (SCIAMACHY). Cloud properties are retrieved from AATSR with the AVHRR Processing scheme Over Land, cLouds and Ocean (APOLLO) originally developed for the Advanced Very High Resolution Radiometer (AVHRR) by *Saunders and Kriebel* (1988), *Kriebel et al.* (1989) and *Kriebel et al.* (2003). Updates to the cloud detection with APOLLO from AATSR for tropical and subtropical land regions enable a better detection also of shallow warm-top convection due to readjusted reflectance and brightness temperature tests (*Holzer-Popp et al.*, 2008). Cloud top thermodynamical phase characterisation is determined with the phase discrimination algorithm method of *Pavolonis and Heidinger* (2004).
The revised APOLLO cloud product from AVHRR has been validated e.g. against meteorological standard SYNOP observations throughout Europe (*Kriebel et al.*, 2003). 70% of all observations have been found to be within ±1/8 of SYNOP cloud cover. The remaining discrepancies are mainly explained by time differences between observations of up to 60 minutes, during which cloud cover can change significantly. Correlation coefficients between APOLLO and SYNOP cloud cover over Europe are between 0.69 in winter and 0.91 in summer (*Meerkötter et al.*, 2004).
Cloud optical depth is retrieved in APOLLO assuming an effective radius of 10µm. Consequently, no effective radius is retrieved. For ice clouds a correction factor is applied to the retrieved optical depth (*Kriebel et al.*, 1989). For thin ice clouds, no optical depth and cloud top temperature are retrieved. Cloud property results from AATSR are averaged onto a 1°x1° grid.
From ENVISAT aerosol optical depth and type is retrieved with the SYNergistic AErosol Retrieval (SYNAER) method for SCIAMACHY and AATSR onboard ENVISAT (*Holzer-Popp et al.*, 2008). SYNAER also follows a "dark target" approach, thus no SYNAER aerosol retrievals are available for bright reflecting surfaces.
After APOLLO cloud screening from AATSR observations surface reflection and AOD are retrieved for 40 predefined aerosol mixtures separately. The AATSR AOD then is coregistrated with the respective SCIAMACHY pixel and a least squares fit is applied for selecting the best fitting aerosol mixture (*Holzer-Popp et al.*, 2008). The 60x30 km² SCIAMACHY pixels are maped onto the 1°x1° grid also used for AATSR-APOLLO.
Generally the combination of SCIAMACHY scan mode between nadir and limb observations and the small swath width of AATSR result in a quite low sampling with ENVISAT SYNAER. Moreover the "dark target" approach limits SYNAER to regions with sufficiently low surface reflectance (vegetated areas and ocean). Consequently sample sizes for analysis are not comparable to those of MODIS (for which also aerosol observation pixels are smaller). Nevertheless, the use of the spectral fit from SCIAMACHY provides information about aerosol type (*Martynenko et al.*, 2011). SYNAER aerosol results are composed from four aerosol components: water soluble aerosols, soot, mineral dust and sea salt.
In this analysis, water soluble and soot are grouped together in one "fine mode aerosol" class in order to remain consistent with MODIS. Thus, besides total aerosol the two classes "mineral dust" and "fine mode aerosol" are also analysed from ENVISAT. As for MODIS the entire grid box is flagged as dominated by either dust or fine mode aerosol and total AOD is assumed to represent the dominating aerosol type.
SYNAER results have been validated against AERONET observations. SYNAER and AERONET AOD correlate with ρ=0.85 at a standard deviation of 0.1 between SYNAER and AERONET AOD (*Holzer-Popp et al.*, 2008). SYNAER data are available online from the World Data Center for Remote Sensing of the Atmosphere, WDC-RSAT (http://wdc.dlr.de). ENVISAT data used here are for the years 2004-2008

and cover the three regions Sahel, Southern Africa (Kalahari) and the Maghreb. For the Arabian region no ENVISAT data are processed for the respective years.

5.3 IASI

The Infrared Atmospheric Sounding Interferometer IASI operated on the Metop-A satellite (and subsequent ones in the future) is a Michelson interferometer with very fine spectral resolution in the thermal infrared. It observes infrared radiance spectra at 12km nadir ground resolution and a swath of 48.3° (2200km). 8461 channels in the thermal infrared result in a spectral resolution of 0.25cm^{-1}. Instrument stability is very high, namely 0.1K (*Blumstein et al.*, 2004; *Larar et al.*, 2010). The interferometer is accompanied by an Integrated Imaging Subsystem (IIS), which provides broadband (10-12.5µm) brightness temperatures at finer spatial resolution (2x2 IASI pixels are covered by 64x64 IIS pixels). Although originally being designed for co-registration with AVHRR operated on the same spacecraft, IIS observations also provide estimates of the spatial homogeneity of IASI observations.
IASI data used for dust and ice cloud retrieval are level 1c radiance spectra of one year (2009) jointly distributed via the EUMETSAT Data Centre (UMARF) and the NOAA Comprehensive Large Array Stewardship System (CLASS). IASI observations from both overpasses (ascending at night and descending with equator crossing time at 09:30 local time) of the Metop-A satellite are used for dust and ice cloud retrieval.

5.4 AERONET

IASI AOD is evaluated against observations of the AErosol Robotic NETwork (AERONET, *Holben et al.*, 1998). This network collects standardized observations with the CIMEL Electronique 318A robotical pointed sun and sky spectral radiometer. Direct sun measurements are made at 0.44µm, 0.67µm, 0.87µm, 0.94µm and 1.02µm, sky measurements at 0.44µm, 0.67µm, 0.87µm and 1.02µm. The uncertainty of AERONET meassurements is approximately ±0.02 in AOD units under cloud free conditions (*Holben et al.*, 1998).
For comparison with IASI derived dust AOD coarse mode AERONET AOD observations processed with the Spectral Deconvolution Algoritm (SDA, *O'Neill et al.*, 2003) have been used. One should be aware that in the SDA algorithm coarse mode AOD is somewhat sensitive to the presence of thin clouds and thus may be overestimated (*O'Neill et al.*, 2003). All available AERONET observations of the year 2009 over Northern hemispheric Africa, Southern Europe, the Arabian Peninsula and Central and East Asia are used.

6 New method for remote sensing of mineral dust and ice clouds with IASI

6.1 Infrared optical properties of mineral dust

The majority of airborne mineral dust is composed of silicate minerals, i.e. quartz (SiO_2), opal and diatomite (fossil amorphous SiO_2), silicate clays (mostly illite mica $K[Al,Mg,Fe]_2(Si,Al)_4O_{10}[OH]_2H_2O$, kaolinite $Al_2[(OH)_4|Si_2O_5$ and montmorillonite / smectite $(Na,Ca)_{0.3}[Fe,Al,Mg]_2Si_4O_{10}[OH]_2,•2H_2O]$), other mica (chlorite $(Mg,Fe,Al,Mn)_{4\text{-}6}(Si,Al)_4O_{10}(OH,O)_8$ and muscovite $KAl_2AlSi_3O_{10}(OH)_2$) or feldspars (albite $NaAlSi_3O_8$, anorthite plagioclase $CaAl_2Si_2O_8$, orthoclase $4[KAlSi_3O_8]$ and mixed forms between them). Moreover carbonates like calcite ($CaCO_3$) and dolomite ($(Ca,Mg)CO_3$), sulfates like anhydrite ($CaSO_4$) or gypsum ($CaSO_4•2H_2O$), and iron oxides (hematite α-Fe_2O_3 and limonite/goethite α-FeO[OH]) are commonly found in mineral dust samples (e.g. *Caquineau et al.*, 1998; *Sokolik and Toon*,1999; *Formenti et al.*, 2008; *Markl*, 2008; *Kandler et al.*, 2011; *Skonieczny et al.*, 2011).

Fig. 8 shows an example of an electron-microscope image of mineral dust particles collected during a dust-storm episode in in northwestern Beijing in China (from *Shao et al.*, 2007), showing the wide range of particle sizes and shapes covered by mineral dust aerosol.

Silicates are characterised by strong ν(Si-O) vibrational strech resonance bands around $1050cm^{-1}$ [9.5µm], which result in strong absorption and reststrahlen scattering around this wavenumber (e.g. *Flanigan and DeLong*, 1971; *Salisbury and Wald*, 1992; *Wald and Salisbury*, 1995; *Mogili et al.*, 2007; *Hudson et al.*, 2008b). Moreover layered alumosilicates like kaolinite show a significant secondary δ(Al-Al-OH) vibrational resonance band around $920cm^{-1}$ (e.g. *Hudson et al.*, 2008b*; Clarisse et al.*, 2013). Thus, mineral dust can also be detected in thermal infrared (TIR) satellite observations (e.g. *Shenk and Curran*, 1974; *Ackerman*, 1997). Although maximum extinction (from combined absorption and scattering) of thermal infrared radiation by silicates is observed around $1050cm^{-1}$ [9.5µm], the peak extinction is masked by the strong O_3 absorption band around $1040cm^{-1}$ [9.6µm]. Nevertheless the broad silicate resonance band shoulders stretch to outside the O_3 absorption band and thus the detection of the extinction signal is possible (e.g. *Ackerman*, 1997; *Hudson et al.*, 2008b; *Laksina et al.*, 2012; *Clarisse et al.*, 2013).

Although also some carbonate (calcite) or sulfate (anhydrite) mineral species show detectable extinction in the atmospheric window region ($830\text{-}1250cm^{-1}$ [8-12µm]), this is not the case for all relevant minerals. For example for dolomite, mainly occuring in dust from Arabian desert dust sources (*Sirocko et al.*, 2000), extinction peaks at about $1450cm^{-1}$ and no significant extinction is observed in $800\text{-}1200cm^{-1}$ (*Sokolik and Toon*, 1999; *Hudson et al.*, 2008a). Hematite and limonite/goethite exhibit a weak resonance band at $1025cm^{-1}$ which is only 2% of the intenstity of Si-O resonance in this region. Thus the iron oxide absorption is generally masked by silicate peaks in airborne dust and cannot be detected from thermal infrared satellite observations (*Flanigan and DeLong*, 1971; *Sokolik and Toon*, 1999).

In order to extract quantitative dust information from thermal infrared remote sensing the spectral characteristics of dust extinction have to be known or assumed.

Brindley and Russel (2006) compare the impact of the use of different dust models (*Volz*, 1973; *Fouquart*, 1987 and *Hess et al.*, 1998) and find very large differences in respective thermal infrared dust retrieval results depending on the dust optical properties used. This result is also supported by *Highwood et al.* (2003), who report

dust refractive indices being the major source of uncertainty for remote sensing applications, prior to dust particle size distribution. *Yang et al*. (2007) present an analysis of the impact of dust particle size and sphericity on remote sensing applications. While they conclude that asphericity impacts are stronger in solar wavelengths, they show that the single scattering albedo, i.e. the fraction of scattering in total extinction, varies significantly with particle size, small particles having smallest single scattering albedo. While from this conclusion for particles with diameter much smaller than wavelength (Rayleigh-limit, e.g. *Laksina et al.*, 2012) scattering can be neglected, it has to be accounted for at larger particle sizes significantly contributing to airborne desert dust, especially in the vicinity of dust source regions (e.g. *Johnson and Osborne*, 2011).

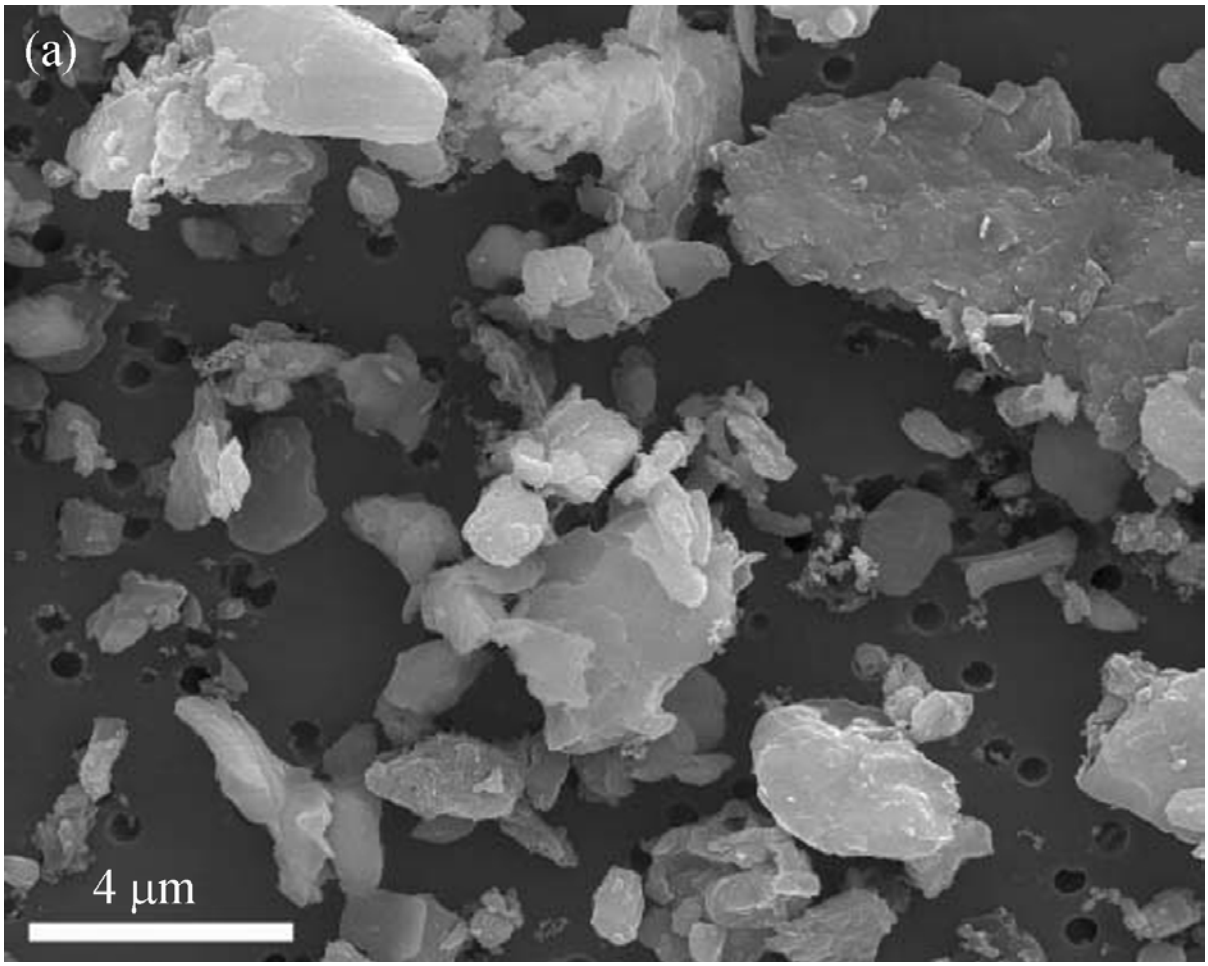

Fig. 8: Electron-microscope image of dust particles with a wide range of particle sizes encountered in a dust storm in nortwestern Beijing (China). The dark aerosol particles indicate the presence of some soot in the sample (from *Shao et al.* 2007).

Tab. 1 lists a selection of publications dealing with quantitative dust TIR remote sensing from satellite and also from ground-based observations together with the dust optical properties source used for the respective application. Although *Sokolik et al.* (1998) and *Sokolik and Toon* (1999) clearly show that dust composition has non-neglible influence on the TIR extinction spectrum and consequently on inferred dust properties (*Sokolik et al.*, 1998; *Brindley and Russell*, 2006) and that it varies strongly between dust source regions (e.g. *Sokolik et al.*, 1998; *Sokolik and Toon*, 1999;

Jeong, 2008; *Kandler et al.,* 2011), so far none of the few thermal infrared (TIR) dust retrieval algorithms does account for variable dust mineralogy in addition to particle size. Consequently a new retrieval scheme accounting for both, dust composition and particle size will add a lot of unprecedented information to remotely sensed dust observations.
Abbreviations of not yet introduced satellite instruments relate to the Atmospheric InfraRed Sounder (AIRS), the High resolution Infared Radiation Sounder (HIRS) and the Spinning Enhanced Visible and InfraRed Imager (SEVIRI).

Tab. 1: Examples of TIR remote sensing applications and respective dust optical properties.

Sensor	**Reference(s)**	**Dust optical properties**
AIRS	*Pierangelo et al.* (2004), *Peyridieu et al.* (2010)	*Hess et al.* (1998)
AIRS	*DeSouza-Machado et al.* (2010)	*Volz* (1973)
AVHRR/HIRS	*Ackerman* (1997)	*Longtin* (1988)
IASI	*Klüser et al.* (2011)	*Hess et al.* (1998)
MODIS	*Zhang et al.* (2006)	*Hess et al.* (1998)
MODIS	*Hong* (2009)	*Hess et al.* (1998)
SEVIRI	*Brindley and Russel* (2006)	*Hess et al.* (1998)
SEVIRI	*Merchant et al.* (2006)	*Hess et al.* (1998)
SEVIRI	*Li et al.* (2007)	*Volz* (1973)
ground-based interferometer	*Turner* (2008)	*Roush et al.* (1991), *Aronson et al.* (1983), *Spitzer and Kleinman* (1961)
ground-based interferometer	*Thomas et al.* (2009)	*Volz* (1973), *Fouquart* (1987)

From tab.1 it is obvious that in a large fraction of TIR dust remote sensing applications optical properties of one of the four different dust models of OPAC (Optical Properties of Aerosols and Clouds) of *Hess et al.* (1998) are used. Also the first version of the new IASI dust retrieval used OPAC for spectral characterisation of mineral dust extinction in the infrared. Especially for high-resolution infrared sounders the rather coarse spectral resolution of OPAC, being developed for applications with broadband radiometers like AVHRR or MODIS, introduces an additional source of error (see *Brindley and Russel*, 2006). The four dust types in OPAC are based on one set of refractive indices and calculated with different size distributions following Mie theory. Accordingly, those optical properties databases are not able to account for variations in dust composition, which may impact on extinction spectra (see e.g. *Hudson et al.*, 2008a,b; *Turner et al.*, 2008; *Laksina et al.*, 2012). Moreover the spectral resolution of the OPAC database is rather coarse in the thermal infrared given the spectral resolution of nowadays infrared sounding instruments like IASI. Consequently the high-resolution shape of the TIR extinction bands (i.e. the Si-O and Al-O-H resonance bands in silicates) is not well reproduced with the OPAC extinction coefficients.
Hudson et al. (2008a,b), *Mogili et al.* (2008) and *Laksina et al.* (2012) also found differences in absorption peak positions and spectral shape of the extinction band between Fourier-Transform Interferometer (FTIR) extinction measurements of typical mineral dust components and Mie calculations. Generally in Mie calculations, assuming spherical particals, infrared extinction peaks of non-spherical dust aerosol

are blue-shifted compared to laboratory measurements (e.g. *Bohren and Huffman*, 1983; *Hudson et al.*, 2008b; *Mogili et al.*, 2008). Comparing T-matrix (e.g. *Mishchenko and Travis*, 1998) calculations of dust extinction with measured extinction spectra moreover shows influence of particle shape distribution on bulk dust extinction spectra for specific minerals (*Kleiber et al.*, 2009). Nevertheless, *Yang et al.* (2007) concluded from detailed comparisons of different radiative transfer simulation methods that Mie theory applied to dust optical properties is considerably accurate for remote sensing applications in the thermal infrared window. The samples of *Hudson et al.* (2008a,b) and *Laksina et al.* (2012) also have very small particle sizes and thus are clearly in the Rayleigh limit, where scattering is extremely low and extinction is totally dominated by absorption. In particle size ranges typically found in airborne desert dust (e.g. *Weinzierl et al.*, 2009; *Johnson and Osborne*, 2011; *Ryder et al.*, 2013) the presence of, athough only a few, large dust particles causes considerable scattering and thus broadens the extinction spectrum (e.g. *Salisbury and Wald*, 1992).
As extinction peak positions and slopes of different mineralogical components of desert dust vary over the TIR domain, the mineralogy and also the morphology (asphericity) of the dust sample, which the optical properties are based on, may thus introduce further uncertainties in retrieval results (*Sokolik and Toon*, 1999).

6.2 Principles of infrared dust remote sensing

The azimuthally averaged form of the spectral radiavtive transfer equation for thermal infrared radiation including scattering as formulated e.g. by *Ackerman* (1997) or *Petty* (2006) is

$$\mu \frac{dI(\tau,\nu,\mu)}{\tau} = I(\tau,\nu,\mu) - (1-\omega_0(\nu)) \cdot B_\nu(T(\tau)) - \left(\frac{\omega_0(\nu)}{2}\right) \cdot \int_0^\mu P_s(\tau,\nu,\mu,\mu') \cdot I(\tau,\nu,\mu') d\mu' \qquad (14)$$

where μ is the cosine of the viewing angle, τ is optical depth, $B_\nu(T)$ represents the Planck function for given temperature T, ω_0 is the single scattering albedo defined by β_{scat}/β_e and P_s is the scattering phase function.
With knowledge of spectrally resolved optical depth ($\tau(\nu)$), single scattering albedo ($\omega_0(\nu)$) and assymetry parameter ($g(\nu)$), the effective transmissivity of the dust can be simulated with a discrete-ordinates approach to the Two-Stream solution of the radiative transfer equation including scattering (eq. (14)).
Strictly following *Ackerman* (1997) k and $M_\pm$ are defined as

$$k(\nu) = \left[(1-\omega_0(\nu)) \cdot (1-\omega_0(\nu) \cdot g(\nu))\right]^{\frac{1}{2}} \qquad (15)$$

$$M_\pm(\nu) = \frac{1}{1 \pm k(\nu)} \left(\omega_0(\nu) \mp \omega_0(\nu) \cdot g(\nu) \cdot (1-\omega_0(\nu)) \frac{1}{k(\nu)} \right) \qquad (16)$$

In the case of an infinite thick aerosol layer ($\tau \to \infty$) the spectrally resolved maximum reflectance of the aerosol is given by

$$R_x(\nu) = \frac{M_+(\nu)}{M_-(\nu)} \tag{17}$$

The effective transmittance of aerosol layers of finite thickness, defined as $I_{sat}(\nu)/I_{sfc}(\nu)$ can then be approximated by

$$\begin{aligned}
&\frac{I_{sat}(\nu)}{\varepsilon_{sfc} I_{sfc}(\nu)} = \frac{1}{2}\left[\frac{e^{-k(\nu)\tau(\nu)} + R_x(\nu)}{R_x(\nu)e^{-k(\nu)\tau(\nu)} + 1} + \frac{R_x(\nu) - e^{-k(\nu)\tau(\nu)}}{R_x(\nu)e^{-k(\nu)\tau(\nu)} - 1}\right] + \\
&\frac{1}{2}\frac{I_{\downarrow}(\nu)}{\varepsilon_{sfc} I_{sfc}(\nu)}\left[\frac{e^{-k(\nu)\tau(\nu)} + R_x(\nu)}{R_x(\nu)e^{-k(\nu)\tau(\nu)} + 1} + \frac{R_x(\nu) + e^{-k(\nu)\tau(\nu)}}{R_x(\nu)e^{-k(\nu)\tau(\nu)} - 1}\right] + \\
&\frac{1}{\varepsilon_{sfc} I_{sfc}(\nu)}\int_0^{\tau} B_\nu(\tau', T(\tau')) \cdot e^{-k(\nu)\tau''(\nu)} d\tau'
\end{aligned} \tag{18}$$

where $I_{\downarrow}(\nu)$ denotes downwelling radiation from above the dust layer which is reflected back to the top of atmosphere. Assuming that scattering can be neglected (which is generally not applicable for airborne desert dust, see e.g. *Ackerman*, 1997; *Yang et al.,* 2007; *Johnson and Osborne*, 2011), i.e. $\omega_0=0$ and hence $R_x(\nu)=0$, spectral radiance at wavenumber ν thus can be approximated by (*Ackerman*, 1997):

$$I_{sat}(\nu) = e^{-\frac{\tau(\nu)}{\mu}} \varepsilon_{sfc}(\nu) B_\nu(T_{sfc}) + \int_0^{\tau(\nu)} e^{-\frac{\tau(\nu)}{\mu}} B_\nu(T(\tau'(\nu)))d\tau' \tag{19}$$

I_{sat} denominates the spectral (expressed in wavenumver ν) radiance observed from space, $\tau(\nu)$ is the total atmospheric optical depth (including gas absorption) in the thermal infrared and μ is the cosine of the viewing zenith angle (in contrast to the pure Two-Stream solution presented by *Ackerman*, 1997 viewing geometry is now accounted for, see e.g. *Petty*, 2006). Moreover, T_{sfc} signifies surface temperature and ε_{sfc} surface emissivity, consequently $\varepsilon_{sfc}(\nu)B_\nu(T_{sfc}) = I_{sfc}(\nu)$. If the dust layer is assumed to be homogeneous and isothermal, the integral solves to $(1\text{-}e^{-(\tau(\nu)/\mu)})B_\nu(T_{dust})$, representing the directional effective atmospheric emission (*Ackerman*, 1997). Atmospheric emission is integrated along the optical depth coordinate. If furthermore gas absorption (and emission) is neglected, the absorbing aerosol, i.e. mineral dust, remains the only contribution to optical depth. Thus AOD can be substituted for τ in eq. (19). Consequently the equation simplifies to the widely used approximation

$$I_{sat}(\nu) = e^{-\frac{AOD(\nu)}{\mu}} \varepsilon_{sfc}(\nu) B_\nu(T_{sfc}) + \left(1 - e^{-\frac{AOD(\nu)}{\mu}}\right) B_\nu(T_{dust}) \tag{20}$$

where T_{dust} represents the temperature of the airborne dust layer (*Ackerman*, 1997).
In the case of non-neglible scattering by dust particles the Two-Stream solution for scattering and absorption can be approximated by eq. (20) when it is assumed that the term of upward reflected radiation incident from the top-of-atmosphere ($I_{\downarrow}(\nu)$) is small compared to upwelling radiation $B_\nu(T_{sfc})$ and the dust emission term (*Ackerman*, 1997; *Petty*, 2006). This assumption is true for thermal infrared radiation

in the spectral range considered here outside the O_3 band (*Petty*, 2006). Following the Kirchhoff law that for dust particles as greybodies spectral emissivity equals absorptivity (*Petty*, 2006) single scattering albedo has to be included in the dust emission term of eq. (19) and the equation becomes

$$I_{sat}(\nu) = e^{-\frac{AOD^*(\nu)}{\mu}} \varepsilon_{sfc}(\nu) B_\nu(T_{sfc}) + \left(1 - e^{-\frac{AOD^*(\nu)}{\mu}}\right) B_\nu(T_{dust}) \quad (21)$$

where

$$AOD^*(\nu) = \frac{(1-\omega_0(\nu)\cdot g(\nu))}{(1-\omega_0(\nu))} AOD(\nu) \quad (22)$$

is the scaled optical depth (*Petty*, 2006). Thermal emission by airborne dust is governed by its optical depth (*Hunt and Logan*, 1972; *Ackerman*, 1989; *Ackerman*, 1997), the single scattering albedo (its absorption) and its ambient temperature. Consequently radiance observed from space is also sensitive to dust layer temperature and, as the real atmosphere is not absolutely transparent even in window channels, height (*Ackerman*, 1997; *Pierangelo et al.*, 2004). Atmospheric absorption and emission also both contribute to the radiance observed at the satellite (eq. (18)). But as these are weak and spectrally homogeneous in the spectral regions used for dust remote sensing (830-1000cm^{-1} [10-12µm] and 1110-1250cm^{-1} [8-9µm]), they can be neglected in methods using spectral differences for dust detection (*Ackerman*, 1997; *Clarisse et al.*, 2013). This assumption is of course not valid for the O_3 absorption peaking around 1040cm^{-1}, consequently dust remote sensing methods should avoid the O_3 band (thus the gap between 1000cm^{-1} and 1110cm^{-1} in preferential spectral regions).
For low optical depths dust thermal emission may be neglected as the emission term becomes small and eq. (21) moreover simplifies to

$$I_{sat}(\nu) = e^{-\frac{AOD(\nu)}{\mu}} \varepsilon_{sfc}(\nu) B_\nu(T_{sfc}) \quad (23)$$

Thus dust consequently can be detected by a reduction of brightness temperature, or, given spectrally different dust AOD_ν in the thermal infrared, also by brightness temperature differences, e.g. between moderate and weak silicate absorption around 910cm^{-1} [11µm] and 830cm^{-1} [12µm], respectively. This finding is also true when the emission term in eq. (21) is not neglected and dust temperature is lower than surface temperature, which is generally the case in most atmospheric situations (*Ackerman*, 1997; *Ashpole and Washington*, 2012).
Nevertheless eq. (21) and especially the (over-) simplification of eq. (23) rely on a set of assumptions which are generally not valid in infrared dust remote sensing. While the assumption of homogeneous isothermal dust layers may be a good approximation for real dust layers (e.g. *Pierangelo et al.*, 2004) given the sensitivities of modern satellite instruments, neglecting of scattering is only valid for very small dust particles (*Yang et al.*, 2007) – much smaller than those naturally occurring in regions close to active dust sources (*Johnson and Osborne*, 2011). Moreover eq. (23) is an oversimplification as the temperature difference between dust layer and surface has strong impact on the observed "effective transmissivity", i.e. AOD(ν) in

eq.(23), as *Ackerman* (1997) clearly showed. This impact is also spectrally variable, the wavelengths of highest importance depend on the optical properties (thus, on the particle sizes and mineralogical composition) of the dust. This different sensitivity to dust layer temperature (and consequently height) is the basis for the dust layer height retrieval in *Pierangelo et al.* (2004).
Different methods based either on temporal comparison of brightness temperatures (*Legrand et al.*, 2001; *Miller et al.*, 2008), on brightness temperature differences (e.g. *Ackerman*, 1989; *Dunion and Velden*, 2004; *Chaboureau et al.*, 2007; *Schepanski et al.*, 2007) or combinations of both (*Li et al.*, 2007; *Klüser and Schepanski*, 2009) have been expolited successfully for dust remote sensing from TIR instruments on geostationary satellites. For polar orbiting satellites a brightness temperature difference approach has been applied to MODIS observations over Asia by *Zhang et al.* (2006) for dust storm classification.
TIR sounders operated on polar orbiting spacecraft provide a very high spectral resolution and are thus especially well suited for dust remote sensing of dust AOD, dust particle size and also height information (e.g. *Pierangelo et al.*, 2004; *DeSouza-Machado et al.*, 2006; *DeSouza-Machado et al.*, 2010; *Peyridieu et al.*, 2010).
For TIR retrieval methods using few broad channels the assumption of neglectability of atmospheric effects in eq. 9 is not valid. Especially water vapour absorption (and emission) contributes significantly to the observed radiance. The spectral resolution of modern IR sounding instruments like IASI is sufficiently high for minimising this effect by definition of "microwindows" between water vapour absorption lines in the window regions (*Comstock et al.*, 2007). Nevertheless, in order to realistically describe the radiative transfer in the atmosphere very accurate estimations of the atmospheric contributions to observed radiance are needed for quantitative dust remote sensing with such methods. Consequently, accurate radiative transfer modelling of dust effects on TIR radiance requires reliable estimation of the atmospheric state, i.e. temperature and humidity profiles (*Comstock et al.*, 2007). These either have to be retrieved simultaneously with the dust properties or must be known or estimated a priori.
Over land surface emissivity with its high variability for desert soils is the most critical parameter for dust remote sensing with thermal infrared methods (*Shenk and Curran*, 1974; *Wald and Salisbury*, 1995; *Ackerman*, 1997; *Ogawa et al.*, 2003; *Pierangelo et al.*, 2004). Recently efforts have been made to compile a global database of surface emissivity (see e.g. *Seemann et al.*, 2008). Any approach of direct radiative transfer modelling for AOD retrieval in the TIR spectrum over land requires sufficient information (or assumptions) on surface emissivity and land surface temperature, as otherwise the modelling of radiances will imply very high uncertainty due to background errors. Consequently most TIR sounder methods are applied over ocean only, where spectral surface emissivity is rather homogeneous (*Pierangelo et al.*, 2004; *DeSouza-Machado et al.,* 2006; *DeSouza-Machado et al.*, 2010; *Peyridieu et al.*, 2010).

6.3 New dust retrieval method for IASI

6.3.1 Method overview

The new developed dust retrieval method for IASI uses principal component analysis in order to extract uncorrelated pieces of information from IASI spectra. This approach enables to separate between gas absorption, surface emissivity and

absorption by dust aerosol. The algorithm outline is depicted in fig. 9 in terms of a retrieval flowchart. After preparatory steps (spectral resolution reduction, decomposition into principal components), infrared dust AOD, dust composition and particle size can be inferred simulatneously from the IASI spectra in the main retrieval section (section 6.3.5). Finally the retrieved particle size and composition are used to transfer AOD from thermal infrared to visible wavelengths.

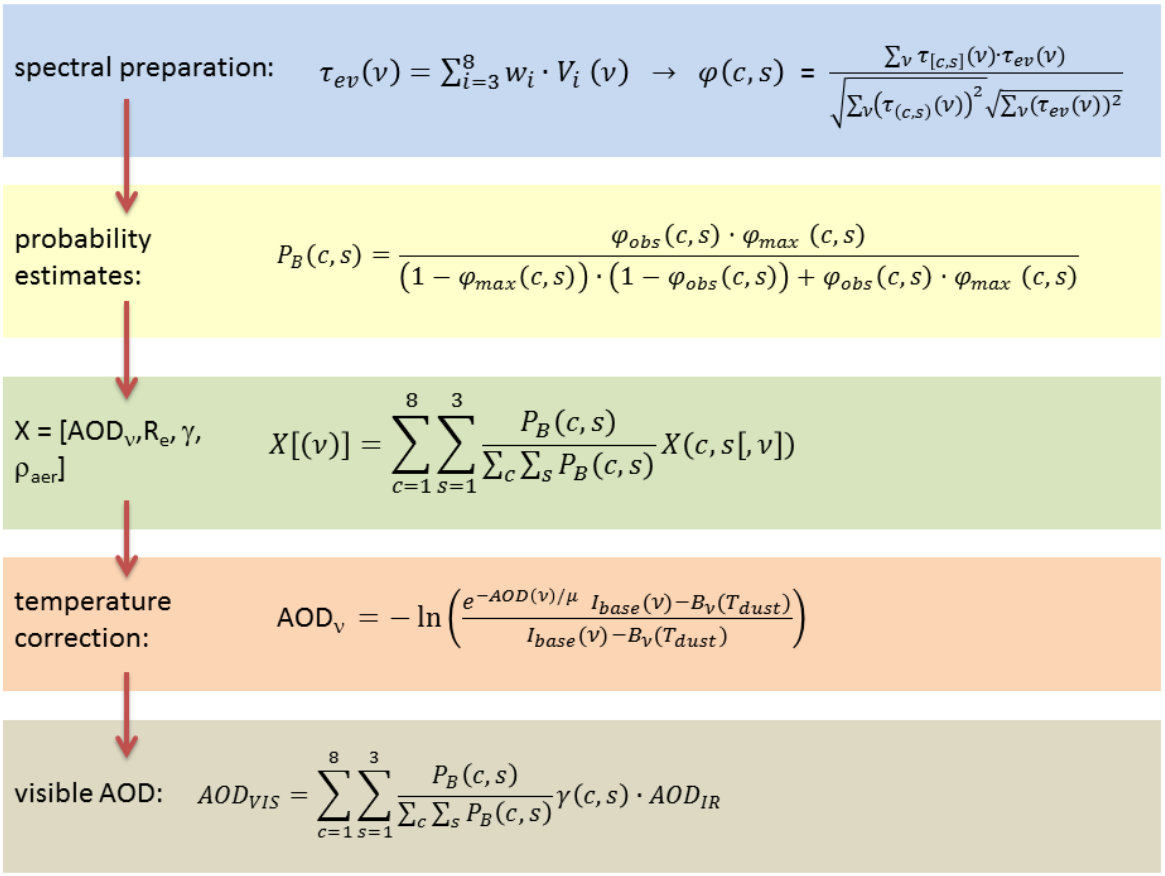

Fig. 9: Overview of the new IASI dust retrieval method. Details of the method are described in section 6.3.3 to 6.3.6.

6.3.2 Principle Component Anyalysis, Degrees of Freedom and Information content

The new IASI dust retrieval algorithm is designed to allow for fast dust remote sensing from thermal infrared observations (thus independently from solar illumination) not only over ocean and vegetation, but also over arid land surfaces. Moreover it is intended to minimize a priori assumptions, e.g. on surface emissivity and atmospheric profiles as far as possbile. One approach for reduction of required a priori information is using Principal Component Analysis (PCA) of observed spectra in order to extract useful independent pieces of information.
In Principal Component Analysis (PCA) the Eigenvalue problem of the covariance or correlation matrix of the observed data is solved (e.g. *Schönwiese*, 2006). While in remote sensing applications often Singular Vector Decomposition (SVD) is used analogously to PCA, the advantage of PCA over SVD is that the matrix, on which the Eigenvalue problem is solved, is of smaller dimensions, especially if large amounts of

data are to be analysed. The PCA represents a coordinate transformation of the observation data with the objective of finding uncorrelated basis vectors and hence reducing the dimensionality of the problem. For any n×m data matrix **X** (representing m observations of IASI spectra with dimension n in the retrieval approach), PCA is solving the Eigenvalue problem of the n×n correlation matrix **K**, where $K_{i,j}$ denotes the correlation coefficient between the i^{th} and j^{th} component of the IASI observation vector (the observed spectrum):

$$det(\boldsymbol{K}-\Lambda\boldsymbol{I}) = 0 \quad (24)$$

The resulting Eigenvectors V_i, determined from Eigenvalues Λ_i with

$$(\boldsymbol{K}-\Lambda_i\boldsymbol{I})V_i = 0 \quad (25)$$

are basis vectors for the observation space **M**, which includes, in particular, the observation data matrix **X**. Spearman rank correlation (*Spearman*, 1908) is used here to construct **K**, avoiding assumptions on normal distribution of the observations.
The weights of the Eigenvectors can directly be used to reconstruct the observation (spectrum) as a linear combination of the Eigenvectors (*Schönwiese*, 2006; *Menke*, 2012).

6.3.3 Preparation of IASI spectra

The high spectral sampling of IASI can be exploited to avoid gas absorption lines in this region and consequently to obtain mineral dust properties from the observed radiance spectra.
Brightness temperatures between 830cm^{-1} and 1250cm^{-1} are collected into 42 bins (equidistant in wavenumber space), thus 1680 IASI channels are used for the retrieval. The brightness temperature used for each of the 42 bins is represented by the maximum brightness temperature of the 40 respective channel values observed within each bin, reducing the effects of narrow gas absorption lines onto the dust retrieval.
Figure 10 presents full resolution IASI brightness temperature spectra (solid blue lines) and the binned reduced resolution spectra obtained in the way described above (red lines). It is clearly evident that there are a lot of gas absorption lines also within the atmospheric window spectral region, which impact on the full resolution brightness temperatures observed by IASI. Nevertheless the calculation of the reduced resolution spectra minimizes the impact of these gas absorption lines on the subsequent retrieval steps while still leaving enough information to exploit the spectral characteristics of the observations.
Many gas absorption features can be eliminated by this way, but of course broad band features such as ozone absorption around 1040cm^{-1} and the water vapour continuum cannot be avoided and remain part of the filtered spectra. The latter one becomes clearly evident when comparing the pristine observations over ocean with low and high water vapour. The ozone absorption band is a very strong feature in those spectra and moreover can be misinterpreted as dust signal (as silicate extinction peaks in the same spectral region). Moreover in the ozone band the slope of brightness temperatures (or radiance) is so steep that the spectrum is no longer well represented by the reduced resolution approximation (Fig. 10). Even worse, as O_3 is concentrated in the stratosphere and thus well above any dust layer, the

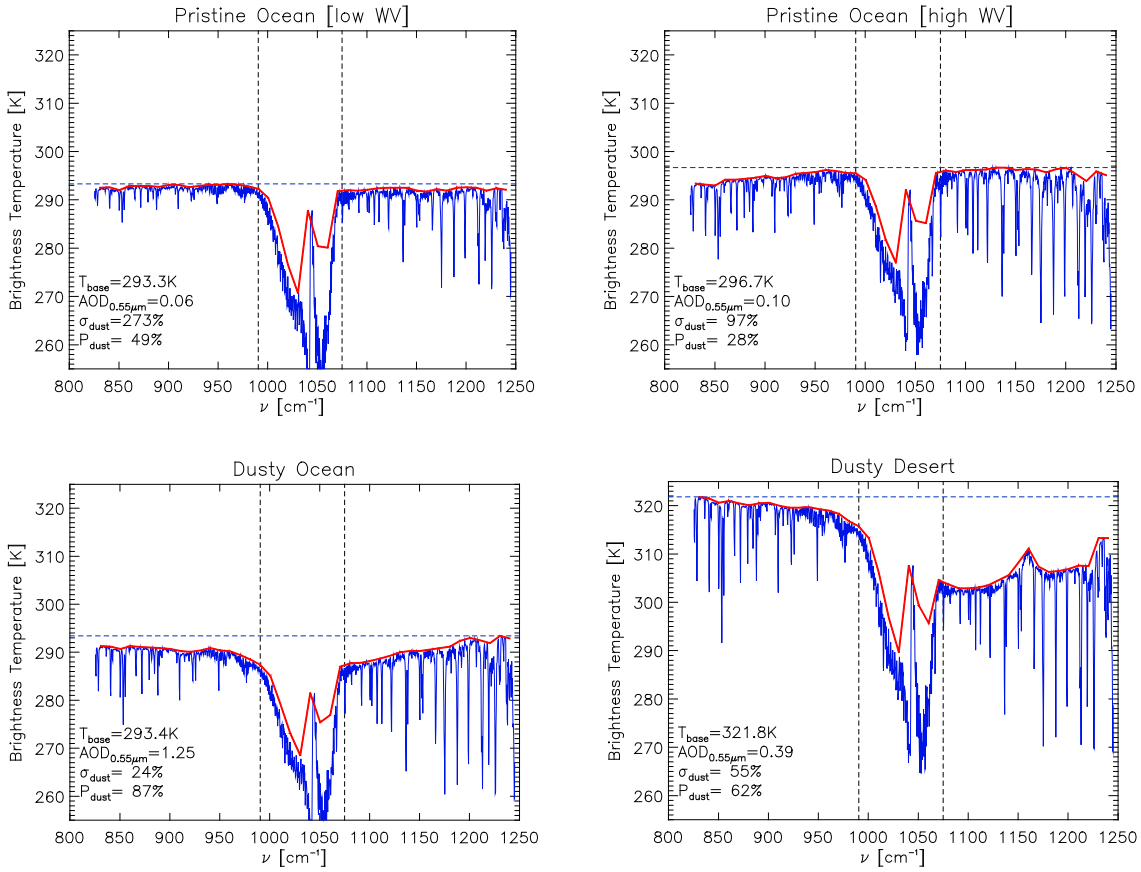

Fig. 10: IASI example brightness temperature spectra in full (blue) and reduced (red) resolution for observations over pristive ocean with low water vapour (top left), and high water vapour (lop right) as well as dust observations over ocean (bottom left) and desert (bottom right). All observations are from descending overpasses over the Atlantic Ocean, the Sahara and the Arabian Peninsula on June 4, 2009. The dashed blue line represents the baseline temperature, moreover retrieved AOD (at 0.55µm), retrieval uncertainty and dust probability are provided for the respective observations. The retrieval steps to obtain these numbers are explained in detail below. The positions where the observations have been taken are indicated in Fig. 11. Dashed black lines (vertical) represent the delimiters of the O_3 absorption band (e.g. *Clarisse et al.*, 2013). All retrieval steps are only performed outside this band.

assumption that reflected downwelling radiation may be neglected is not longer valid in eq. (18). Consequently the seven bins between 990cm^{-1} and 1070cm^{-1} are not used for PCA and for dust retrieval reducing the number of useful bins to 35.

In Fig. 10 the impact of desert dust on brigthtness temperature spectra is already clearly evident. While the main extinction within the ozone band is masked by the strong O_3 absorption, the reduced brightness temperatures at the shoulders of the ozone band (in contrast to the pristine observations) points towards the silicate extinction band. On the other hand by comparing the dusty ocean and desert observations also the impact of desert surface emissivity, i.e. the well pronounced quartz sand feature around 1160cm^{-1} (e.g. *Salisbury and Wald*, 1992) can be seen.

From this 35-bin spectrum the baseline temperature T_{base} is determined as its overall maximum brightness temperature (dashed blue line in Fig. 10). It is assumed to represent the transmittant radiance at the weakest (dust) absorption and thus serves as initial guess for the effective surface temperature (including surface emissivity effects). For the pristine ocean observations with low water vapour in fig. 10 the brightness temperature of the reduced resolution spectrum does hardly deviate from

T_{base} throughout the whole window region (outside the O_3 band). Only IASI observations with T_{base} > 225K are used for dust retrieval, as it is assumed that lower baseline temperature clearly indicates the presence of deep convective cold cloud tops (e.g. *Aumann et al.*, 2011).

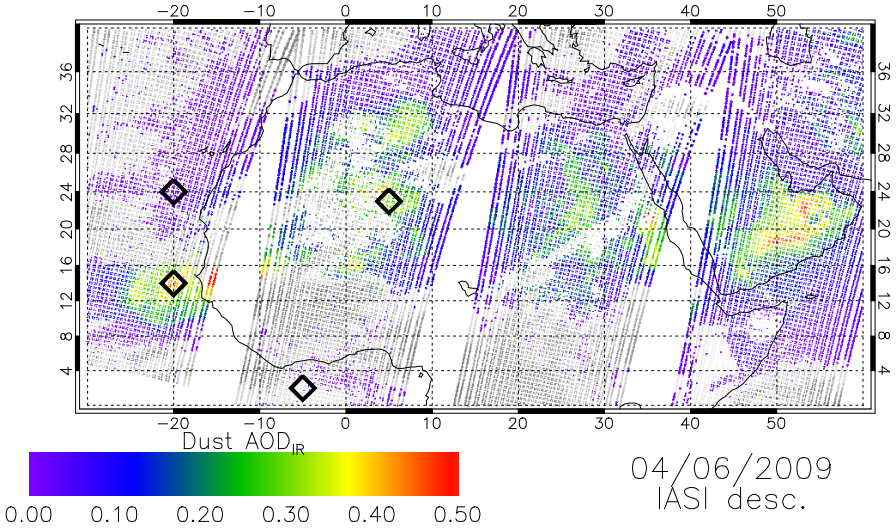

Fig. 11: IASI infrared dust AOD over Northern Africa from descending (morning) orbits of June 4, 2009. The four symbols indicate the observations for the example spectra in fig. (10)

Brightness temperature spectra then are transformed into a spectrum of a quantity τ_{eqv}, which can be regarded as an “equivalent optical depth” (and which is similar to the optical depth in the oversimplified radiative transfer equation eq. (23)):

$$L_{sat}(\nu) = e^{-\frac{\tau_{eqv}(\nu)}{\mu}} B_{\nu}(T_{base}) \qquad (28)$$

τ_{eqv} still contains significant pieces of information about surface emissivity and water vapour. Moreover in the calculation of τ_{eqv}, any atmospheric emission (and upwelling reflected radiation) is neglected and thus also contributes to the deviation of τ_{eqv} from true atmospheric optical depth (e.g. *Ackerman*, 1997), hence the description as "equivalent" optical depth, as it is not true optical depth (*Ackerman*, 1997 describes the exponential in eq. (22) as "effective transmissivity" which includes the same assumptions and approximations as done here).

6.3.4 Determination of Eigenvectors

From IASI observations with T_{base} > 225K over Southern Europe, Northern Africa, the Arabian Peninsula and adjacent oceans (0°N–50°N and 30°W–70°E) covering all four seasons of 2009, a principal component analysis has been performed for τ_{eqv}

spectra. The days included in the PCA are ten days (5-15) of March, July, September and December of 2009, respectively. Consequently the PCA is performed for IASI spectra over the given domain from 40 days, resulting in the use of 448462 spectra.
The large spatial domain provides a lot of different conditions of all types, ranging from snow covered cold surfaces to hot desert surfaces and high atmospheric moisture in the tropics. Thus the set of Eigenvectors represents a very broad range of atmospheric conditions. The Eigenvectors have been determined using the LAPACK libraries for solution of linear algebra problems (*Anderson et al.*, 1999).
The principle component analysis provides a set of 35 Eigenvectors $V_{i\leq 35}$ forming a basis of the spectral space.
This principle components approach allows for the retrieval being run in the same way for all suitable observations over land, ocean and (water-) clouds regardless of solar illumination.
As also spectrally small scale differences in the extinction spectra point to important information (e.g. differentiation between clays by the Al-Al-OH resonance peak or differentiation of particle size), the leading eight basis vectors are used for dust retrieval; they are presented in fig. 12 The leading two singular vectors mainly represent typical shapes of surface emissivity spectra of bare and partly vegetated soils (e.g. *Salisbury and Wald,* 1992; *Hulley et al.*, 2009) and also include water vapour absorption (compare Fig. 10).

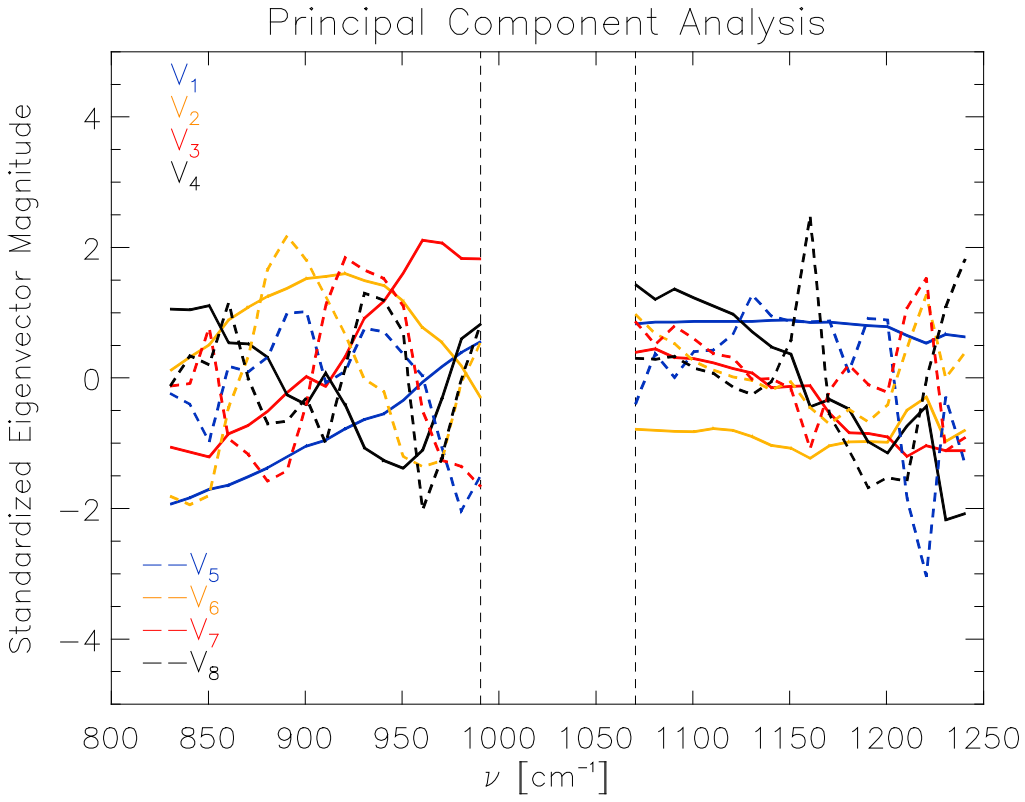

Fig. 12: Leading eight principle components (Eigenvectors) obtained from the 448462 IASI τ_{eqv} spectra. The gap between the dashed lines marks the strong O_3 absorption band, where no dust information is retrieved.

6.3.5 Inversion of AOD and effective radius from τ_{eqv} spectra

Although over deserts dust aerosol and surface (rocks, sand, barren silicate soils) are composed of widely the same material (silicates), surface emissivity spectra and dust extinction spectra can be separated, as the particle or agglomerate size has large effects on the spectral shape of the emitted and transmitted spectrum (e.g. *Salisbury and Wald*, 1992). Small particles like dust aerosol tend to reduce the spectral contrast of vibrational reststrahlen bands in typical desert minerals, consequently the radiance observed from satellite is differently modified by surface emissivity and airborne dust extinction (*Salisbury and Wald*, 1992; "small" in this context means within the Mie scattering regime, not absorption in the Rayleigh limit (*Laksina et al.*, 2012)). While these spectral differences between surface emissivity and dust extinction may not be resolved from broadband instruments (like AVHRR or MODIS), high-resolution spectrometers like IASI provide the opportunity to separate surface and dust signals (see example spectra in Fig. 10).
In a first version of the retrieval dust optical properties from the OPAC database had been used for characterising dust extinction spectra (see Tab. 1).
Instead of spectra solely based on sample based bulk dust refractive indices, mineral component extinction spectra for eight typical dust components and three typical dust size distributions are used here. The dust components for the retrieval are from quartz, illite, kaolinite, montmorillonite (smectite), chlorite, plagioclase feldspar, anhydrite and calcite. Extinction coefficients, extinction efficiency and single scattering albedo are simulated with Mie theory (*Quenzel and Müller*, 1987). Particle size distributions from three different field-campaigns in Northern Africa are used to represent different stages of dust transport. During the FENNEC campaign in June 2011 dust samples were collected over the Western Sahara source region including very large particles (*Ryder et al.*, 2013). The SAMUM-1 (Saharan Mineral dUst experiMent) campaign took place in 2006 in Morocco and dust samples represented dust still close to the source (*Weinzierl et al.*, 2009). The particle size distribution collected during SAMUM did not cover particles as giant as observed during FENNEC and thus represents an interim size mode. The third campaign providing an estimated of the dust particle size distribution was the GERBILS (Geostationary Earth Radiation Budget Intercomparisons of Long-wave and Shortwave radiation) campaign in 2010. (*Johnson and Osborne*, 2011). Particles collected during GERBILS were considerably smaller than those observed during SAMUM and compared well to particle size distributions from several other campaigns (*Johnson and Osborne*, 2011). Moreover dust extinction spectra simulated with GERBILS and submicron only (*McConnell et al.*, 2008) size distributions assuming Mie theory did not vary in shape (while of course they did for magnitude of the extinction coefficients), indicating that dust particles from those transport mode size range are close to the Rayleigh limit where single scattering albedo becomes very low and extinction is almost exclusively dominated by absorption (e.g. *Yang et al.*, 2007). Consequently the three size distributions cover the full transport cycle of the dust with abundance of giant particles at the source region, interim size distributions closely downwind and small particles approaching the Rayleigh limit during far-range transport. All four dust particle size distributions are represent by a set of four lognormal distributions representing different modes in the overall size distribution (*Weinzierl et al.*, 2009; *Johnson and Osborne*, 2011; *Ryder et al.*, 2013).
Table 2 lists the sources of refractive indices used in the Mie calculations. In tables below these eight mineral components will be described by the following

abbreviations: qz = quartz, il = illite mica, ka = kaolinite; mo = montmorillonite; cl = chlorite; fs = feldspar; ah = anhydrite; ca = carbonates (calcite).

Tab. 2: References for optical constants of mineralogical dust components.

qz	il	ka	mo	cl	fs	ah	ca
Spitzer and Kleinman (1961)	*Glotch et al.* (2007)	*Glotch et al.* (2007)	*Glotch et al.* (2007)	*Koike and Shibai* (1990)	*Aronson et al.* (1979)	*Marzo et al.* (2004)	*Orofino et al.* (2002)

All extinction spectra are normalised to their averaged value at 925cm^{-1} (Al-Al-OH peak) and 1125cm^{-1} (SiO peak).
Table 3 presents the mineralogical composition of dust samples reported in the literature. The Chinese dust is reported in *Jeong* (2008), the Iran sample is from *Rashki et al.* (2012), Kuwait from *Kahlaf et al.* (1985), Israel from *Foner* et al. (1992), the Central Sahara sample is reported in *Laksina et al.* (2012), Nigeria from *Adedokun et al.* (1989), the composition of Moroccan dust was analysed in the SAMUM-1 campaign and reported in *Kandler et al.* (2009) and the dust composition over the tropical Atlantic ocean has been described by *Claccum and Prospero* (1980).
While this list of minerals does not cover all mineral species occurring in desert dust, it well represents the majority of minerals observed in dust samples from North Africa and Asia (see also *Sokolik and Toon*, 1999; *Shao et al.*, 2007; *Kandler et al.*, 2011; *Wagner et al.*, 2012). Although hematite and goethite are especially important for absorption at solar wavelegths, the iron oxides do not provide useful spectral variability between 800cm^{-1} and 1200cm^{-1}, which makes it hard to retrieve information about them in the current method (e.g. *Sokolik and Toon*, 1999).

Tab. 3: Examples for the mineralogical composition of dust samples reported in the literature.

	Quartz	***Illite / Musc.***	***Kaol.***	***Montm.***	***Chlorite***	***Anhydr.***	***Carb.***	***Felds.***
China	19,5%	19,3%	2,4%	15,7%	2,8%	0.3%	7,5%	9,9%
Iran	39,8%	10,1%	N/R	N/R	6,3%	2,0%	23,8%	17,3%
Kuwait	27,3%	4,0%	0,4%	2,1%	0,1%	6,0%	40,2%	9,1%
Tel Aviv	23,0%	N/R	N/R	N/R	N/R	2,0%	70,0%	5,0%
C. Sahara	1,4%	31,3%	16,2%	33,6%	N/R	N/R	8,8%	8,7%
Nigeria	70,2%	2,3%	11,0%	N/R	N/R	N/R	N/R	16,5%
Morocco	24,0%	27,0%	4,0%	N/R	3,0%	N/R	14,0%	28,0%
Trop. Atl.	14,2%	62,1%	7,1%	N/R	4,2%	N/R	6,9%	5,6%

Fig. 13 shows the eight extinction spectra used for dust retrieval with IASI for the three size distributions respectively. The spectra are normalised to extinction optical depth of one (averaged extinction at 925cm^{-1} and 1125cm^{-1}). Again the two black dashed lines at 990cm^{-1} and 1070cm^{-1} are delimiters of the predominant O_3 absorption band not used for dust retrieval. It is clearly evident that the extinction peaks for most silicates are found within the O_3 absorption band. Nevertheless, the dust extinction at resonance band shoulders outside the O_3 absorption is still sufficiently high for dust AOD quantification – which is even more promoted by the presence of scattering for larger particles (SAMUM and FENNEC distributions). Also the secondary Al-Al-OH extinction peak highly contributes to the detectability of silicate dust in the spectra, especially well pronounced for kaolinite, as well as the calcite absorption peak around 875cm^{-1}.

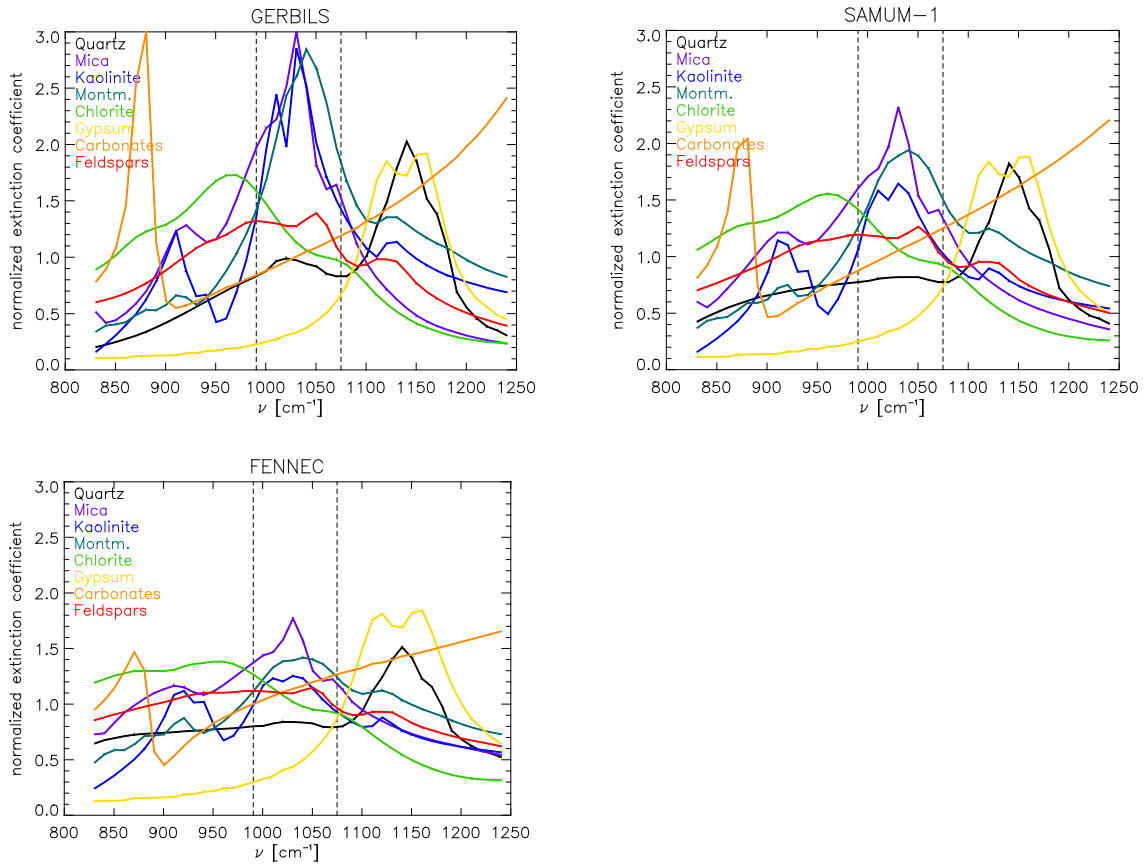

Fig. 13: Normalized extinction coefficient spectra of the eight mineral components in the three size modes used in the IASI retrieval.

It is clearly evident that the spectral contrast in all spectra is highest for the transport mode (GERBILS size distribution), i.e. approaching the Rayleigh limit, and lowest (but still well pronounced) for the large particles, where scattering strongly reduces the spectral contrast (*Salisbury and Wald*, 1992).

The weights w_i of the respective Eigenvectors V_i are calculated as the scalar products of respective Eigenvectors and τ_{eqv} spectra (e.g. *Bretherton et al.*, 1999; *Rodgers*, 2000):

$$w_i = \sum_{\nu} V_i(\nu) \cdot \tau_{eqv}(\nu) \tag{30}$$

where i denotes the number of the corresponding Eigenvalue and Σ_ν is the sum over all 35 spectral bins. As already outlined in section 6.3.3, the leading two singular vectors are dominated by surface emissivity together with water vapour absorption. The dust signal is thus analysed from the Eigenvectors three to eight.
The Eigenvectors V_i with $3 \leq i \leq 8$ span a subspace of the observation

$$\tau_{ev}(\nu) = \sum_{i=3}^{8} w_i \cdot V_i(\nu) \tag{31}$$

to which the observed equivalent optical depth can be projected analoguously to eq. (30).
For each of the three size modes S_j now the probability of each component C_i to represent the dust spectrum is calculated independently. The initial weight of each component is determined by the normalized projection

$$\varphi_{comp}(C_i|S_j) = \frac{\sum_\nu \tau_{ev}(\nu) \cdot \tau_e(C_i, S_j, \nu)}{\sqrt{\sum_\nu (\tau_{ev}(\nu))^2} \cdot \sqrt{\sum_\nu (\tau_e(C_i, S_j, \nu))^2}} \tag{32}$$

The normalization guarantees that $-1 \leq \varphi_{comp}(C_i|S_j) \leq 1$, a projection of $\varphi_{comp}(C_i|S_j)=0$ indicates orthogonality of the vectors and hence no information on component C_i to be contained in τ_{ev}. The projection is similar to Pearson product-moment correlation (*Pearson and Hartley*, 1972), which in fact is the normalized projection of centralized vectors, i.e. the mean value of the vector substracted (*Schönwiese*, 2006). Consequently normalized projection may equally be interpreted as (qualitatively) signifying the covariance between vectors (e.g. *Menke*, 2012).
Negative values of $\varphi_{comp}(C_i|S_j)$ are set to 0 in order to not account for these (physically not reasonable for interpreting composition and AOD) signals in the retrieval.
As the extinction spectra of the different components are highly correlated, Bayes' theorem (developed from *Bayes*,1763) is used in order to update the probability of component C_i with the evidence from the observations. Here the notion of Bayes' theorem by *Silver* (2012) is used (which is equivalent to that of *D'Agostini*, 1995). Given the a priori probability of an event $P_x(E)$, the a posteriori evidence $P_y(E)$ and the probability of the prior being false, $P_z(E)$, the updated Bayesian probability of the event is given by:

$$P_B(E) = \frac{P_x(E) \cdot P_y(E)}{P_x(E) \cdot P_y(E) + P_z(E) \cdot (1 - P_x(E))} \tag{33}$$

If the event E considered in eq. (33) is the abundance of component C_i under the assumption of size mode S_j, $P_B(E)$ can be written as $P_B(C_i|S_j)$. The normalised projection $\varphi_{comp}(C_i|S_j)$ represents the a priori estimate of the component's abundance probability in the give size mode S_j, $P_x(C_i|S_j)$ in eq. (33), while the probability $\varphi_{max}(C_i,S_j)$ that any linear combination from Eigenvectors three to eight can

reproduce the extinction spectrum of component C_i at size mode S_j provides the "model accuracy" $P_y(C_i|S_j)$ following *Menke* (2012). The weights of the linear combination of the Eigenvectors is determined from $\tau_e(C_i,S_j,\nu)$ with eq. (30).
Consequently $P_z(E)$ can be represented by the probability of the dust signal not being contained in the respective eigenvectors, i.e.

$$P_z(C_i|S_j) = 1 - P_y(C_i|S_j) \tag{34}$$

Consequently

$$P_B(C_i|S_j) = \frac{P_x(C_i|S_j)\cdot P_y(C_i|S_j)}{P_x(C_i|S_j)\cdot P_y(C_i|S_j) + \left(1-P_y(C_i|S_j)\right)\cdot\left(1-P_x(C_i|S_j)\right)} \tag{35}$$

is the Bayesian probability for each component C_i representing the dust with size mode S_j and is evaluated for all six C_i and for all four S_j.
Having determined the componentwise abundance probability for each size mode, the representation probability of the size modes is determined from $P_B(C_i|S_j)$ by

$$P_B(S_j) = \frac{\sum_{i=1}^{8} P_B\left(C_i|S_j\right)}{\sum_{j=1}^{3}\sum_{i=1}^{8} P_B\left(C_i|S_j\right)} \tag{36}$$

Normalization of $P_B(C_i|S_j)$ (e.g. *D'Agostini*, 1995; *Menke*, 2012) yields the fraction of dust component C_i and size mdoe S_j for the further retrieval steps:

$$\Phi\left(C_i,S_j\right) = \frac{P_B\left(C_i|S_j\right)}{\sum_{j=1}^{3}\sum_{i=1}^{8} P_B\left(C_i|S_j\right)} \tag{37}$$

The sum of weighted Bayesian probabilities for components and size modes yields the probability that the observation really represents mineral dust:

$$P_{dust} = \sum_{j=1}^{3}\sum_{i=1}^{8} \Phi\left(C_i,S_j\right) P_B\left(C_i|S_j\right) \tag{38}$$

From the size dependent component dust extinction spectra $\tau_e(C_i,S_j)$ now a dust extinction spectrum assumed to best represent the observed conditions is calculated as

$$\tau_{dust}(\nu) = \sum_{j=1}^{3}\sum_{i=1}^{8} \Phi\left(C_i,S_j\right)\cdot \tau_e\left(C_i,S_j,\nu\right) \tag{39}$$

Now the dust infrared AOD (AOD_{IR}, evaluated as the average AOD at 925cm^{-1} and 1125cm^{-1}) can be estimated as

$$AOD^*(\nu) = \left(\sum_{i=1}^{8} \sum_{j=1}^{3} \Phi(C_i, S_j) \cdot \sum_{\nu} \tau_{ev}(\nu) \cdot \tau_e(C_i, S_j, \nu) \right) \quad (40)$$

Provided AOD*(ν) together with $\omega_0(\nu)$ and g(ν) eq. 21 can be solved for T_{dust} (e.g. *Pavolonis et al.*, 2013).
Ackerman (1997) also shows that the effective transmissivity is reduced by aloft dust layers and that the retrieval is likely to overestimate optical depth. The overestimation can be corrected for applying eq. (21) with the determined value of T_{dust}:.

$$AOD_{IR} = \left(e^{-AOD'_{IR}} - \left(e^{-AOD'_{IR}}\right) \frac{B_{IR}(T_{dust})}{I_{sfc}(IR)} \right) \quad (41)$$

where "IR" denotes the average over 925cm^{-1} and 1125cm^{-1} as above and AOD'$_{IR}$ is the infrared scaled AOD obtained from eq. (40), i.e. uncorrected the AOD*.
In a final step infrared dust AOD is transfered to standard visible AOD (at 0.55µm) in order to achieve comparability with solar AOD observations. *Dufresne et al.* (2002) determined the relationship between longwave IR and shortwave visible optical depth by radiative transfer simulations using dust optical properties of *Volz* (1973) originating from a low-iron Saharan dust sample collected after long range transport in Barbados. The transfer coefficients of *Clancy et al.* (2003) for iron-rich clay dust on Mars show significant differences to those of *Dufresne et al*. (2002) due to the dust composition. Table (4) lists the transfer coefficients $\gamma(C_i,S_j)$ between infrared and visible AOD (at λ=0.55µm) for all eight components and three size modes calculated with Mie theory. Also for the extinction coefficients at visible wavelengths component-dependent refractive indices have been used (compiled by *Alexander et al.*, 2013). The particle size dependence of the TIR-to-VIS transfer coefficients is clearly visible.

Tab. 4: Coefficients for transfer from TIR to 0.55µm for different particle size distributions and dust components.

	qz	**il**	**Ka**	**mo**	**cl**	**fs**	**ah**	**ca**
GERBILS	8.080	5.270	5.304	3.111	7.147	7.630	7.549	5.243
SAMUM	2.641	1.851	1.829	1.173	2.572	2.605	2.478	1.820
FENNEC	1.120	0.933	0.886	0.668	1.165	1.125	1.066	0.898

$$AOD_{VIS} = \sum_{j=1}^{3} \sum_{i=1}^{8} \left(\Phi(C_i, S_j) \cdot \gamma(C_i, S_j) \right) \cdot AOD_{IR} \quad (42)$$

Fig. 14 exemplarily shows dust optical depth at 0.55µm as retrieved from IASI descending orbits (daylight overpasses) for June 4, 2009 over Northern Africa and Arabia. Strong dust activity in the western Sahel connected to the presence of mesoscale deep convection provides support for a dust plume over the Atlantic Ocean in the West with high dust optical depths over the ocean. Another region with high dust activity is northern East Africa along the coast of the Red Sea. Moreover dust is transported from the Arabian Peninsula twoards the Arabian Gulf and the Indian Ocean South of Yemen and Oman. Increased dust loads also can be observed over wide parts of the Sahara desert (especially over the Western Sahara). Background greyscale represents the mean temperature of the broadband IIS imager

for the respective IASI pixels. Dark grey indicates low temperatures (clouds) and brighter shades of grey represent high temperatures. No dust AOD is presented where ice clouds are detected (i.e. the Bayesian probability for ice cloud is higher that that for dust).

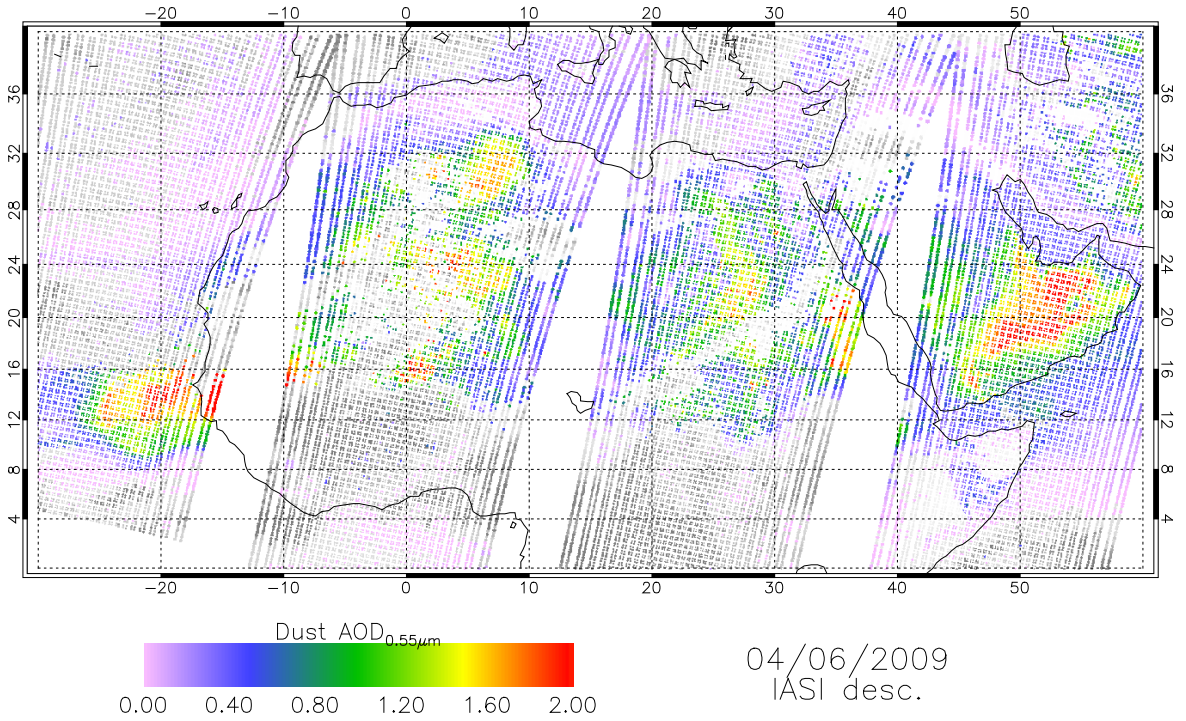

Fig. 14: IASI dust $AOD_{0.55\mu m}$ over Northern Africa from descending (morning) orbits of June 4, 2009.

6.3.6 Intrinsic and external uncertainties

Following Bayesian probability theory the overall probability of airborne mineral dust is

$$P_{dust} = \sum_{i=1}^{8} \sum_{j=1}^{3} P_J\left(C_i, S_j\right) \tag{43}$$

This dust probability is linked to an AOD, i.e. the retrieved AOD_{IR}, as well as to a range of possible AOD (for each single component and size; averaged over 925cm^{-1} and 1125cm^{-1}) values determined by

$$AOD_{comp}\left(\mathrm{C_i}, \mathrm{S_j}\right) = \sum_{\nu} \tau_{ev}(\nu) \cdot \tau_e\left(\mathrm{C_i}, \mathrm{S_j}, \nu\right) \tag{44}$$

Consequently the standard deviation $\sigma(AOD_{IR})$ of possible AOD_{IR} in eq (44), i.e. the standard deviation of component- and sizemode-wise AOD_{IR}, provides the AOD uncertainty in the retrieval brought about by the selection of dust components and size modes. Nevertheless $\sigma(AOD_{IR})$ does not represent the retrieval accuracy which has to be obtained from validation with independent data.
The retrieval is moreover subject to a range of uncertainties which cannot as easy be quantified. One of the most obvious uncertainties is the absence of iron oxides (which widely control absorption at solar wavelengths) in the retrieval composition, as those lack significant extinction peaks in the spectral domain of the retrieval. Consequently it is expected that true dust optical depth is underestimated by the retrieval, especially at solar wavelengths (*Sokolik and Toon*, 1999).
Additional uncertainties are introduced by the spectral binning of the IASI observations in regions with strong spectral slopes of extinction bands and the effect of dust layer height respective temperature difference between dust layer and surface (*Ackerman*, 1997). Assuming a typical dust mixture (*Sokolik and Toon*, 1999) and a typical dust size distribution (from GERBILS, *Johnson and Osborne*, 2011) the maximum impact of spectral binning on retrieved infrared AOD can be tested assuming a totally transparent atmosphere and blackbody emission of the surface in eq. (21). Results for two different infrared AOD, three surface temperatures and four dust layer temperatures are presented in table (5). While surface temperature is approached by the retrieval estimate T_{base} quite well at low and moderate optical depths (0.1 and 0.5, respectively) and moderately low surface temperature (270K), it is significantly underestimated (by up to 10K) at high optical depth (1.0) and high surface temperature (310K). If dust layer temperature is greater than or equal to the surface temperature all signal is lost (see also *Ackerman*, 1997) and significantly underestimated at low temperature differences between dust layer and surface. As also pointed out by *Ackerman* (1997) AOD is overestimated when the temperature contrast between surface and dust layer is high. The wavenumber shift itself introduces errors in the magnitude of 0.003 to 0.010 in AOD units at infrared AOD of 1.0 and thus can be neglected in the uncertainty assessment. The same is true for uncertainties brought about by the instrument accuracy which is about 0.1K and can be neglected in contrast to the uncertainties from the T_{base} estimation.

Tab. 5: Sensitivity of retrieved AOD_{IR} to temperature contrast between surface and dust layer.

AOD_{IR}	**0.1**	**0.1**	**0.1**	**0.1**	**1.0**	**1.0**	**1.0**	**1.0**
T_{dust}	**230K**	**250K**	**270K**	**290K**	**230K**	**250K**	**270K**	**290K**
T_{sfc}=270K	0.148	0.083	0.000	0.000	0.927	0.438	0.000	0.000
T_{sfc}=290K	0.180	0.134	0.074	0.000	1.250	0.803	0.379	0.000
T_{sfc}=310K	0.200	0.166	0.121	0.065	1.498	1.098	0.701	0.331

One of the largest uncertainties which cannot easily be assessed is the remaining impact of the surface emissivity spectrum. Although most of the emissivity signal is contained in the leading two Eigenvectors, the mathematically orthogonal set of Eigenvectors does not fully separate the spectral features by physical processes. Consequently surface emissivity information is also contained in higher order Eigenvectors. Moreover the dust extinction spectra used in the retrieval are reproduced by the Eigenvectors three to eight with magnitudes between 30% for the largest size mode and 50% for the smallest size mode (depending on component*).* The remainder of the dust information is contained mainly in the leading two

Eigenvectors, which unfortunately are dominated by surface emissivity and thus cannot easily be used for dust retrieval. Consequently it has to be assumed that the information contained in the Eigenvectors three to eight is sufficient for estimating dust optical depth with variable particle size and composition. Especially for large particles this assumption may be quite wrong. Moreover for large particles near dust sources the spectral contrast of dust extinction within the window region is rather low (fig. 13), severely affecting the potential of dust detection with this spectral pattern matching method. From table (5) it also can be concluded that nighttime inversion layers (e.g. *Ashpole and Washington*, 2012) will cause great uncertainty in retrieval results as in those cases dust layer temperatures often exceed surface temperature.
Solar illumination contributes around 0.5% to the observed radiance in the thermal infrared window region (*Petty*, 2006). As only the scattered part of the solar illumination would affect the retrieval and single scattering albedo of mineral dust is rather low for most particle sizes (*Yang et al.*, 2007) the uncertainty introduced by solar contributions at daytime overpasses is small compared to the other uncertainties and thus may be neglected.
One uncertainty not at all addressed so far is the potential presence of volcanic ash. As volcanic ash also is mainly made of silicates it has similar extinction features in the thermal infrared like desert dust (e.g. *Pavolonis et al*., 2013). Thus volcanic ash would also be identified as dust with this retrieval and would add to the total observed dust, while due to different composition the quantitative AOD might be severely wrong in the case of volcanic ash (see *Pavolonis et al*., 2013). Fortunately during the year 2009 being used here no severe volcanic eruption appeared in the regions addressed and thus volcanic ash impacts (in those specific regions and that year) may be neglected in the analysis.

6.4 Validation of dust AOD

Fig. 15 shows time series of IASI and sun-photometer AOD of March and April 2009 exemplary for the AERONET station at Cinzana in Mali (13°16'N, 5°55'W). IASI observations within 50km distance to the AERONET station are included as blue diamonds in the plots. Taking 50 km as maximum distance to ground based observations has proven a very good distance threshold, e.g. by a variogram analysis of AERONET observations versus satellite data (*Holzer-Popp et al.*, 2008). AERONET observations are coarse mode AOD at 0.5µm processed with the Spectral Deconvolution Algorithm (SDA, *O'Neill et al.*, 2003), each symbol represents an hourly mean. In the SDA algorithm coarse mode AOD has been shown to also be sensitive to the presence of thin semitransparent clouds and thus partly tends to overestimate true AOD of the coarse mode aerosol fraction (*O'Neill et al.*, 2003). Significant dust events like for example end of April are well represented by the IASI dust observations, both qualitatively and quantitatively (in terms of $AOD_{0.5\mu m)}$.
There is a generally high agreement between IASI and AERONET observations in the temporal evolution of dust respective coarse mode aerosol activity over the AERONET stations. Nevertheless it is also clearly evident that sometimes dust is not observed by IASI at all (partly due to obscuring clouds) and at Cinzana dust optical depth at visible wavelengths is partly underestimated compared to AERONET, potentially due to the lacking representation of iron-oxide absorption at visible wavelengths in the IASI retrieval.

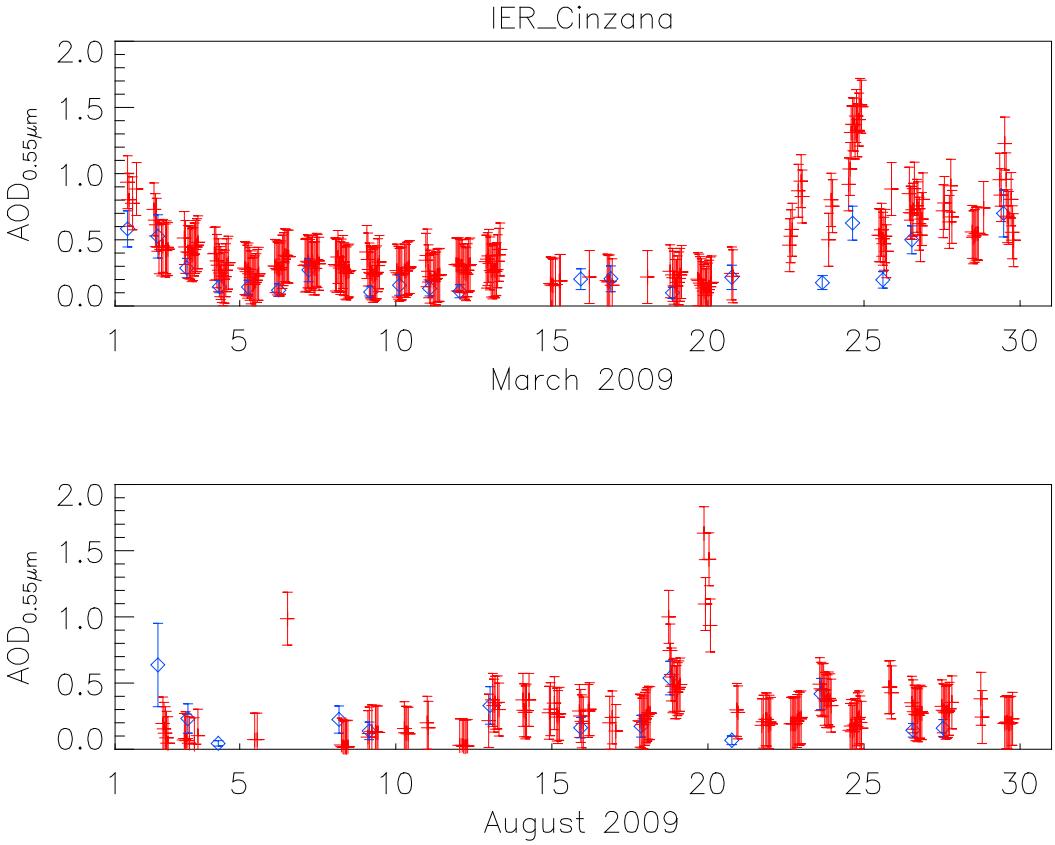

Fig. 15: Time series of AERONET coarse mode $AOD_{0.55\mu m}$ (red plus signs and ±0.2 margins) and IASI dust $AOD_{0.55\mu m}$ (blue diamonds with retrieved instrinsic uncertainty margins) at the AERONET station of IER Cinzana in Mali (13°16'N, 5°55'W) for March and August 2009.

Figure 16 presents the overall comparison of IASI dust observations with those of 32 AERONET stations in Africa, Southern Europe, Arabia and Central- and East-Asia for the year 2009. AERONET observations are coarse mode $AOD_{0.5\mu m}$. Each observation is the average over all data with maximum time difference of half an hour between AERONET observation and Metop (IASI) overpass, where AERONET observations are filtered by a minumum of at least three observations within the one hour time window and by standard deviation of those observations lower than 30% in order to guarantee representativity for the dust situation observed by IASI.
Error bars at the symbols indicate the intrinsic retrieval uncertainty, while the symbol colour represents the Ångström exponent α of the AERONET observation. The linear correlation (*Pearson and Hartley*, 1972) between IASI derived $AOD_{0.5\mu m}$ and AERONET coarse mode $AOD_{0.5\mu m}$ for all 32 stations is ρ=0.714, the root-mean-square difference (RMSD) is 0.169 and the bias -0.014. Of the 595 simultaneous observations of IASI and AERONET, 83% of IASI observations lie within $AOD_{0.5\mu m}$±0.2 of AERONET coarse mode $AOD_{0.5\mu m}$.
The correlation between AERONET AOD and IASI AOD at 0.5µm is higher than the one between the respective AERONET $AOD_{0.5\mu m}$ and the firstly retrieved dust AOD_{IR} of the IASI retrieval (ρ=0.623). It can thus be assumed that the size-dependent

transfer function has a positive impact on the observation results. Using a fixed transfer coefficient for the calculation of $AOD_{0.5\mu m}$ from AOD_{IR} thus would underestimate the impact of size distribution on the AOD spectrum. Moreover, correlating IASI dust $AOD_{0.5\mu m}$ with total AERONET $AOD_{0.5\mu m}$ yields ρ=0.667 and is thus weaker than with coarse mode AERONET AOD.

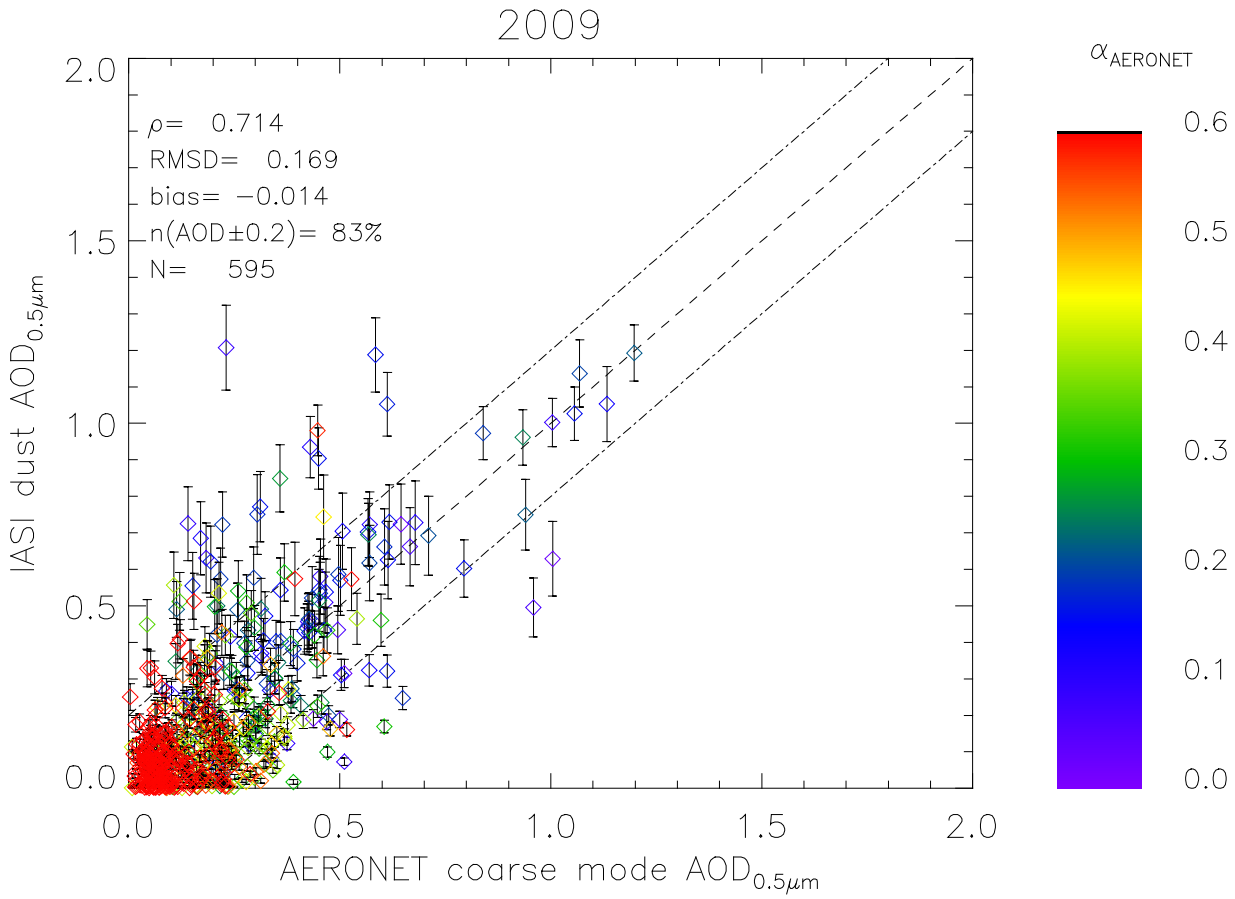

Fig. 16: Evaluation of IASI $AOD_{0.5\mu m}$ against AERONET coarse mode $AOD_{0.5\mu m}$ over Africa, Arabia and Asia for 2009.

In this case strong underestimation of AERONET total AOD by IASI is observed for high fine mode fractions. Despite the, for a desert dust retrieval over land (see e.g. *Carboni et al.*, 2012), generally good correlation between $AOD_{0.5\mu m}$ from IASI and AERONET (having in mind that the IASI retrieval is in TIR and AERONET AOD is from solar wavelengths and includes also sea salt) there is a range of outliers where the IASI retrieval strongly under- or overestimates AOD.
Underestimation may reflect the lack of information about iron-oxide content in the dust representation of the IASI retrieval, which will increase absorption at visible wavelengths while having hardly any impact on thermal infrared optical depth.
Moreover natural dust is composed of more than the eight components used in the IASI retrieval. On the other hand mineral dust contains also fine mode (particle size < 1µm) particles, especially after long-range transport and for clay-sized mineral abundance (*Markl*, 2008). In this case these dust particles may not be fully represented by the coarse mode AOD of AERONET (*O'Neill et al.*, 2003).

The evaluation with ground-based AERONET observations has also been used to address the impact of different influencing factors on retrieval results. Therefore the relative deviation between AERONET AOD and IASI AOD (both at 0.5µm) has been correlated with the viewing zenith angle, with the intrinsic retrieval uncertainty and the retrieved particle size (in terms of retrieved effective radius). The correlation coefficients are +0.04, +0.02 and -0.22 respectively. While only the last one (correlation with retrieved dust effective radius) does vary from zero, none of these correlations is significant. Consequently it can be concluded that neither viewing geometry nor retrieval uncertainty or retrieved effective radius impact on the accuracy of the retrieval results to any significant degree.

6.5 Application to ice clouds

Atmospheric water ice also can be retrieved from absorption differences in the 830-1250cm^{-1} region (e.g. *Yang et al.*, 2005; *Comstock et al.*, 2007). The spectral differences of ice absorption in the atmospheric window are commonly used for cirrus detection in cloud screening algorithms (e.g. *Kriebel et al.*, 1989). Thus the ice absorption spectrum can also be exploited for ice cloud remote sensing from IASI. Whereas the impact of water vapour and CO_2 absorption on observation spectra in the infrared window region further decreases with increasing cloud top height (at least for sufficiently opaque clouds), the stratospheric O_3 absorption is not affected by cloud top height. Consequently the O_3 absorption band between 1000cm^{-1} and 1075cm^{-1} also cannot be used for ice cloud remote sensing.
Ice absorption spectra are provided by *Yang et al.* (2005) for different ice particle effective diameters between 5µm and 100µm. The definition of ice cloud effective radius in *Yang et al.* (2005) follows *Ebert and Curry* (1993), consequently it is also the ice effective diameter definition applicable to IASI retrieval results.
With these ice absorption spectra the methodology of IASI dust retrieval can directly be applied to ice clouds. Nevertheless the high opacity of thick ice clouds limits all IR methods to IR optical depth below about 10, as the radiance signal for higher optical depth saturates and observed radiance is more or less purely originating from cloud top emission (*Petty*, 2006; *Comstock et al.*, 2007; *Hong et al.*, 2010). Thus for optical depth below 10 it is possible to retrieve ice cloud optical depth and effective diameter simultaneously. A maximum saturation optical depth of 10 is used here, although also higher values result from the retrieval in specific cases.
Ice water path can be retrieved from optical depth and effective diameter. Above cloud saturation retrieval of optical depth is still possible, but it does not longer represent ice optical depth of the total cloud. Infrared optical depth is transfered to visible wavelengths following the method described in *Heymsfield et al.* (2003).
Comstock et al. (2007) define three classes of ice clouds: thin cirrus (τ_{ice}<0.3), optically thicker ice clouds (0.3<τ_{ice}<5.0) and optical thick deep convective clouds (τ_{ice}>5.0). For the latter no reliable optical depth retrieval is possible from IR observations. As the MODIS detection limit is τ_{ice}>0.4 (*Ackerman et al.*, 2008), this value is used here as lower threshold in consistency with MODIS.
The liquid water fraction of clouds cannot be analysed with this kind of method, as spectral extinction / emission of liquid water droplets does hardly vary over the IR window. Thus spectral extinction shape or contrast cannot be used to infer water cloud properties from the spectral observations without explicit knowledge of surface-leaving radiance. Even then optical depth retrieval for opaque liquid water clouds is

not possible from thermal infrared. Also liquid water effective radius cannot be determined from IR window observations alone.
Figure 17 shows how IASI retrieved ice cloud CTT compares to MODIS level 2 ice cloud CTT for three days in August 2009 (daylight overpasses only). Especially for high CTT, IASI overestimates CTT, while it corresponds quite well for low CTT. Moreover the overestimation by IASI at high CTT may also result from inhomogeneous cloud scenes within one IASI pixel or from different classifications of cloud phase.

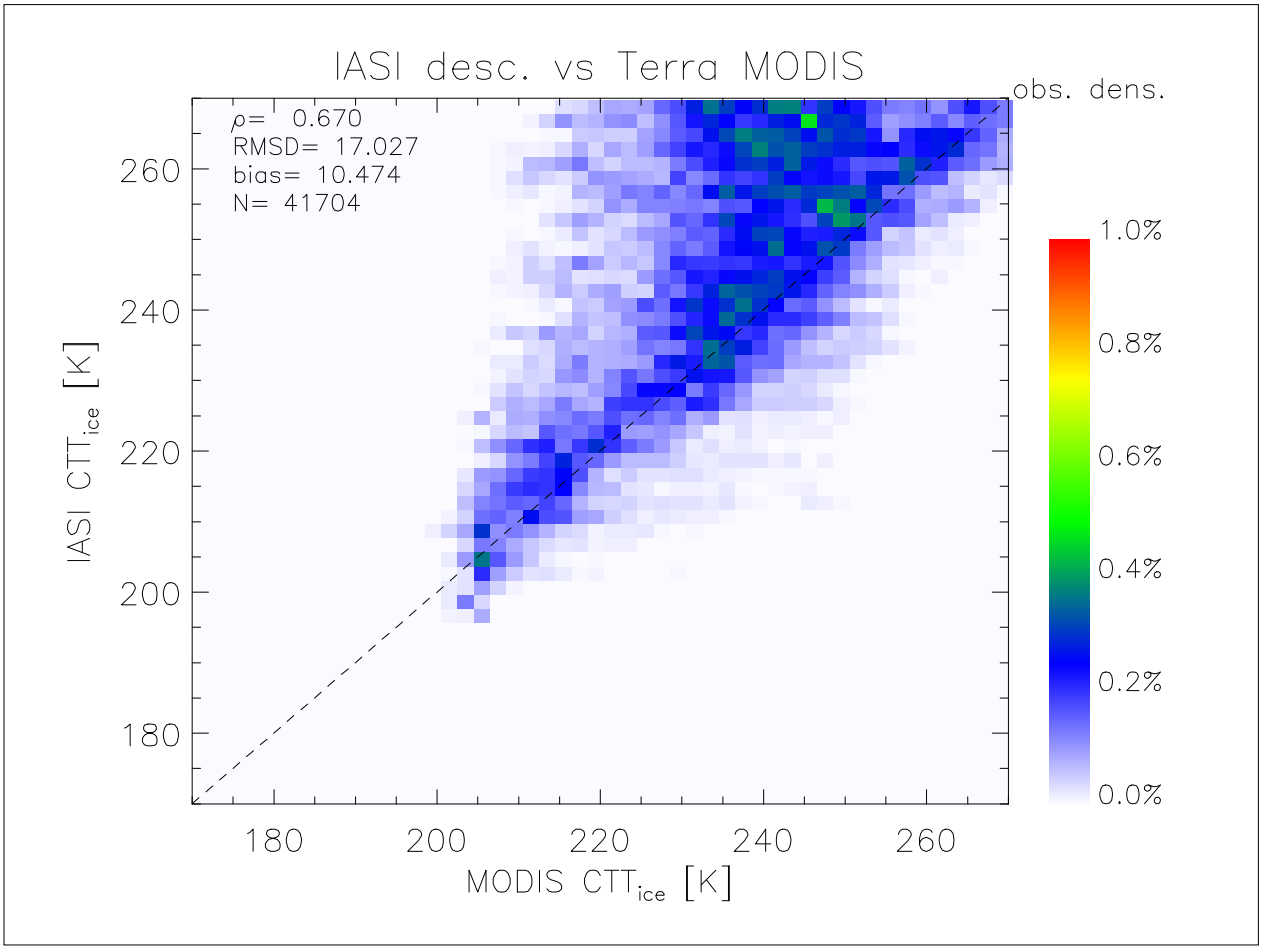

Fig. 17: Comparison of IASI retrieved ice cloud CTT with that of MODIS L2 ice cloud observations from 8-10 August 2009.

The corresponding comparison of IASI effective radius retrievals are only losely correlated (ρ=0.411) and especially at small ice crystal sizes IASI effective radius is much larger than that of MODIS. The RMSD is 8.29µm at a bias of 4.05µm from a sample size of 41707 co-registered observations. The observed differences between ice effective radius observed from IASI and from MODIS are subject to differences in retrieval method (look-up table for MODIS, spectral PCA for IASI), on the opacity limit for IASI (the cloud volumes responsible for the radiance observations are not the same), on the higher thin cloud fractions in IASI observations (infrared methods are more sensitive to thin cirrus than solar methods, e.g. *Comstock et al.*, 2007; *Broadley et al.*, 2012) and, of course, on the different pixel sizes (1km for MODIS, 12km for IASI). Moreover the comparison of *McFarquhar and Heymsfield* (1998) showed that for the same cloud the effective radius definition of *Fu and Liou* (1993), which is used

in the MODIS retrieval, results in lower retrieved effective radius than that of *Ebert and Curry* (1992), which is used in the IASI retrieval. Together with the significantly lower ice cloud optical depths observed by IASI due to the IR opacity limit the differences in effective radius result in uncorrelated (ρ=-0.002) observations of ice water path between MODIS and IASI with generally much lower IWP values for IASI observations than for MODIS, especially for optically thick clouds above the opacity limit of the IASI method.

7 Method for the quantification of indirect aerosol effects

So far only few attempts of large scale statistical quantification of indirect aerosol effects over land, and especially over semi-arid or arid regions, from satellite remote sensing are available (*Stevens and Feingold*, 2009). For example, *Koren et al.* (2008) and *Small et al.* (2011) correlate AOD with cloud cover and interprete the results as evidence for aerosol indirect effects. But this kind of analysis does not take into account microphysical properties of the clouds as observed from satelite and does also not seperate between different aerosol types. Interpretation of the results in *Small et al.* (2011) relies on vertical velocities simulated by numerical weather forecast models. Moreover the analysis is limited to liquid water clouds only, as in the majority of studies covering indirect aerosol effects.

Besides total aerosol also subsets for mineral dust and fine mode aerosol are analysed here. Cloud properties are averaged into 1°x1° grid boxes (ENVISAT and MODIS). IASI (only one year available) is analysed by means of 1°x1° running windows around each IASI observation.

The "background" aerosol load subset represents conditions with low aerosol influence. It is compiled from all gridboxes with 0<AOD<0.2. Total AOD is used as constraint for background conditions for MODIS and ENVISAT. As IASI is not sensitive to biomass burning aerosol, here the background can only be defined as observations with $0<AOD_{dust}<0.2$. Although e.g. *Koren et al.* (2008) and *Small et al.* (2011) report a significant relationship between cloud cover and AOD also for smaller AODs, AOD=0.2 is used as background constraint here in order to acount for different retrieval uncertainties.

The second aerosol load class ("moderate") is defined by aerosol thresholds of 0.2 (lower) and 0.75 (upper). For MODIS and ENVISAT, now the respective type AOD is used as defined in sections 5.1 and 5.2. Finally, the "high aerosol" class contains all observations with AOD>0.75.

Aerosol is observed under very different meteorological conditions in all test regions. Moreover convective clouds are mainly a result of high moisture supply. Dust and also biomass burning aerosol is preferentially observed in dry conditions. Thus, differences in statistical distributions of cloud properties between background and higher aerosol load cases also carry information about the difference in moisture supply. Microphysical properties of clouds such as effective radius are closely linked to the stage of convective development. Consequently the analysis of aerosol impact on cloud properties has to take into account the statistical distribution of cloud properties in dependence of the cloud top height.

Cloud top temperature is quite often used for estimating the vertical profiles of e.g. effective radius or other cloud property observations within the cloud (e.g. *Ramanathan et al.*, 2001; *Kaufman et al.*, 2002; *Rudich et al.*, 2003; *Yuan et al.*, 2011). *Ramanathan et al. (2001), Rosenfeld* (2001), *Rudich et al.* (2003) and others use diagrams of effective radius as a function of cloud top temperature in order to show aerosol influence on droplet size in several case studies (see fig. 5). The aerosol effect is respresented by the deviation of the aerosol-influenced profile from the background profile. It has been used so far mainly for case studies or well defined cloud regimes, most often limited to liquid water clouds (e.g *Ramanathan et al.*, 2001; *Rudich et al.*, 2003). Nevertheless this approach can also be used in statistical analysis at temporally and spatially large scales in order to characterise cloud properties and the impact of aerosols. Moreover, such an analysis approach can be applied to a wide range of cloud properties, not only to effective radius. It will be

described in detail in the following with the example of liquid water cloud effective radius in the Sahel observed from MODIS for total aerosol.
Firstly, cloud top temperature histograms are determined from all Sahel observations from for the three aerosol load classes "background" ("b", red), "moderate" ("m", black) and "high" ("h", blue). The CTT histograms are made up of 50 bins between 200K and 300K with 2K binwidth each. The histograms are depicted in Fig. 18, the annotations indicate the first three statistical moments (mean, variance, skewness) of the respective samples. For the "moderate" and the "high" aerosol class, the tag "Si_{95}" before the statistical moments indicates that the sample ditributions are statistically significant (at the 95% confidence level) different from the background. The significance of deviation from the background distribution is tested with a Wilcoxon-Mann-Whitney test (*Schönwiese*, 2006).

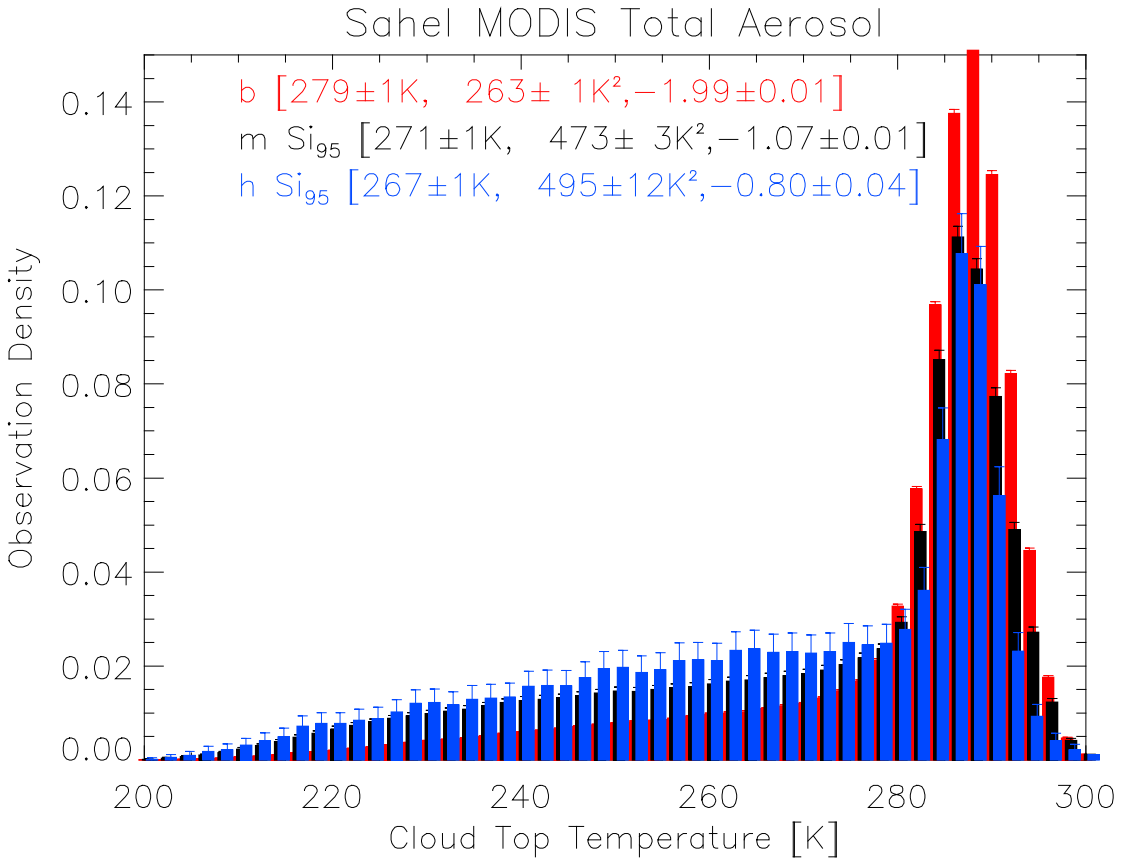

Fig. 18: Cloud top temperature histograms for total aerosol classes "background" (red), "moderate" (black) and "high" (blue) in the Sahel (from 2004-2009) together with the respective first three statistical moments of the samples.

The uncertainty of of the mean value (first statistical moment) is the maximum of the statistical error introduced by the finite sample size (*Schönwiese*, 2006) and the half bin width of the histogram, which in most cases is higher than the statistical error in the MODIS sample. It is clearly evident, that the CTT distributions from aerosol observations of the "moderate" and "high" classes significantly differ from the background distribution. These differences mainly reflect the different meteorological conditions (i.e. moisture supply and convective stability). Although aerosol also influences CTT ("Albrecht effect", section 3.4), from this kind of analysis the

differences in the CTT distribution cannot be interpreted as a result of the aerosol influence.
In Fig. 19 corresponding histograms of liquid phase cloud effective radius are shown. It is obvious that for the classes "moderate" (black) and "high" (blue) total aerosol the effective radius distributions are concentrated around smaller values. Both distributions significantly deviate from the background (at 95%).
This is not only indicated by the much lower mean values of the samples (14.0±0.3µm and 12.7±0.3µm compared to 15.8±0.3µm for the backgorund sample), but also by the lower variance and much higher positive skewness. Especially the latter can be taken as a statistical description of the strongly reduced presence of large effective radii.

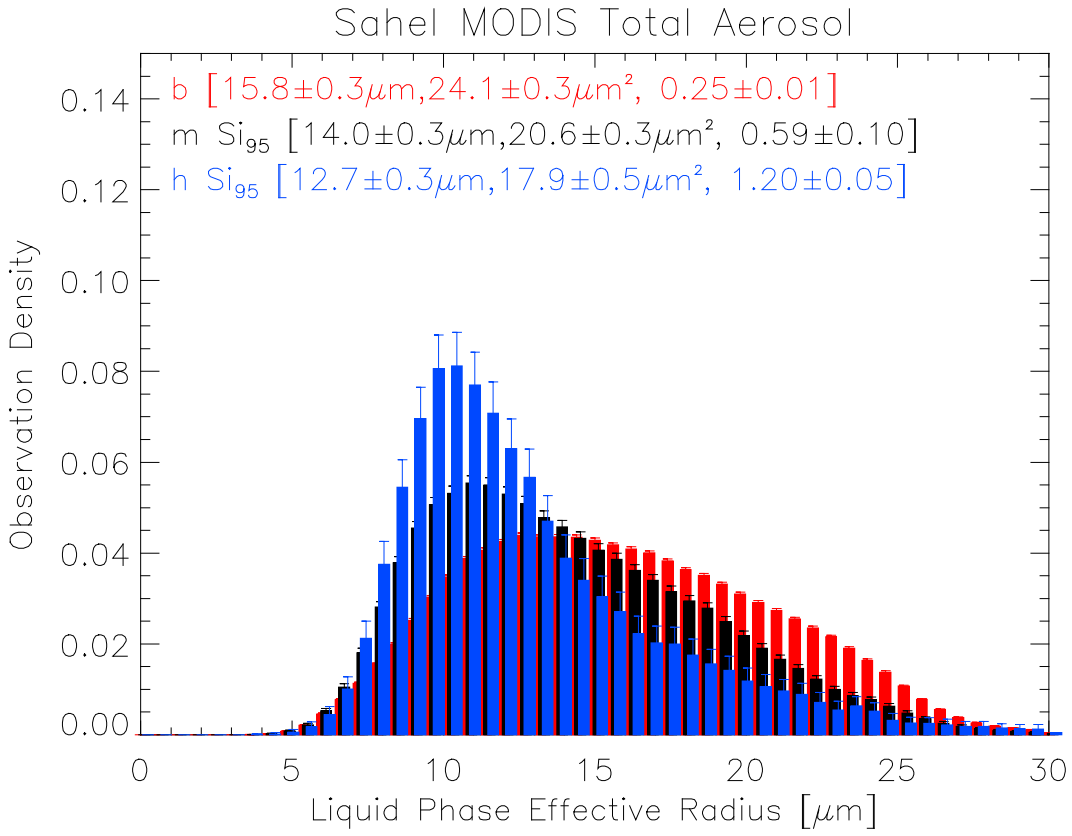

Fig. 19: Liquid cloud effective radius histograms for background (red), moderate (black) and high (blue) total aerosol in the Sahel observed by MODIS.

For the analysis of microphysial effects of aerosol on clouds, deviations in the CTT distributions have to be corrected in order to assess differences in microphysical cloud properties at similar CTT distributions (representing similar states of convection). Fig. 20 shows the variation of liquid cloud effective radius with cloud top temperature in the Sahel for total aerosol and the three subsets "background" (red), "moderate" (black) and "high" (blue). Solid lines represent the median effective radius value for the respective CTT bins, while the bars indicate the spread of the 20% and 80% quantiles of the respective distributions of effective radius. It is evident from Fig. 20 that liquid cloud effective radius is reduced under the influence of aerosols for most cloud top temperatures. The diamond symbols indicate that for the respective CTT bin the effective radius distribution deviates significantly (at 95%) from the respective background distribution. The profile behaviour seen in Fig. 20 also

matches very well the observations of effective radius profiles analysed e.g. by *Rudich et al.* (2003): Effective radius is strongly reduced (even below the 20%-quantile of the background conditions) in "polluted" clouds and converges to the background for low CTT (which represent deep convection and cirrus).
Unfortunately the MODIS Level 3 products do not provide seperate cloud top temperature for the liquid and the ice phase fraction of the clouds (which is done for most other cloud properties like effective radius, optical depth, cloud water path, cloud cover). Consequently liquid phase effective radius is also available at box-mean CTT lower than 240K, which obviously is not the temperature of the liquid water fraction. Nevertheless also total cloud CTT is suited for determining the convective height of the cloud ensemble observed within the grid box and thus representing the convective conditions of the box, but of course also introduces additional uncertainty to the analysis.

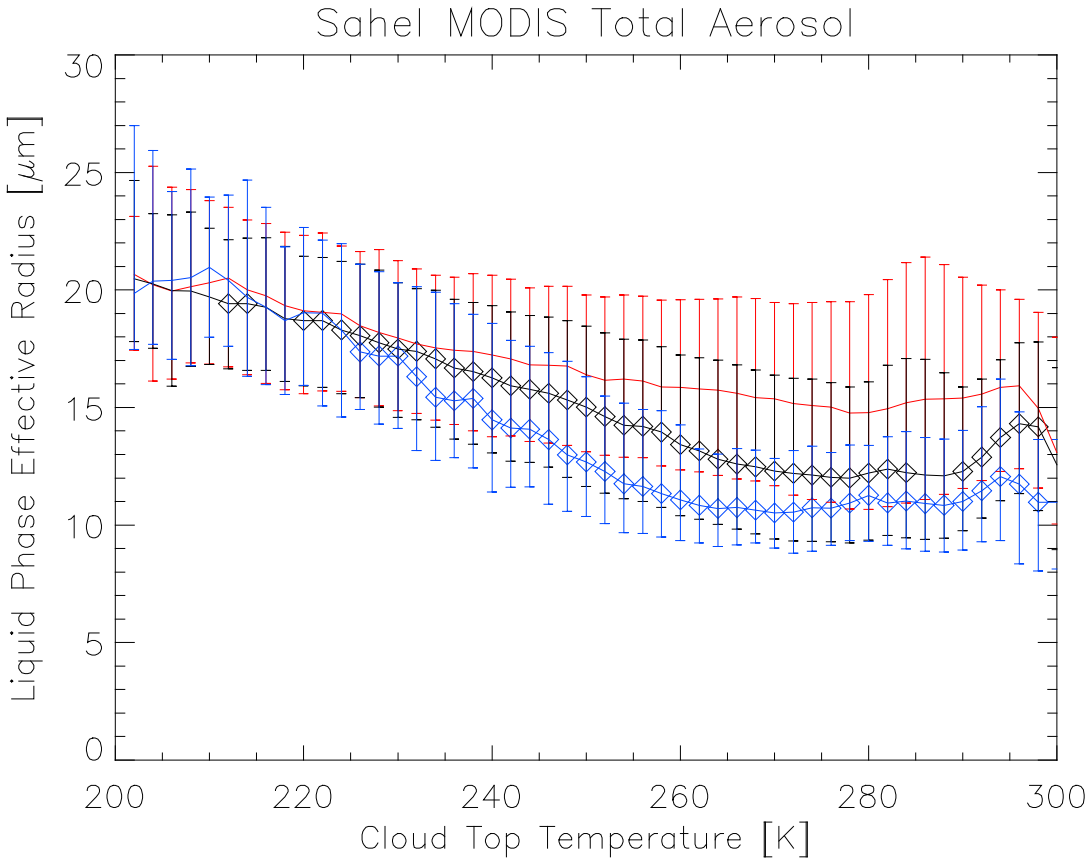

Fig. 20: Liquid phase effective radius as a function of cloud top temperature of Sahelian liquid water clouds and background (red), moderate (black) and high (blue) total aerosol. Solid lines indicate median, while bars represent the 20% and 80% quantile of the respective distributions.

The effective radius profiles (Fig. 20) are themselves effective radius distributions for each CTT bin. The result of this analysis is a two-dimensional 50x50 normalised propability matrix estimate $\mathbf{P}_{CTT,Re}$ which gives the common observation density of a pair of cloud top temperature and effective radius.
With the probability matrix **P** and the effective radius histograms $\mathbf{H}_b$, $\mathbf{H}_m$, $\mathbf{H}_h$ for the aerosol load classes "background", "moderate" and "high", respectively, now the observed effective radius histograms for the aerosol load classes can be projected

onto background CTT conditions. This is spelled out here for the projected histogram $\hat{\mathbf{H}}_m$ (for moderate aerosol) calculated as

$$\hat{H}(R_e)_m = \sum_{CTT}\left[\frac{P(CTT,R_e)\cdot H(CTT)_m}{H(CTT)_b}\right] \tag{46}$$

and analogous for the “high” aerosol load classes. The projected histogram $\hat{\mathbf{H}}_m$ now represents the background to test against, statistically accounting and correcting for differences in meteorological conditions for the different samples.

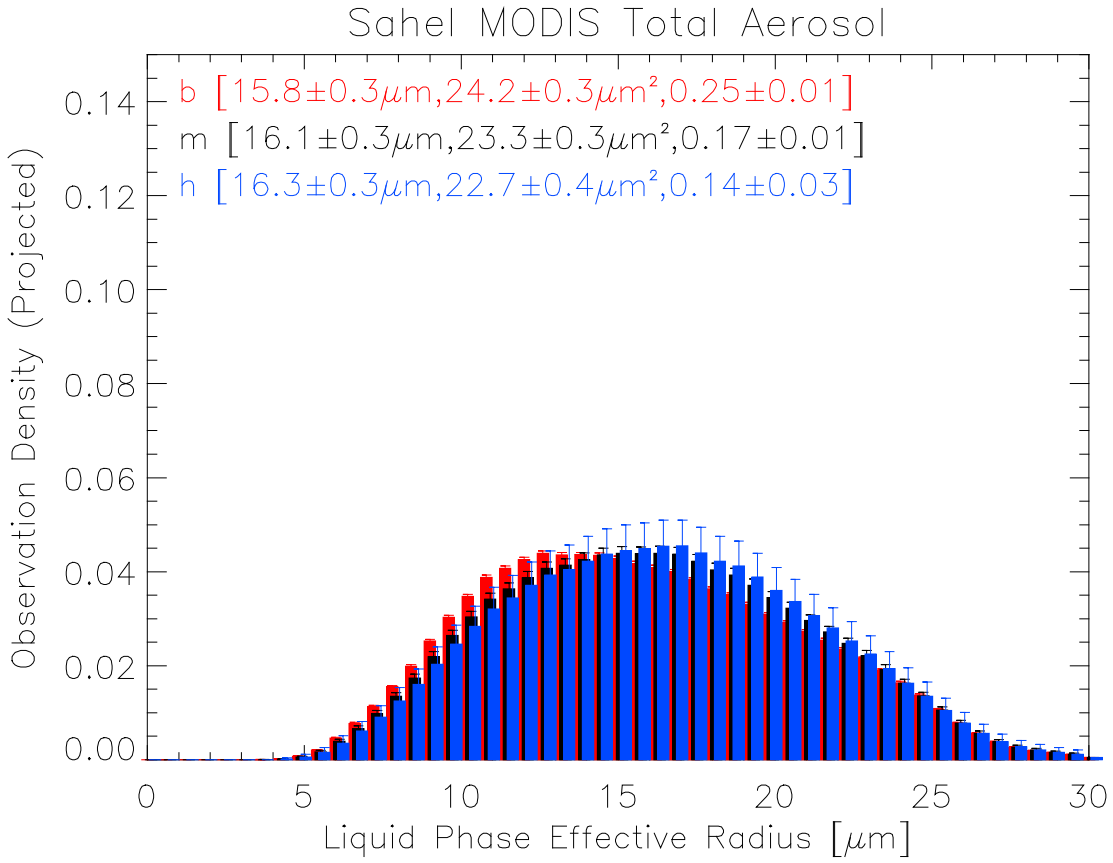

Fig. 21: Liquid cloud effective radius histograms projected on background CTT conditions using eq. (46) for total aerosol in the Sahel.

The projected histograms of liquid cloud effective radius observed by MODIS are presented in Fig. 21 for total aerosol in the Sahel.
Despite the significant deviations in cloud top temperature distribution of the three samples, the projected effective radius histograms do not differ significantly (Wilcoxon-Mann-Whitney test). The mean values for the "moderate" and "high" total aerosol classes are higher than for the background, as could be expected from the higher fraction of low cloud top temperature in these samples. The deviation of the observed effective radius histogram from the CTT-corrected background now indicates the relationship between aerosol and effective radius. This observavtion density difference is calculated as

$$\Delta \boldsymbol{H} = \boldsymbol{H}_m - \hat{\boldsymbol{H}}_m \quad (47)$$

and the example for liquid cloud effective radius in the Sahel is presented in Fig. 22. The background deviation is zero, indicating that the correction worked properly.

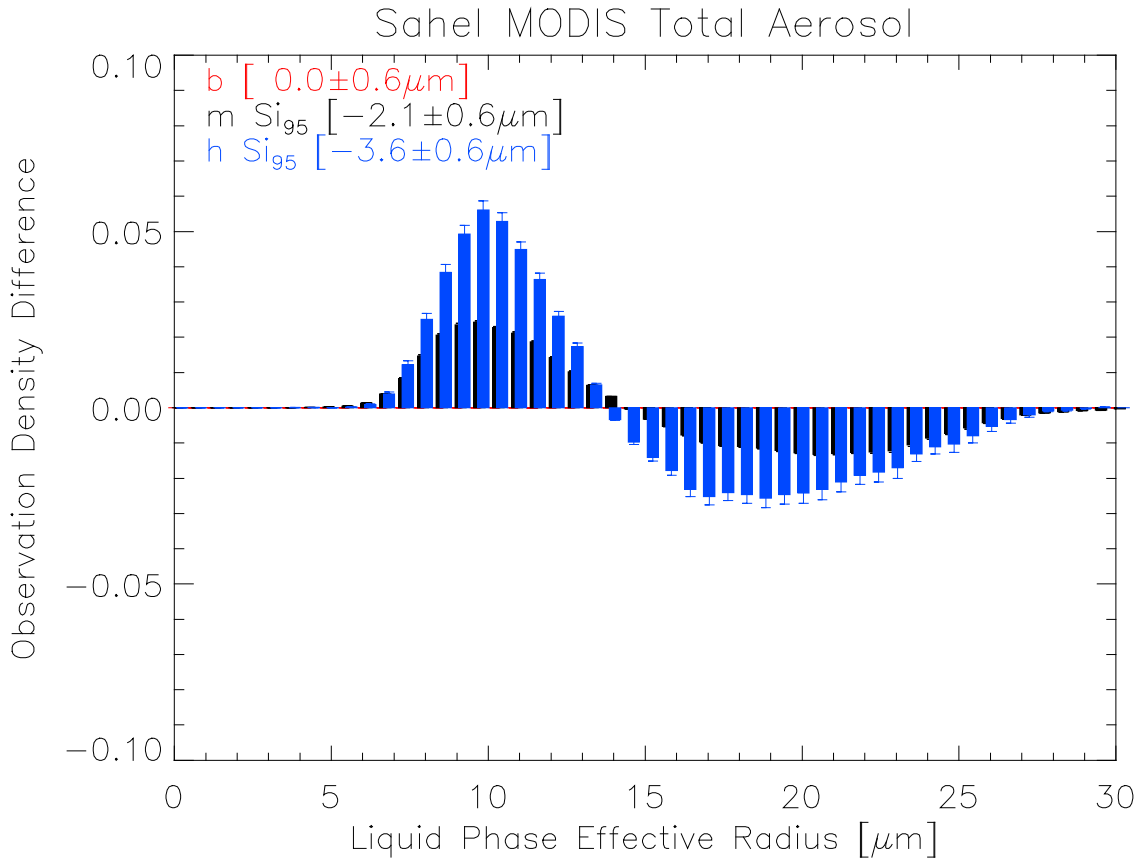

Fig. 22: Deviation between observed and projected liquid cloud effective radius in the Sahel for background (red, all zero as can be expected), moderate (black) and high (blue) total aerosol observed form MODIS.

For deviations to be accepted as statistically significant, three conditions have to be fulfilled. Firstly the observed uncorrected histograms have to deviate significantly (at 95%) from the background observations. Seconly the observed histogram has to differ significantly (at 95%) from the corrected background $\hat{H}$. The significant deviation is indicated by the "Si_{95}" tags in Fig. 22 for moderate and high aerosol classes. The third condition is that the mean deviation has to be higher than the statistical uncertainty resulting from the uncertainty estimation in both observed and projected histograms. Also this condition is fulfilled for moderate and high total aerosol in the case of liquid cloud effective radius in Fig. 22. Consequently these deviations from background conditions are statistically significant at the 95% confidence level.

This analysis method, presented exemplarily with the case of MODIS liquid cloud effective radius for total aerosol in the Sahel, is performed for all other cloud properties, aerosol classes and sensors in the same way.

Moreover, the CTT correction method enables to seperate aerosol effects on clouds from the other direction of influence, i.e. that given cloud conditions are responsible for aerosol emission (e.g. dust storms caused by convective density currents, e.g.

Miller et al., 2008; *Knippertz et al.*, 2010). In such cases the convective cloud development should follow the undisturbed background distribution profile with respect to CTT and no significant deviation should be present in the aerosol case. Nevertheless, once suspended into the atmosphere, the aerosol of course may also affect the cloud microphysics of the convective system which is responsible for its emission.
The presented analysis method is capable of detecting and quantifying from large scale (in both, space and time) statistical analysis mainly four relationships between aerosol and cloud microphysics:

1) *Droplet size reduction*
2) *Increasing cloud optical depth for elevated aerosol levels*
3) *Cloud lifetime effects represented by combined increases or decreases of cloud water path and cloud cover*
4) *Impacts on cloud phase (early vs. late freezing)*

For these four aerosol-cloud interactions the nullhypothesis to be tested is that they are not statistically relevant for cloud development (i.e. the cloud property samples). The nullhypothesis is rejected only if observation sample deviations from the background population are statistically significant at the 95% confidence level.
Other effects like the microphysical-radiative equilibrium (*Kaufman and Fraser*, 1997; *Koren et al.*, 2008; *Small et al.*, 2011) or consequences on precipitation (*Rosenfeld*, 2001; *Rudich et al.*, 2003; *Jenkins et al.*, 2008) may be included in the data, but from the available satellite data alone it is not possible to proof the respective effects from the potential evidence. The same is true for any potential cloud initialisation as a result of absorbing aerosols (e.g. *Rudich et al.*, 2003).
IASI data are available from descending (daylight overpasses in the local morning) and ascending (night time overpasses in the local evening) orbits. Analysis is performed for both orbits seperately in order to avoid spurious correlations due to the diurnal cycles of airborbe dust (e.g. *Schepanski et al.*, 2007) and convection.

8 Results

8.1 Droplet size

Analysis of liquid phase cloud effective radius is only possible from the MODIS data as the ENVISAT-APOLLO dataset does not provide effective radius and from IASI ice cloud properties only are retrieved. Tab. 6 shows the differences of MODIS derived liquid cloud effective radius to background conditions for all aerosol subsets and regions. The values in brackets below the region name provide the respective background mean effective radius of the region for comparison purposes. Reduced liquid phase effective radius is observed for all three aerosol subsets and for the regions Sahel, Maghreb and Arabia. In all of those the cloud effective radius decreases stronger for the high aerosol subset then for moderate aerosol. Only in Southern Africa an increase in cloud effective radius is observed for all aerosol subsets.

Tab. 6: Liquid phase cloud effective radius deviations from background conditions as observed by MODIS. Differences marked by * are not statistically significant at 95% confidence level.

region (region mean)	**Sahel** (15.8±0.3 µm)	**South-Africa** (12.3±0.3 µm)	**Arabia** (17.8±0.3 µm)	**Maghreb** (17.5±0.3 µm)
moderate total	-2.1±0.6 µm	+0.3±0.6 µm*	-2.0±0.6 µm	-2.7±0.6 µm
high total	-3.6±0.6 µm	+0.3±0.6 µm*	-4.2±0.6 µm	-4.9±0.6 µm
moderate dust	-1.7±0.6 µm	+0.4±0.6 µm*	-1.0±0.6 µm	-1.7±0.6 µm
high dust	-3.8±0.6 µm	+0.4±0.6 µm*	-3.3±0.6 µm	-3.7±0.6 µm
moderate fine	-2.4±0.6 µm	+0.2±0.6µm*	-3.0±0.6 µm	-4.2±0.6 µm
high fine	-3.4±0.6 µm	+0.1±0.6 µm*	-4.6±0.6 µm	-5.8±0.6 µm

In the Sahel, the Maghreb and Arabia the liquid water cloud effective radius reduction is more effective for the fine mode aerosol class than for the mineral dust class. Moreover in those regions all differences between aerosol classes and background are statistically significant at the 95% confidence level. The strongest effective radius decrease is observed for high fine mode aerosol in the Maghreb region (-5.8±0.6µm), while the weakest observed decrease is that for moderate dust in Arabia (-1.0±0.6µm). For the regions Sahel, Arabia and Maghreb the variability of effective radius reduction is stronger between aerosol classes than between regions.
The observed effective radius increase in Southern Africa is not statistically significant in any case.

Tab. 7: Ice phase cloud effective radius deviations from background conditions as observed by MODIS. Differences marked by * are not statistically significant at 95% confidence level.

region (region mean)	**Sahel** (23.8±0.8 µm)	**South-Africa** (18.3±0.8 µm)	**Arabia** (26.7±0.8 µm)	**Maghreb** (26.0±0.8 µm)
moderate total	-2.5±1.6 µm	+1.0±1.6 µm*	-1.8±1.6 µm	-3.1±1.6 µm
high total	-4.1±1.6 µm	+2.1±1.6 µm	-5.4±1.6 µm	-5.2±1.6 µm
moderate dust	-1.1±1.6 µm*	+1.4±1.6 µm*	-1.6±1.6 µm*	-2.0±1.6 µm
high dust	-2.6±1.6 µm	+2.3±1.6 µm	-4.8±1.6 µm	-2.8±1.6 µm
moderate fine	-3.3±1.6 µm	+0.6±1.6 µm*	-2.2±1.6 µm	-5.4±1.6 µm
high fine	-4.2±1.6 µm	+1.1±1.6 µm*	-6.1±1.6 µm	-6.4±1.6 µm

For ice cloud effective radius very similar results are obtained from MODIS. These are presented in tab. 7. As for liquid water clouds ice cloud effective radius is increased for all aerosol classes in Southern Africa and is decreased elsewhere. The increase is statistically significant only for high dust and total aerosol; generally all ice effective radius increases are relatively stronger than those for liquid water clouds.
In contrast to the liquid water cloud effective radius analysis for ice clouds also the effect of moderate dust is not statistically significant (at the 95% level) in the Sahel and in Arabia. Mean values of the ice cloud effective radius distributions are generally higher than for liquid water. Thus, the relative changes of ice cloud effective radius are smaller than for liquid water effective radius in the Sahel, Arabia and the Maghreb.
Ice cloud effective radius is also retrieved from IASI observations.The resulting deviations of moderate and high dust from background are presented in Tab. 8 for daytime (descending) and night time (ascending) Metop overpasses.

Tab. 8: Ice cloud effective radius deviations from background conditions as observed by IASI for moderate and high dust and decsending and ascending overpasses. Respective background means are also given in brackets. Differences marked by * are not statistically significant at 95% confidence level.

Region	**Sahel**	**South-Africa**	**Arabia**	**Maghreb**
moderate dust (descending**)**	+2.0±1.0 µm (27.1±0.5 µm)	+1.8±1.0 µm (27.9±0.5 µm)	+3.0±1.0 µm (26.7±0.5 µm)	+1.6±1.0 µm (26.8±0.5 µm)
high dust (descending**)**	+3.9±1.0 µm (27.1±0.5 µm)	+3.4±1.0 µm (27.9±0.5 µm)	+5.0±1.0 µm (26.7±0.5 µm)	+4.0±1.0 µm (26.8±0.5 µm)
moderate dust (ascending**)**	+2.2±1.0 µm (26.9±0.5 µm)	+3.1±1.0 µm (26.8±0.5 µm)	+2.8±1.0 µm (26.2±0.5 µm)	+2.1±1.0 µm (25.6±0.5 µm)
high dust (ascending**)**	+4.0±1.0 µm (26.9±0.5 µm)	+6.2±1.0 µm (26.8±0.5 µm)	+4.7±1.0 µm (26.2±0.5 µm)	+4.8±1.0 µm (25.6±0.5 µm)

Unlike from MODIS observations, effective radius as retrieved from IASI observations is increased with respect to background conditions for all regions. The increase in effective radius is generally highest in Arabia. Here the effects observed at descending orbits, i.e. morning overpasses, are stronger than those of the ascending orbits (evening overpasses), but within the uncertainty range. For the three other regions the order is inverted, stronger ice cloud effective radius increases are observed in the evening. In Arabia and the Maghreb mean effective radius from IASI descending orbits fits well the MODIS observations, which is not the case in the two other regions.

8.2 Cloud optical depth

Cloud optical depth is analysed in the same way and independently from the effective radius results. Three optical depth subsets are analysed subsequently: liquid water cloud optical depth (MODIS only), ice cloud optical depth (including IASI data) and total cloud optical depth (including ENVISAT data).
MODIS results of liquid water cloud optical depth deviations from background conditions are provided in tab. 9 for all three aerosol type classes. Deviation results not statistically significant at the 95% level are marked again with the * symbol.

Tab. 9: Liquid phase cloud optical depth deviations from background conditions as observed by MODIS. Differences marked by * are not statistically significant at 95% confidence level.

region (region mean)	**Sahel** (9.4±0.5)	**South-Africa** (5.8±0.5)	**Arabia** (7.7±0.5)	**Maghreb** (7.0±0.5)
moderate total	+0.2±1.0*	-0.0±1.0*	+0.8±1.0*	+1.4±1.0
high total	+0.4±1.0*	-0.1±1.0*	+5.0±1.0	+5.2±1.0
moderate dust	-1.1±1.0	-0.5±1.0*	+1.0±1.0*	+1.0±1.0*
high dust	-1.5±1.0	-0.5±1.0*	+4.8±1.0	+2.3±1.0
moderate fine	+0.9±1.0*	+0.3±1.0*	+0.8±1.0*	+2.3±1.0
high fine	+0.8±1.0*	+1.2±1.0	+5.7±1.0	+6.5±1.0

It is evident that much more deviation results are not statistically significant (at 95%) given the significance criteria applied here then it is the case for effective radius observations. Optical depth is generally increased with MODIS aerosol load compared to background conditions, only in the Sahel under dusty conditions liquid water cloud optical depth is decreased. In Southern Africa for dust insignificant optical depth reduction is observed, for total aerosol the liquid phase optical depth is not changed at all. Given the relatively high mean background optical depth in the Sahel (9.4±0.5), the relative deviations from background for the total and fine mode high aerosol classes are rather small compared to the Arabia and Maghreb regions. Interestingly for fine mode aerosol in the Sahel the deviation from background is larger for the moderate aerosol class than for high aerosol conditions (both within the uncertainty range).

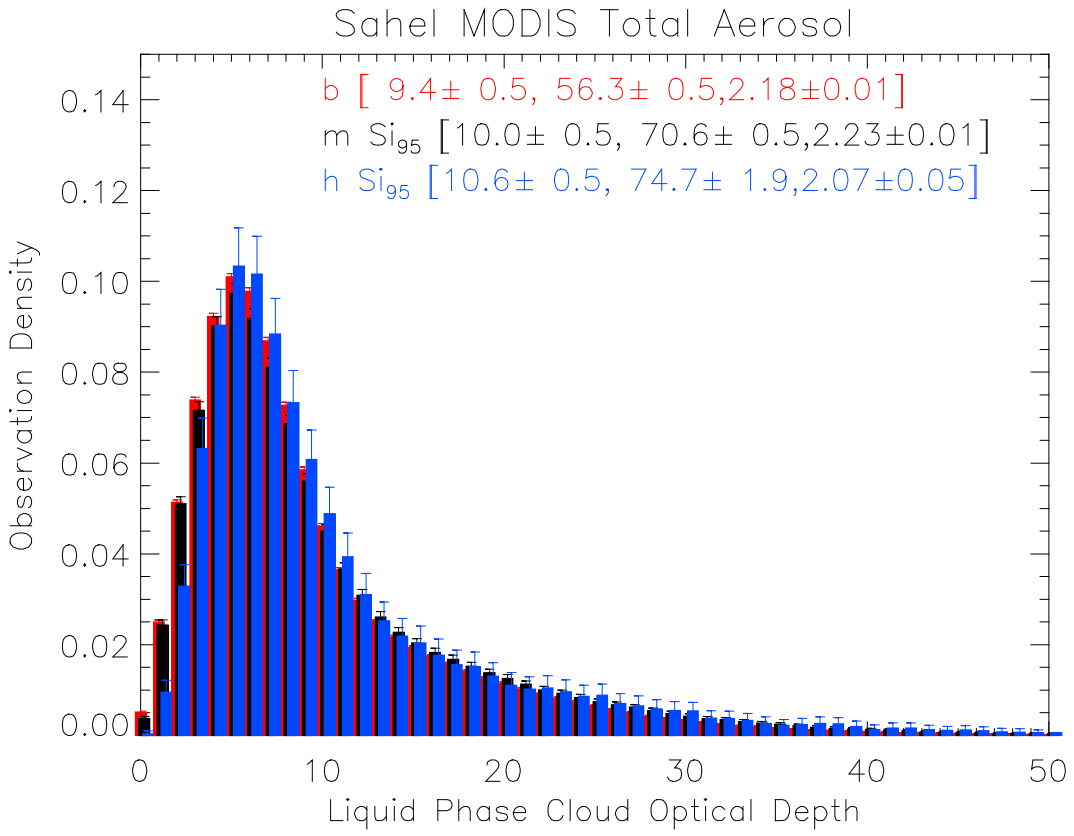

Fig. 23: Liquid water cloud optical depth histograms for background (red), moderate (black) and high (blue) total aerosol in the Sahel observed by MODIS.

Fig. 23 presents the liquid water cloud optical depth histograms obtained from MODIS observations in the Sahel for background, moderate and high total aerosol, respectively. The distributions of the moderate and high aerosol class deviate significantly (at 95%) from the background distribution. They show higher mean values and also higher variance as well as strongly reduced skewness. For comparison, Fig. 24 shows the same kind of histograms for the Maghreb region.
It is obvious that differences between moderate respective high total aerosol conditions and the background, although being significant also in the Sahel, are much stronger in the Maghreb. Moreover the influence of CTT projection on the resulting optical depth deviations can be seen in this example: without CTT projection the deviation of the moderate and high aerosol classes would be 1.7±1.0 and 5.7±1.0 instead of 1.4±1.0 and 5.2±1.0, respectively.

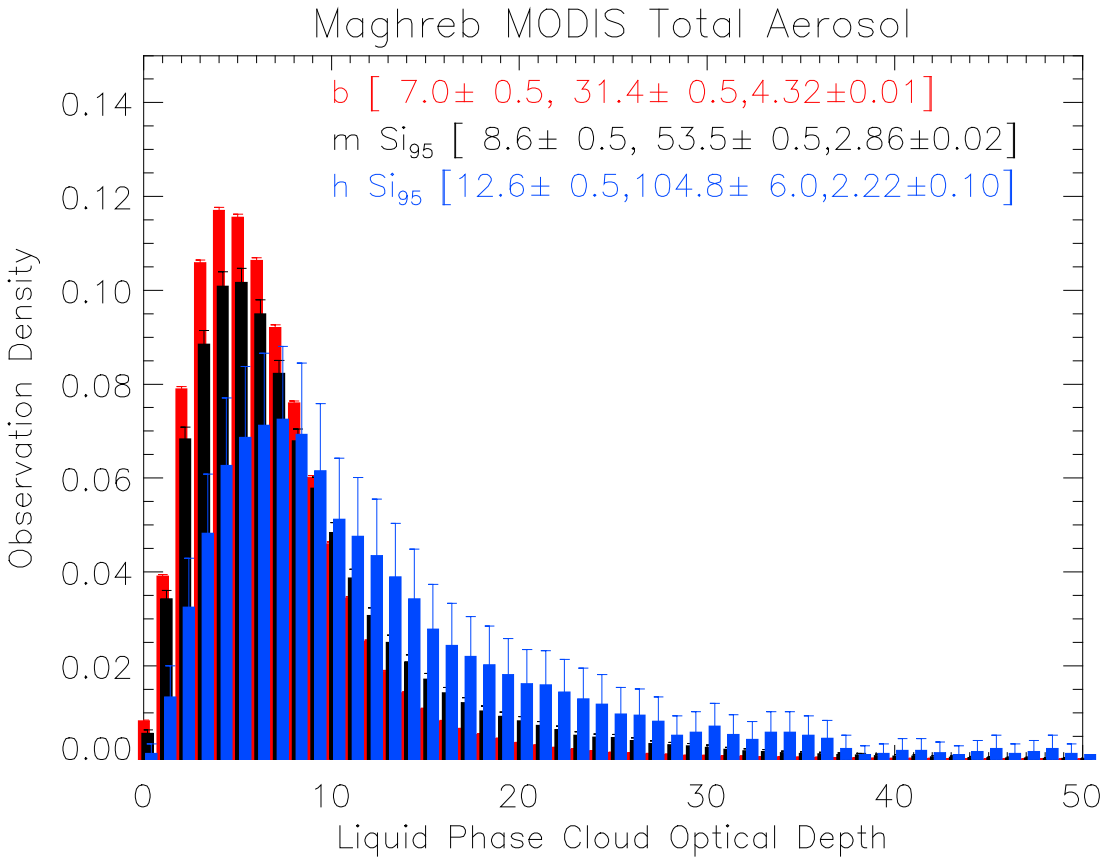

Fig. 24: Liquid water cloud optical depth histograms for background (red), moderate (black) and high (blue) total aerosol in the Sahel observed by MODIS.

Tab. 10 presents the results for ice cloud optical depth from MODIS. Negative deviations from background condition are again observed in the Sahel, in the case of ice clouds also for the high total and fine mode aerosol classes. In the other regions ice cloud optical depth is increased compared to background conditions for all aerosol classes. Deviations are not statistically significant at 95% for moderate aerosol (all types) in Southern Africa and Arabia and also not for moderate fine mode aerosol in Southern Africa. In Southern Africa generally very low mean ice cloud optical depth is observed, while in the Sahel mean optical depth is higher for ice than

for liquid water clouds (compare to Tab. 9). For high fine mode aerosol in Arabia and the Maghreb positive ice cloud optical depth increase of more than 100% of background mean value is observed, which is also reflected in the high total aerosol analysis. The corresponding ice cloud optical depth analysis from IASI observations for moderate and high dust at descending and ascending overpasses is summarized in Tab. 11.

Tab. 10: Ice cloud optical depth deviations from background conditions as observed by MODIS. Differences marked by * are not statistically significant at 95% confidence level.

region (region mean)	**Sahel** (12.5±0.8)	**South-Africa** (4.7±0.8)	**Arabia** (7.9±0.8)	**Maghreb** (7.3±0.8)
moderate total	+0.1±1.6*	+1.4±1.6*	+1.7±1.6	+3.3±1.5
high total	-2.2±1.6	+2.8±1.6	+7.7±1.6	+9.2±1.6
moderate dust	-3.4±1.6	+1.2±1.6*	+1.3±1.6*	+2.1±1.6
high dust	-3.9±1.6	+2.6±1.6	+8.7±2.1	+4.2±1.6
moderate fine	+1.8±1.6	+1.5±1.6*	+2.3±1.6	+5.7±1.6
high fine	-2.3±1.6	+3.5±1.6	+9.3±1.6	+11.4±1.6

Tab. 11: Ice cloud optical depth deviations from background conditions as observed by IASI for moderate and high dust and decsending and ascending overpasses. Respective background means are also given in brackets. Differences marked by * are not statistically significant at 95% confidence level.

region	**Sahel**	**South-Africa**	**Arabia**	**Maghreb**
moderate dust (descending)	+0.7±0.2 (2.6±0.1)	+0.5±0.2 (2.3±0.1)	+0.5±0.2 (1.5±0.1)	+0.3±0.2 (1.5±0.1)
high dust (descending)	+1.3±0.2 (2.6±0.1)	+0.5±0.2 (2.3±0.1)	+1.1±0.2 (1.5±0.1)	+0.7±0.2 (1.5±0.1)
moderate dust (ascending)	+0.8±0.2 (2.2±0.1)	+0.5±0.2 (1.9±0.1)	+0.3±0.2 (1.4±0.1)	+0.1±0.2* (1.3±0.1)
high dust (ascending)	+0.7±0.2 (2.2±0.1)	+0.0±0.2* (1.9±0.1)	+0.6±0.2 (1.4±0.1)	+0.3±0.2 (1.3±0.1)

Ice cloud optical depth observed by IASI is increased in all cases but one, where no change of mean ice cloud optical depth is observed (strong dust at ascending orbits in Southern Africa). In most cases the mean optical depth changes are weaker from IASI than from MODIS, but as IASI optical depths saturate at values of about 10, also mean values are much lower than those of MODIS. The strongest increases of ice cloud optical depth are observed in the Sahel and in Arabia for strong dust during morning overpasses (descending orbits). For high dust in ascending orbits in Southern Africa the net-effect is zero and consequently insignificant, but nevertheless the observation density distribution is much narrower than the background and strongly peaked around the mean value.

Total optical depth is determined from MODIS and ENVISAT, MODIS results are presented in tab. 12 while the ENVISAT results are provided in tab. 13.

MODIS total cloud optical depth deviations from background conditions reflect the combination of the described above liquid and ice cloud optical depth results. As above, total cloud optical depth is decreased in the Sahel for both dust and the high total aerosol classes and is increased elsewhere.

Tab. 12: Total cloud optical depth deviations from background conditions as observed by MODIS. Differences marked by * are not statistically significant at 95% confidence level.

region (region mean)	**Sahel** (9.8±0.5)	**South-Africa** (5.8±0.5)	**Arabia** (7.7±0.5)	**Maghreb** (7.0±0.5)
moderate total	+0.1±1.0*	+0.5±1.0*	+1.0±1.0*	+1.9±1.0*
high total	-0.7±1.0*	+1.1±1.0	+5.5±1.0	+6.5±1.0
moderate dust	-1.5±1.0	+0.1±1.0*	+1.2±1.0	+1.4±1.0
high dust	-2.3±1.0	+0.7±1.0*	+6.6±1.0	+2.7±1.0
moderate fine	+0.9±1.0*	+0.8±1.0*	+0.9±1.0*	+3.0±1.0
high fine	-0.5±1.0*	+2.5±1.0	+6.2±1.0	+8.3±1.0

ENVISAT sample sizes are much smaller than for MODIS, partly due to the large pixel sizes of SCIAMACHY, its alternating view modes together with much smaller swath of AATSR and partly due to the fact that the SYNAER aerosol retrieval does not work over bright surfaces. The small sample sizes of the ENVISAT data sets are reflected in the very high uncertainties and in the fact that due to these uncertainties none of the observed optical depth deviations from background is statistically significant at 95%. Moreover for high aerosol of all three types as well as for moderate dust in Southern Africa sample sizes are too small to perform any statistical analysis at all, the same for high dust in the Sahel. The Arabia region is missing in tab. 13 because no SYNAER and APOLLO observations have been processed for this easternmost region so far. Since the region is dominated by very bright soils, only few SYNAER observations would be available at all.
Nevertheless despite the lack of statistical significance it can be seen that most total cloud optical depth deviations from background conditions observed by ENVISAT are positive, the only negative values are in the Maghreb for high total and moderate dust aerosol, for high fine mode aerosol in the Maghreb no deviation at all is detected (with very high uncertainty).

Tab. 13: Total cloud optical depth deviations from background conditions as observed by ENVISAT. Differences marked by * are not statistically significant at 95% confidence level.

region (region mean)	**Sahel** (9.3±0.6)	**South-Africa** (8.6±1.3)	**Arabia** (--)	**Maghreb** (7.6±0.5)
moderate total	+0.8±1.0*	+1.6±5.6*	--	+1.3±1.6*
high total	+1.5±2.3*	--	--	-1.0±2.6*
moderate dust	+0.7±5.3*	--	--	+2.8±4.3*
high dust	--	--	--	-1.5±3.6*
moderate fine	+0.8±1.0*	+1.1±6.0*	--	+1.4±1.7*
high fine	+2.3±2.5*	--	--	-0.1±2.8*

8.3 Cloud lifetime

Cloud lifetime cannot be determined directly from polar orbiting satellites. Thus the hypothesis of cloud lifetime increase can only be tested indirectly. Moreover, as cloud top temperature is used here to correct for different convection development state distributions of the samples, it can also not be used as observable for testing the extension of cloud lifetime. Nevertheless, cloud cover and cloud water path are well suited observables to test the consequences of a potential longer cloud lifetime. If the cloud lifetime effect as suggested in the literature is effective, cloud water path and

cloud cover will both increase, as cloud dissipation is slowed down. Liquid water path is analysed in tab. 14 from MODIS observations. In the Sahel, where background LWP mean is highest, LWP is reduced for all aerosol classes compared to the background significantly (at 95%).

Tab. 14: Liquid water path deviations from background conditions as observed by MODIS. Differences marked by * are not statistically significant at 95% confidence level.

region (region mean)	**Sahel** (92±5 g/m²)	**South-Africa** (45±5 g/m²)	**Arabia** (86±5 g/m²)	**Maghreb** (80±5 g/m²)
moderate total	-16±10 g/m²	+2±10 g/m² *	-7±10 g/m² *	-3±10 g/m² *
high total	-28±10 g/m²	+2±10 g/m²*	+8±10 g/m²	+12±10 g/m²
moderate dust	-23±10 g/m²	-1±10 g/m² *	+1±10 g/m²*	+0±10 g/m² *
high dust	-37±10 g/m²	-1±10 g/m² *	+18±10 g/m²	-5±10 g/m²*
moderate fine	-13±10 g/m²	+4±10 g/m² *	-15±10 g/m²	-5±10 g/m²
high fine	-26±10 g/m²	+12±10 g/m²	+11±10 g/m²	+16±10 g/m²

In Southern Africa only the increase for high fine mode aerosol is statistically significant at 95%. In Arabia the significant (at 95%) decrease of LWP observed in the moderate fine mode aerosol class is also reflected by an insignificant decrease at moderate total aerosol classes, while LWP is increased in all other aerosol classes. The increase for moderate dust is also insignificant. In the Maghreb LWP deviations are insignificant for mineral dust, while LWP is reduced for moderate fine mode (significantly) and total (insignificantly) aerosol and significantly increased for the respective high aerosol classes.

Tab. 15: Ice water path deviations from background conditions as observed by MODIS. Differences marked by * are not statistically significant at 95% confidence level.

region (region mean)	**Sahel** (156±5 g/m²)	**South-Africa** (43±5 g/m²)	**Arabia** (114±5 g/m²)	**Maghreb** (101±5 g/m²)
moderate total	-17±10 g/m²	+15±10 g/m²	+9±10 g/m² *	+19±10 g/m²
high total	-54±10 g/m²	+33±10 g/m²	+37±10 g/m²	+48±10 g/m²
moderate dust	-36±10 g/m²	+13±10 g/m²	+12±10 g/m²	+17±10 g/m²
high dust	-57±10 g/m²	+31±10 g/m²	+50±10 g/m²	+24±10 g/m²
moderate fine	-9±10 g/m² *	+16±10 g/m²	+4±10 g/m² *	+25±10 g/m²
high fine	-55±10 g/m²	+37±10 g/m²	+44±10 g/m²	+57±10 g/m²

Ice water path from MODIS, presented in tab. 15, shows in general the same characteristics as liquid water path, reduced IWP for all aerosol classes in the Sahel and increased IWP elsewhere. Only the IWP decrease for moderate fine mode aerosol in the Sahel and the increased IWP for moderate total and fine mode aerosol in Arabia are not statistically significant at the 95% level.
Ice water path is also retrieved from IASI optical depth and effective radius observations. Respective results for IWP changes in dusty conditions for both orbits are presented in tab. 16. As both, optical depth and effective radius is increased in all regions with respect to background conditions, consequently also IWP is increased. In the Arabia domain the IWP increases reaches up to 100% of background IWP for high dust loads. Relative to background IWP the increases are smallest in Southern Africa. Due to the opacity limit of the infrared optical depth retrieval maximum IWP observed by IASI is much smaller than for MODIS. Consequently also mean IWP is much smaller for IASI than for MODIS.

Tab. 16: Ice water path deviations from background conditions as observed by IASI for moderate and high dust and decsending and ascending overpasses. Respective background means are also given in brackets. Differences marked by * are not statistically significant at 95% confidence level.

region	Sahel	South-Africa	Arabia	Maghreb
moderate dust (descending)	+12±2g/m² (35±1g/m²)	+9±2g/m² (32±1g/m²)	+9±2g/m² (20±1g/m²)	+5±2g/m² (20±1g/m²)
High dust (descending)	+21±2 g/m² (35±1) g/m²	+9±2g/m² (32±1g/m²)	+20±2g/m² (20±1g/m²)	+13±2g/m² (20±1g/m²)
moderate dust (ascending)	+12±2g/m² (29±1g/m²)	+7±2g/m² (26±1g/m²)	+6±2g/m² (18±1g/m²)	+3±2 g/m² (17±1g/m²)
high dust (ascending)	+14±2g/m² (29±1g/m²)	+4±2g/m²* (26±1g/m²)	+13±2g/m² (18±1g/m²)	+7±2 g/m² (17±1g/m²)

In fig. 25 median total cloud cover is depicted as a function of cloud water path (CWP) from MODIS observations in the Southern African (Kalahari) region. For all three, background (red curve), moderate total aerosol (black curve) and high total aerosol (blue curve), cloud cover increases with CWP with the strongest increase for moderately low CWP in all three classes. Diamond symbols indicate that the respective cloud cover distributions for moderate and high total aerosol at given CWP deviate significantly from the background. This also is evident from the 20% and 80% quantiles. The cloud cover profile for moderate and high total aerosol deviates significantly from the background profile over the whole CWP range.

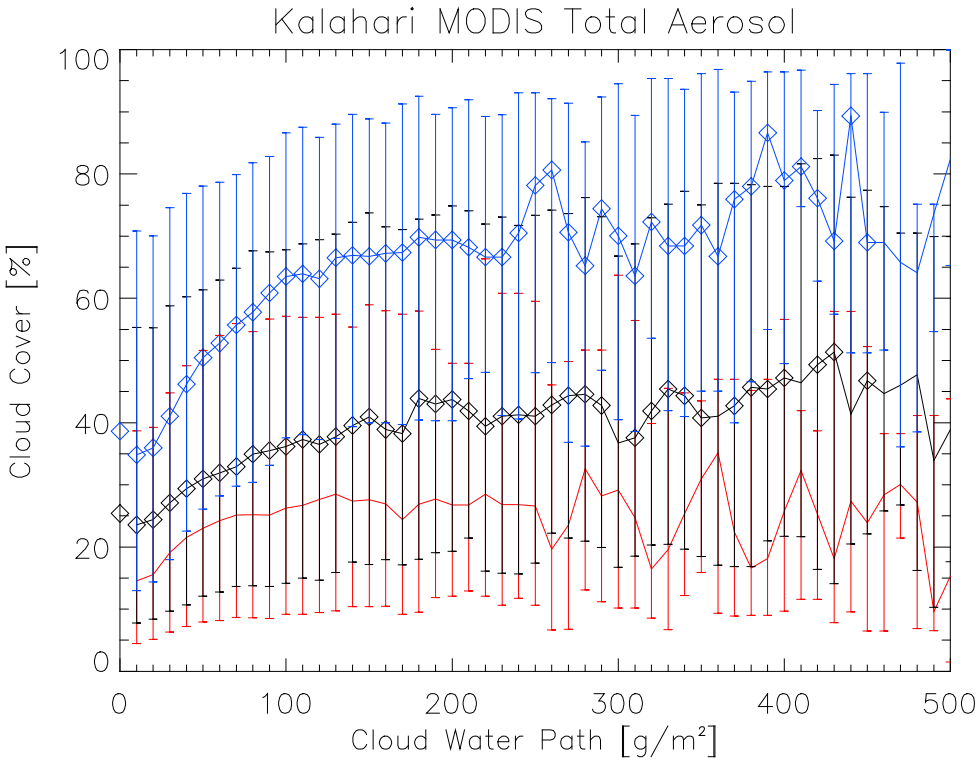

Fig. 25: Cloud cover as a function of cloud water path for background (red), moderate (black) and high (blue) total aerosol in the Kalahari region. Solid lines indicate median, while bars represent the 20% and 80% quantile of the respective distributions.

Tab. 17: Cloud cover deviations from background conditions as observed by MODIS. Differences marked by * are not statistically significant at 95% confidence level.

region (region mean)	**Sahel** (51±1 %)	**South-Africa** (12±1 %)	**Arabia** (48±1 %)	**Maghreb** (56±1 %)
moderate total	+4±2	+11±2	+8±2	+3±2
high total	+2±2*	+31±2	+13±2	+7±2
moderate dust	+3±2	+12±2	+11±2	+5±2
high dust	+11±2	+30±2	+6±2	+6±2
moderate fine	+2±2*	+10±2	+6±2	-1±2*
high fine	-3±2	+34±2	+10±2	+2±2*

Table 17 shows cloud cover deviations from MODIS. In most cases cloud cover is increased compared to background conditions. Only for high fine mode aerosol in the Sahel and moderate fine mode aerosol in the Maghreb cloud cover is reduced. The latter one is not significant at the 95% confidence level, as well as the cloud cover increases for high total and moderate fine mode aerosol in the Sahel. Regional mean cloud cover in Southern Africa is extremely low (12±1 %) compared to the three other regions (all around 50%). Nevertheless for Southern Africa highest absolute increases in cloud cover are observed. The extreme differences in cloud cover distributions for Southern Africa are presented in fig. 26.

.

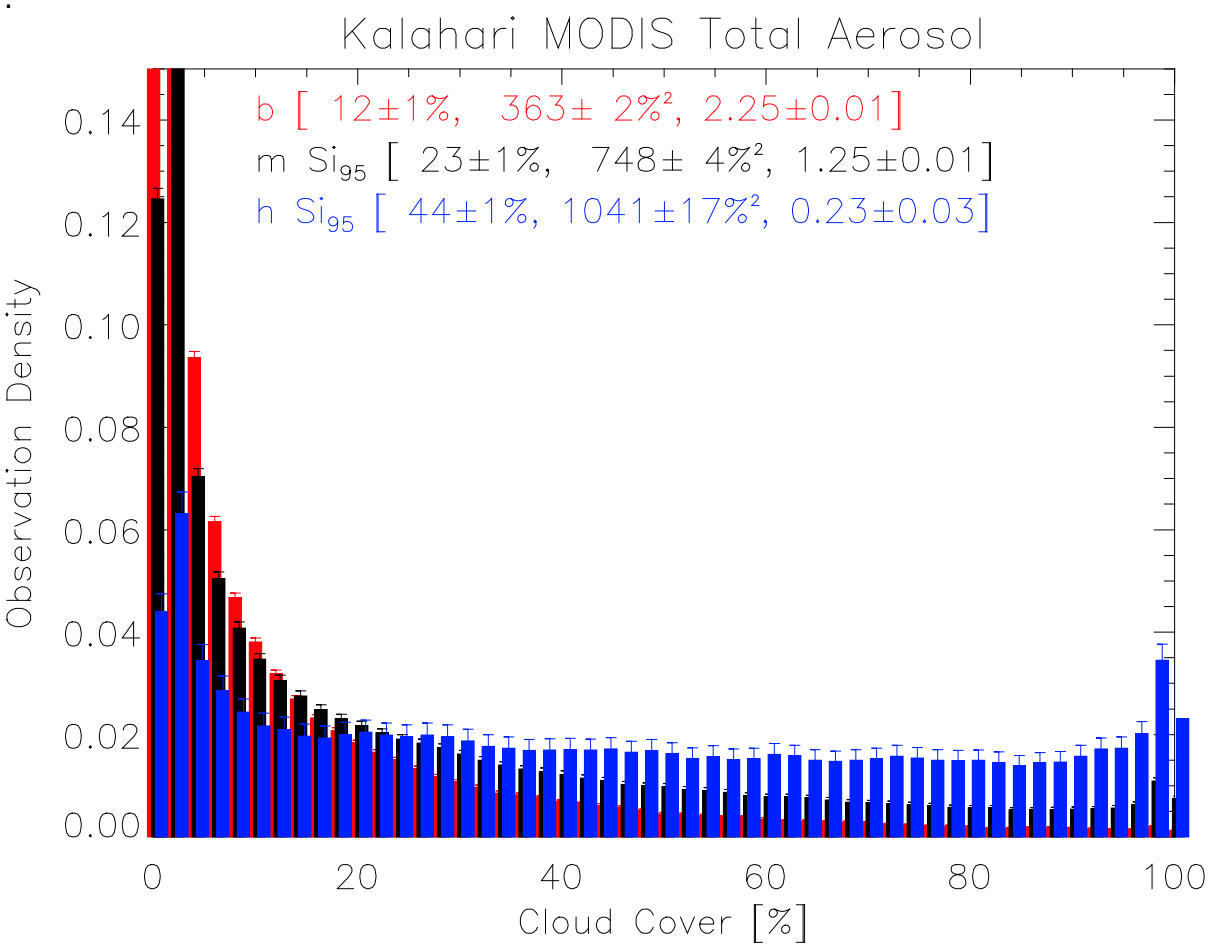

Fig. 26: Cloud cover histograms from MODIS for Southern Africa. The distributions for moderate ("m", black) and high ("h", blue) total aerosol deviate significantly (at 95%) from the background distribution ("b", red).

Corresponding results for cloud cover from ENVISAT are presented in tab. 18. Again the low sampling rate of the ENVISAT dataset causes high uncertainties. Moreover the SYNAER limitation to cloud cover below 50% over a large satellite pixel can be seen in the strongly reduced cloud cover values of the Sahel and the Maghreb compared to MODIS observations. Only in Southern Africa, where cloud cover is generally small, ENVISAT and MODIS mean cloud cover match within the error bars. Consequently none of the cloud cover deviation observations is statistically significant from ENVISAT. Cloud cover decrease (insignificant) is only observed for moderate total and fine mode aerosol in the Maghreb, while cloud cover is increased or unchanged elsewhere. For Arabia no ENVISAT observations are available.
From IASI no cloud cover is retrieved due to the lack of liquid phase cloud observations and the rather large footprints of the IASI observations (12km pixel diameter at nadir).

Tab. 18: Cloud cover deviations from background conditions as observed by ENVISAT. Differences marked by * are not statistically significant at 95% confidence level.

region (region mean)	**Sahel** (23±1 %)	**South-Africa** (13±2 %)	**Arabia** (--)	**Maghreb** (28±1 %)
moderate total	+1±2*	+0±6*	--	-2±3*
high total	+5±5*	--	--	+19±7*
moderate dust	+4±7*	+4±18*	--	+5±16*
high dust	+4±10*	--	--	+6±15*
moderate fine	+1±2*	+0±7*	--	-2±3*
high fine	+6±6*	--	--	+22±8*

9 Discussion

9.1 Relationships between aerosol and droplet size

Liquid cloud effective radius is reduced by all three aerosol types in all regions but Southern Africa. Fine mode aerosols include soot, sulfates and other water soluble aerosol particles and consequently are much more hygroscopic than mineral dust.
As a result of the stronger hygroscopicity the reducing effect is stronger for fine mode aerosol than for mineral dust in almost all cases. The fine mode detection by MODIS dark target retrievals seems to be rather robust (*Levy et al.*, 2010) in correctly identifying fine mode dominated aerosols. Nevertheless, such conclusion cannot be drawn for the "Deep Blue" aerosol type separation. Moreover, the dust (coarse mode) fraction detected by the MODIS "dark target" retrieval still includes a significant fraction of fine mode aerosols. Thus, although differences in effective radius reducing capability between fine mode aerosol and mineral dust are evident from tab. 6, it cannot be concluded that these differences fully represent different sensitivities to aerosol type. In the Southern African Kalahari domain slight but insignificant increases of effective radius are observed for all aerosol types. It is not clear if the positive sign is the result of uncertainties in the analysis given the different cloud states for the observations.

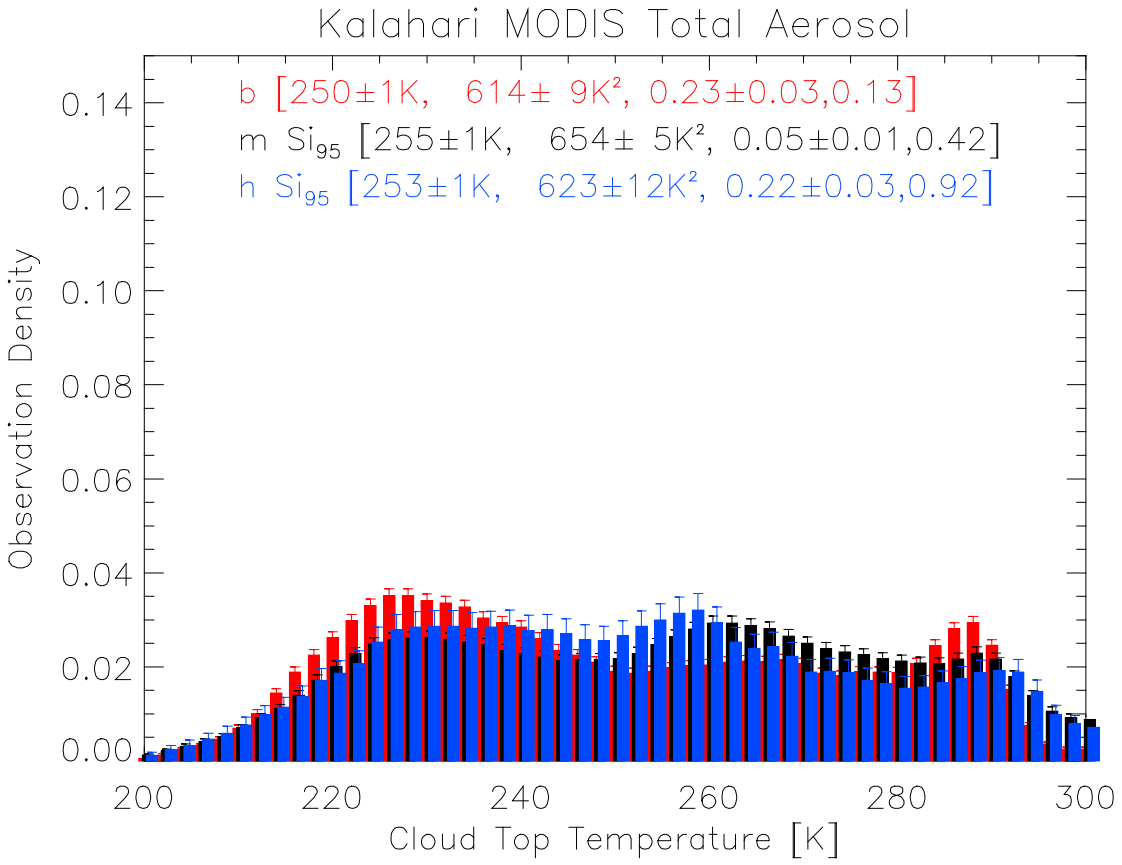

Fig. 27: Cloud top temperature histograms for background (red), moderate (black) and high (blue) total aerosol in the Southern African Kalahari region.

Regional mean cloud cover of pristine background is extremely low in Southern Africa, which also is reflected in very low mean liquid cloud effective radius (12.3±0.3 µm). Cloud cover is dramatically increased in the case of higher aerosol loads (fig. 26), which is also reflected in observations of higher mean effective radius for the moderate and high aerosol classes. The lack of attribution of different cloud top temperature values to the liquid, undetermined and ice cloud fractions in the aggregated MODIS observations also impacts on the analysis presented here. In most regions shallow liquid water clouds are the predominant feature in the CTT distributions (see e.g. Fig. 18 for Sahelian CTT). In the Southern African Kalahari region the shallow cloud peak is strongly reduced and the contribution of mid-level clouds (240K<CTT<260K, often mixed-phase) and deep convective systems dominates the CTT distribution (Fig. 27).
Rudich et al. (2003) analyse aerosol-cloud-interactions in events of extremely heavy fine mode aerosol contamination from the Kuwait oil fires in 1991. They find drastically reduced liquid phase effective radius for a wide range of cloud top temperatures. The same can be seen in the fine mode analysis for the Arabia region here (fig. 26).
Especially for higher cloud top temperatures the effective radius of polluted clouds is significantly lower than for pristine conditions. The diamond symbols indicate that the effective size distribution for the respective CTT bin deviates significantly (at the 95% confidence level) from the background distribution. For high fine mode aerosol at CTT>250 the median effective radius is even lower than the 20% quantile of the background distribution.

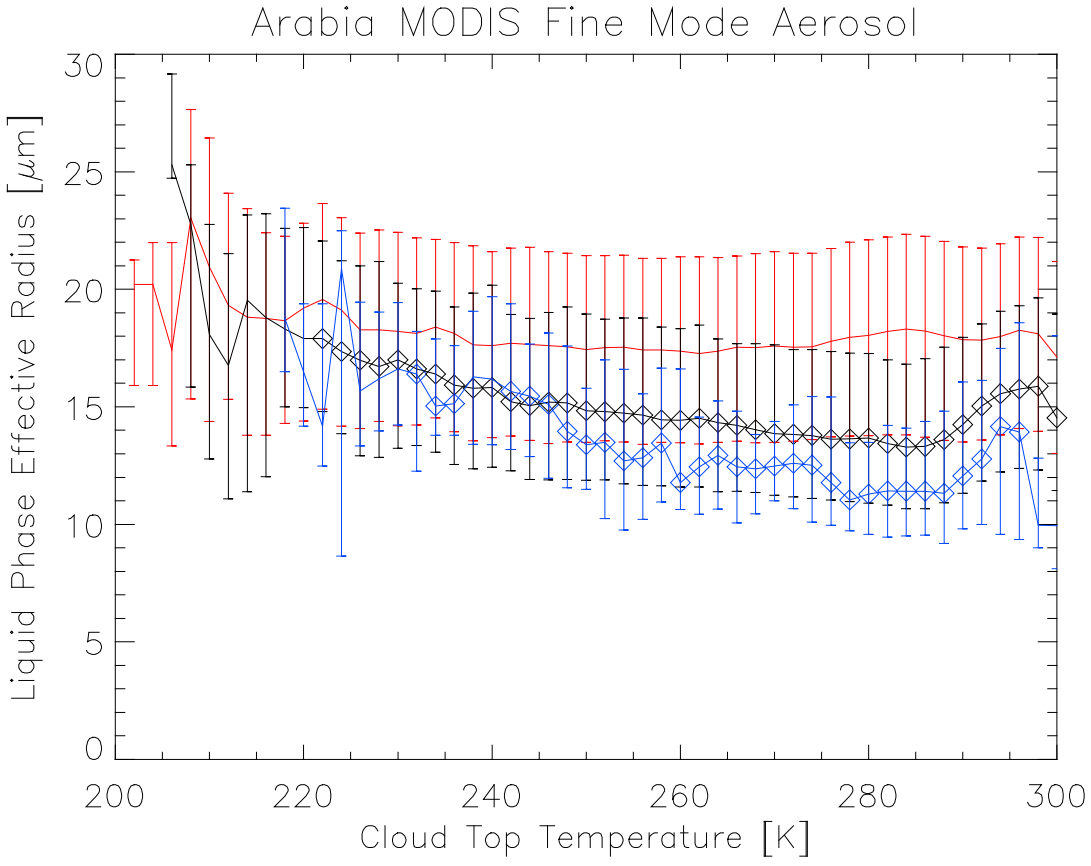

Fig. 28: Liquid water cloud effective radius as a function of CTT for background (red), moderate (black) and high (blue) fine mode aerosol in Arabia. Solid lines represent median while the bars indicate the 20% and 80% quantiles of the respective distribution per CTT bin.

Ice cloud effective radius results from MODIS are very similar to those of liquid water clouds: positive deviations from background in Southern Africa, negative elsewhere. In contrast to liquid water clouds for ice effective radius also statistically significant (at 95% confidence level) deviations are observed in Southern Africa for high mineral dust and total aerosol. In the other regions the effects again are stronger for the fine mode class than for the dust class and the strongest deviations from background are observed for the Maghreb.
The results of the analysis of the IASI observations seem to be a contradiction to the MODIS results at first sight. Instead of being decreased as suggested by the traditional theory, ice crystal effective size of the IASI observations is increased under dusty conditions for all observations. In the case of optically thick clouds the radiance observed by IASI originates from the uppermost cloud layer only as the cloud becomes opaque, whereas for MODIS effective radius retrievals ice absorption deep inside the cloud also contributes to the spectral contrast between visible and near-infrared reflectance and thus to retrieved ice effective radius.
As IASI is sensitive to mineral dust only, the background ice effective radius distribution also includes cloud observations, which may interact with fine mode aerosol (e.g. from biomass burning), tending to decrease droplet (and ice crystal) size of the background sample. So the observed dust effect is the deviation from a potentially not pristine background. On the other hand the dust discrimination of MODIS is not very reliable, thus the “dusty conditions” potentially also include biomass burning contributions, which may reduce ice crystal size counteracting a potential increasing effect from giant mineral dust particles.
Consequently, for ice clouds, it cannot finally be concluded which interpretation of dust effect on ice crystal size may be correct – or if they are both, potentially at different parts of the cloud.
Generally analysis of satellite observations with respect to aerosol-cloud interactions in most cases lack the vertical information required in order to assess the three-dimensional structure of the clouds and aerosol layers. Especially in the case of ice clouds observed effects will not be the same, if the aerosol is entrained at cloud base (i.e. in the boundary layer) and thus already impacts on the liquid phase droplets, or if elevated aerosol layers (e.g. transported mineral dust) are entrained at mid-level, impacting on droplet freezing. With respect to cirrus clouds, especially outflow from deep convective systems, changed cirrus properties under aerosol influence, reflecting the indirect aerosol effects, may be the result of different stages of aerosol cloud interaction (drizzle suppression, early freezing, invigorated convection, stronger cirrus outflow) or only some of them.

9.2 Relationships between aerosol and cloud optical depth

Total cloud optical depth is mainly increased by moderate and high aerosol loads. Nevertheless in the Sahel it is only increased for moderate fine mode and total aerosol, and these increases are furthermore not statistically significant. Especially for mineral dust a decrease of optical depth with aerosol can be observed from MODIS in the Sahel. Although not being significant, decreased optical depth under dusty conditions is also observed by ENVISAT in the Maghreb.
In order to understand the governing principles behind the differences in total cloud optical depth it is important to look into the effects for liquid and frozen cloud phase independently. Liquid phase cloud optical depth is still significantly reduced for

mineral dust in the Sahel and insignificantly for mineral dust in Southern Africa. It is increased elsewhere, partly significantly and partly not.
The theory of the Twomey effect would suggest that with decreasing cloud droplet size (which in fact is observed in the Sahel, also for mineral dust) cloud optical depth should increase. Nevertheless the opposite is observed for Sahelian dust. Fig. 29 shows the optical depth deviation from background conditions depicted against that of liquid water effective radius. Black symbols represent the effects for total aerosol, red ones for dust and blue ones for fine mode aerosol. Total and fine mode aerosol effects are reasonably well linearly correlated (despite the very small sample sizes correlation coefficients are calculated here), which is obviously not the case for mineral dust. Mainly in the mineral dust sample, but also for both other aerosol types two major axes of co-variability can be identified. One in the direction of the classical Twomey effect (lower effective radius increases optical depth) and one in an almost orthogonal direction (lower effective radius and decreased optical depth).

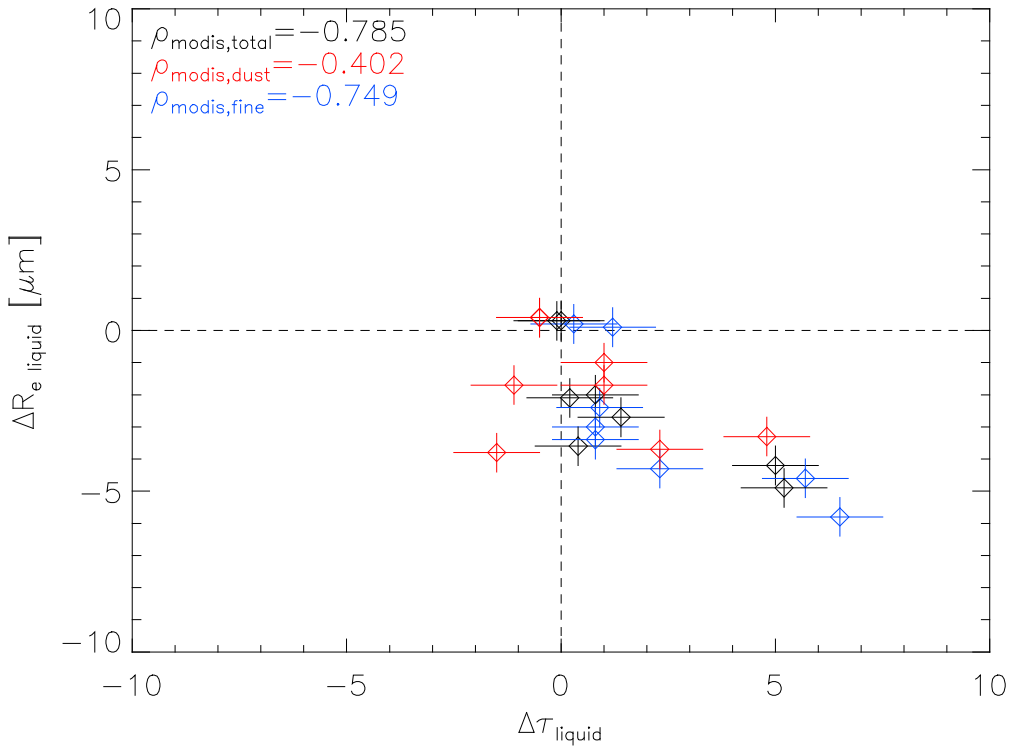

Fig. 29: Liquid phase effective radius effect as function of liquid phase optical depth for the four analysis regions and three aerosol types.

The theory of the Twomey effect relies on the assumption that the liquid water path remains unchanged. Thus for verifying the nature of the detected secondary axis of co-variability the same analysis is performed for the MODIS observations using liquid water path as background projection coordinate rather than CTT.
Fig. 30 shows the liquid water cloud effective radius as a function of liquid water path. It is evident that smallest droplet sizes are connected to small liquid water paths and that the increase of droplet size with increased liquid water path is highest at moderate LWP and for pristine backgroud conditions (red curve in fig. 30).

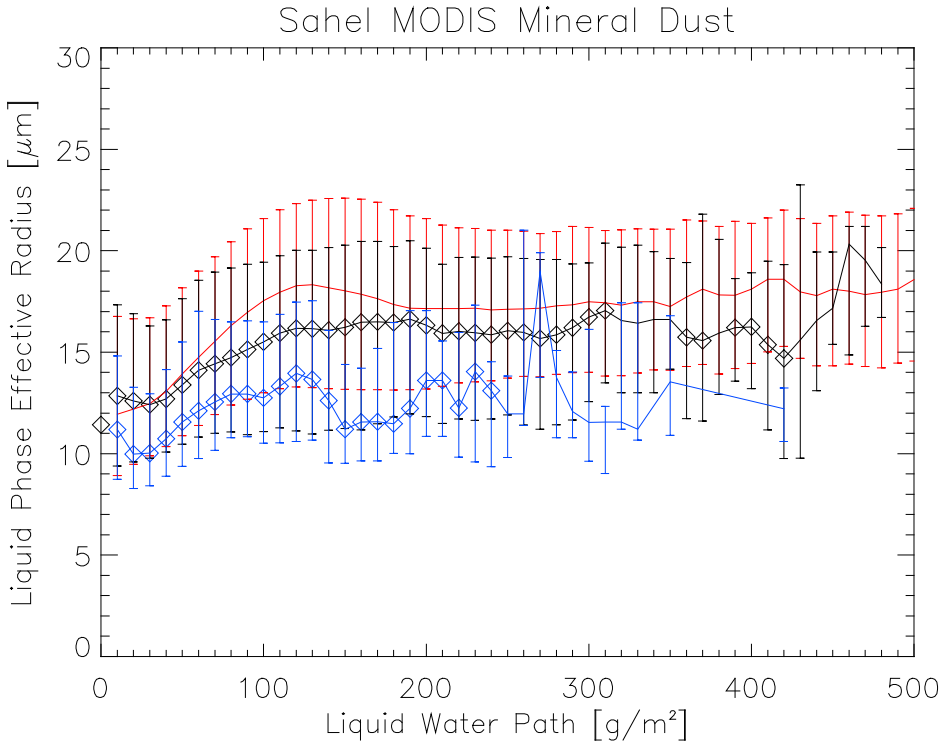

Fig. 30: Median, 20% and 80% quantiles of MODIS observed liquid phase effective radius as function of LWP for background (red), moderate (black) and high (blue) mineral dust in the Sahel.

Fig. 31 is the same as fig. 30 but for cloud optical depth. Also in the Sahel and for mineral dust optical depth is always increased for moderate and high aerosol at the same liquid water path. If the same relationship as in fig. 29 is depicted with analysis performed with liquid water path as background projection coordinate, optical depth and effective radius are highly correlated and the secondary mode of co-variability vanishes (fig. 32), as expected from the LWP definition in eq. (12). Consequently the theory of the Twomey effect is generally also valid for mineral dust in the Sahel. Nevertheless effective radius it is not the only influencing factor for liquid water optical depth. It can thus be concluded from the analysis that the reduction of cloud optical depth as observed in the Sahel is mainly the consequence of reduced LWP under dusty conditions (see Tab. 14) and the only slight increase in optical depth for low LWP due to reduced effective radius is not able to counterbalance the strong reducing effect by the LWP decrease. Consequently effects on cloud lifetime and thus on liquid or ice water path also impact on cloud optical depth and, if the cloud water path is reduced, also decrease the cloud optical depth despite the reduction of droplet sizes.

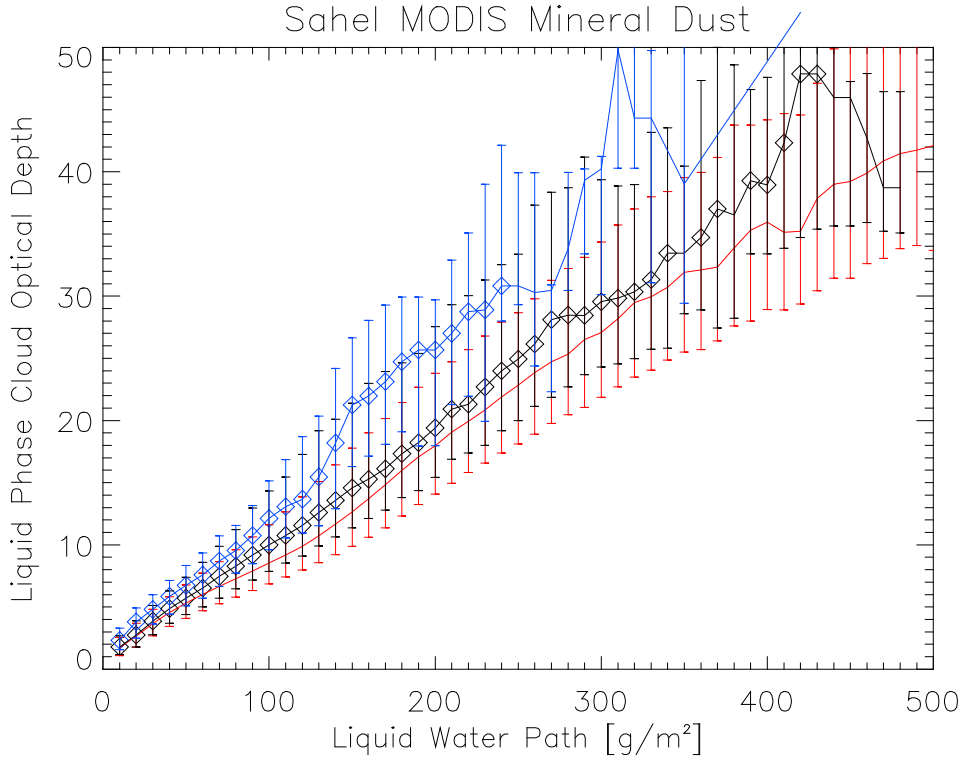

Fig. 31: Median, 20% and 80% quantiles of MODIS observed liquid phase cloud optical depth as function of LWP for background, moderate and high total aerosol in the Sahel.

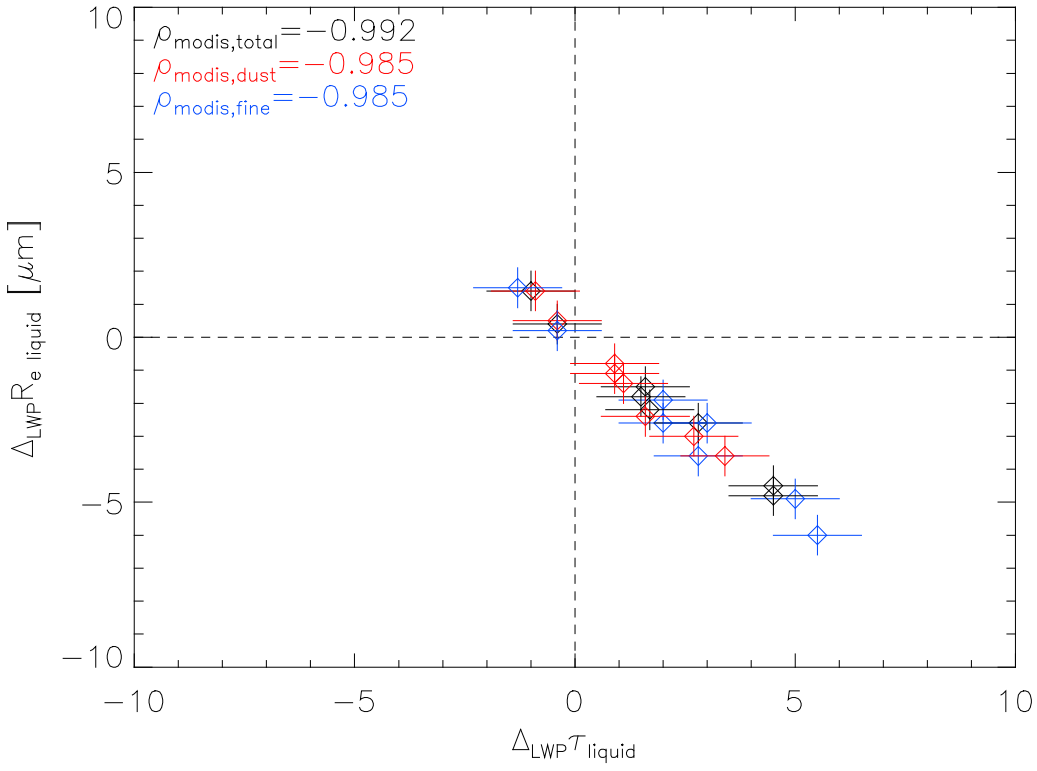

Fig. 32: As fig. 29, but with LWP correction instead of CTT correction.

For ice cloud optical depth generally the same kind of behaviour is seen as for liquid water clouds. Also here optical depth is widely decreased in the Sahel and increased elsewhere. Ice water path is significantly lower under aerosol influence in the Sahel and higher in all other regions. Fig. 33 and fig. 34 show the ice cloud effective radius deviation from background as functions of ice cloud optical depth as obtained from the analysis with CTT and with IWP as projection coordinate, respectively.
As for liquid water clouds, the analysis of MODIS observations with respect to CTT shows two distinct modes of co-variability. One represents the classical Twomey effect and the other one again a decrease of optical depth together with decreasing effective radius and vice versa. Consequently correlations are low for all aerosol types. If deviations from background are evaluated with respect to background IWP, correlations are very high and mainly the Twomey effect is found. But unlike for liquid water clouds the optical depth is also (insignificantly) increased for positive ice effective radius deviations.
The decrease of optical depth observed in the Sahel can be explained by a higher cirrus fraction at low CTT. These cirrus clouds have lower optical depth and lower IWP than the deep convective fraction at the same CTT. Although the cirrus is generally vertically separated from mineral dust layers, and thus is not affected directly by the dust, dust particles can be uplifted into the cirrus layer by deep convective clouds and thus also the outflow cirrus of those systems may be subject to dust interactions. If this is the case here, cannot be answered in detail from the used satellite data.

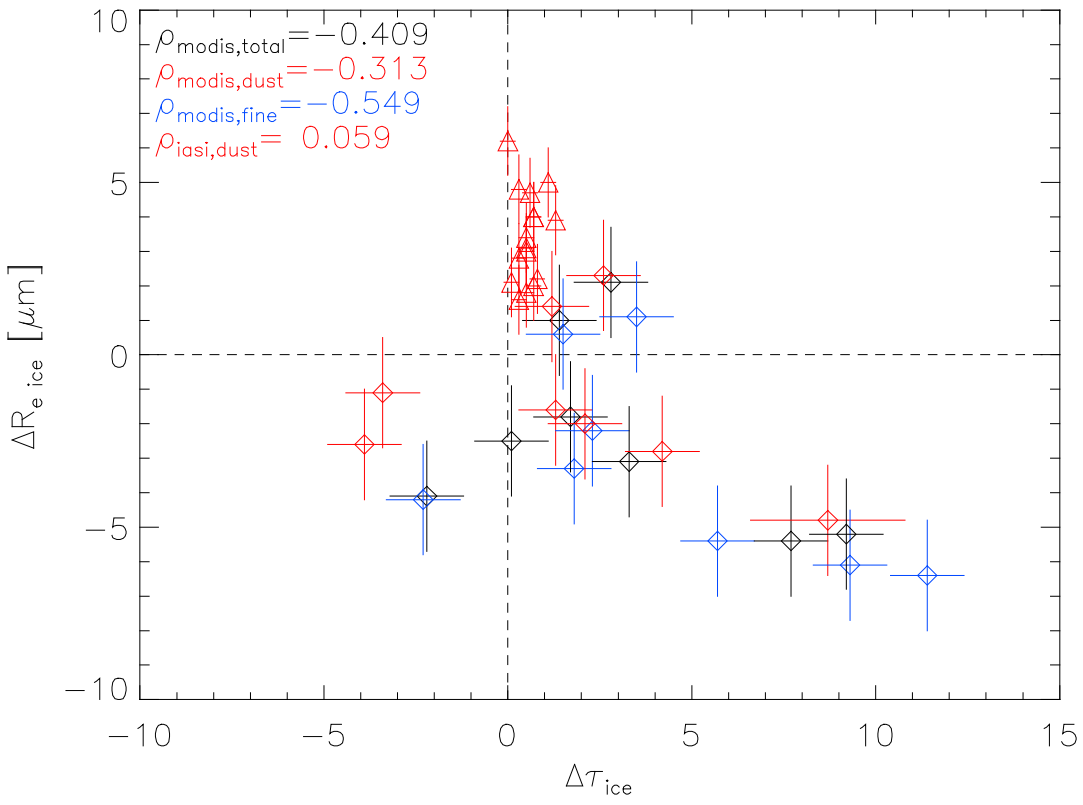

Fig. 33: Ice effective radius effects of MODIS (diamonds) and IASI (triangles) as function of ice optical depth effect for the four regions and different aerosol types.

IASI observations show an increase in ice cloud optical depth in all regions, but with different magnitudes. Moreover, due to the opacity limit of IASI ice cloud optical depth, average optical depths and consequently also deviations from background under dusty conditions are much smaller than obtained from MODIS. The increase in optical depth mainly reflects a decrease of thin cirrus observations under dusty conditions and an increased fraction of optically thicker clouds. Those changes in IWP, potentially controlling optical depth behaviour, are not represented by the IASI observations and thus the observed optical depth effects can be regarded as being generally the result of an increased fraction of optically thicker ice clouds (e.g. deep convective cloud systems).

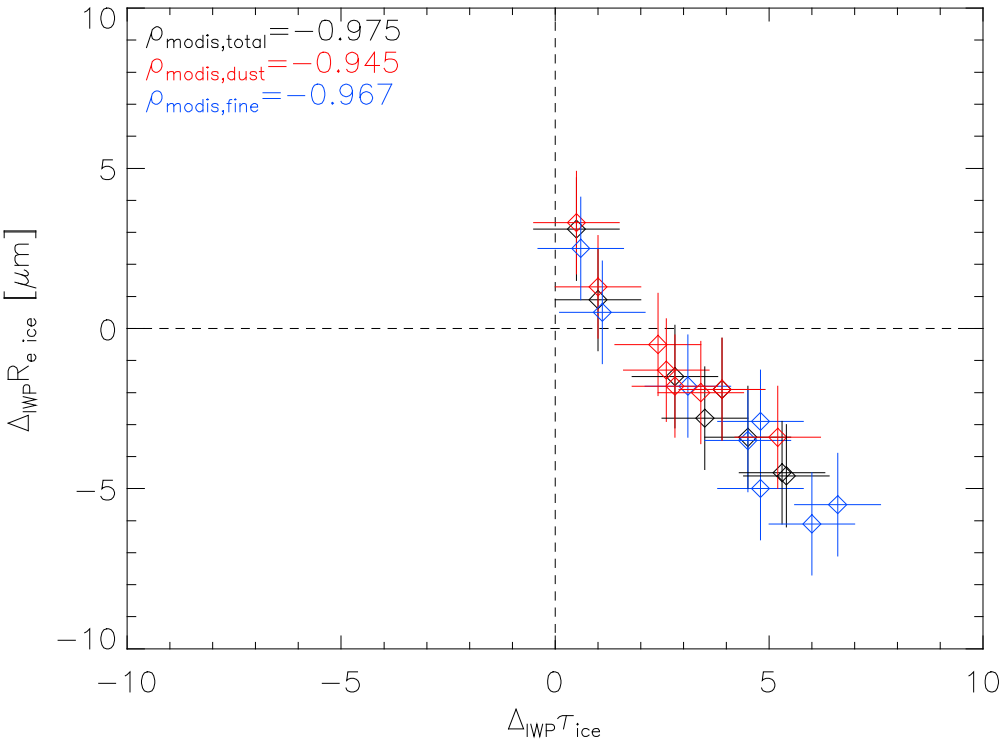

Fig. 34: As fig. 33 but with IWP correction instead of CTT correction (MODIS observations only).

9.3 Cloud lifetime effects

Although the Twomey effect can be confirmed for liquid water and ice clouds from the observations, counteracting effects have been identified, which are strongly related to decreasing LWP and IWP. Cloud cover changes are also important for the radiation balance, they are moreover closely linked to changes in cloud water path. Fig. 35 presents the changes of LWP as a function of liquid phase effective radius deviations from background conditions (from MODIS observations). Again two orthogonal modes of co-variability can be identified.
In one the effective radius dominates the LWP (LWP decreases with decreased effective radius), but also an invigoration mode (LWP is increased or less decreased despite the effective radius reduction). For example in the case of the strongest effective size reductions (observed for fine mode aerosol in Arabia and the Maghreb)

LWP is increased, indicating invigoration of convection by the reduced droplet sizes. Consequently total optical depth is also strongly increased in those cases – by both, smaler droplets and increased cloud liquid water path. The relationship between IWP and ice effective radius deviations from background looks very similar to that of liquid water clouds (fig. 36), it also shows separation in mainly two axes of co-variability. In the Sahel cloud water path (LWP+IWP) is reduced for all aerosol types, in the other three regions reductions in LWP are mostly overcompensated by IWP increases, so that in the end total cloud water path is increased by the aerosol influence. In the classical understanding of the Twomey effect LWP and IWP would not be changed by aerosol interactions, thus ΔLWP and ΔIWP would all be zero at any effective radius change. Fig. 35 and fig. 36 clearly show that this assumption is not realistic in nature and that it is mainly cloud water path (both, liquid water and ice), which determines the resulting optical depth (and thus cloud albedo) effect. Cloud water path changes have many different origins. For example suppressed precipitation and changes in the droplet size distribution impacting on supersaturation levels above droplet surfaces directly influence the cloud water path. Moreover solar heating can increase convective stability and thus suppress initial convection. Nevertheless these feedback mechanisms cannot be confirmed from the satellite datasets used here.

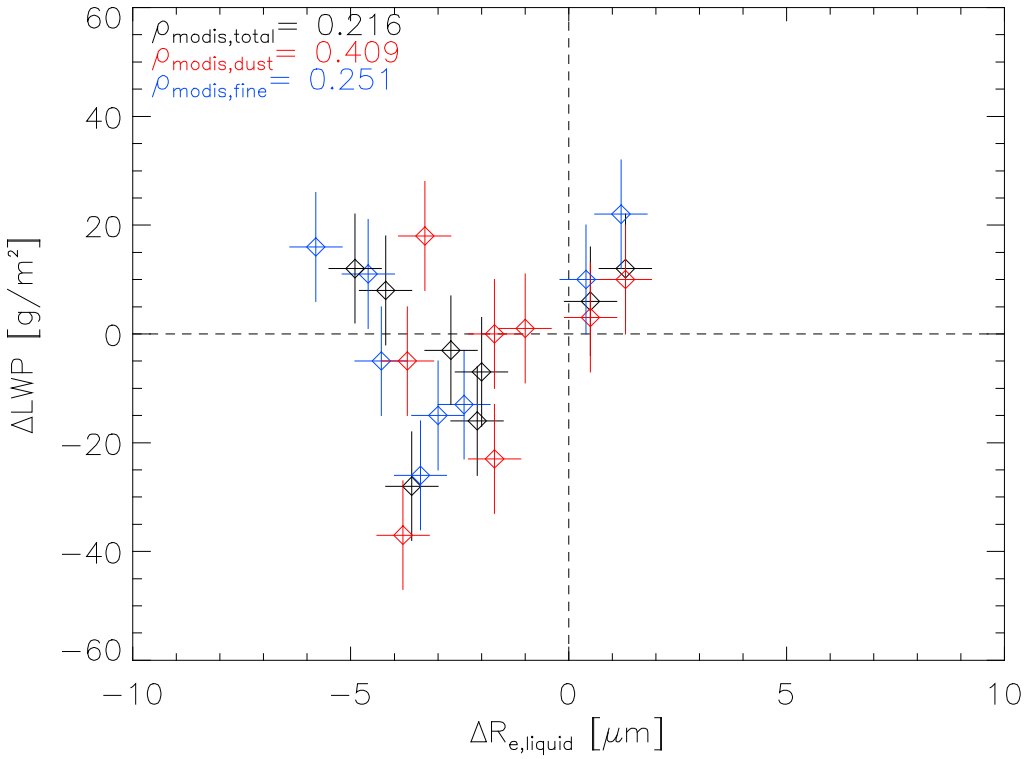

Fig. 35: Liquid water path difference of MODIS as functions of liquid phase effective radius for four analysis regions and three aerosol types.

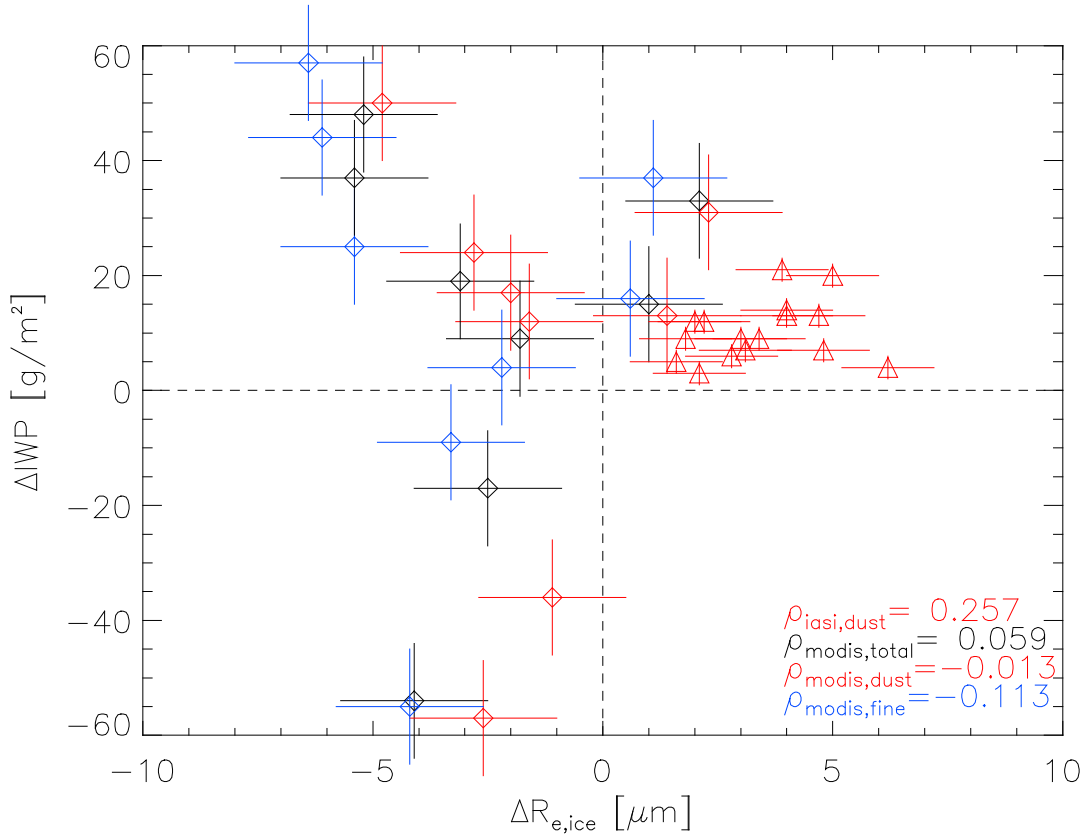

Fig. 36: Ice water path differences of MODIS (diamonds) and IASI (triangles) as function of ice phase effective radius from four analysis regions and three aerosol types.

IASI observations show only increasing IWP in the presence of mineral dust, which is a trivial consequence of the observations of effective radius and optical depth increases. Nevertheless the IASI IWP does not represent the total ice water path for optically thick clouds due to the opacity limit in thermal infrared optical depth retrievals. As for ice cloud optical depth observed with IASI, the IWP increase mainly reflects the larger relative fraction of optically thick clouds in the total IASI ice cloud observations. Moreover, as biomass burning aerosols are much more absorbing than most mineral dust aerosols (depending on the iron oxide fraction of the dust particles), background conditions are also influenced by the fine mode aerosols (as well in terms of cloud droplet or ice crystal size as in terms of reducing convective instability due to solar heating). Thus the IASI background sample cannot be regarded as truely pristine and dust effects have to be seen relative to a background potentially including biomass burning aerosols.
Convective stabilisation through solar heating of the aerosol layer indirectly reduces convective growth and thus cloud water path. Changing freezing levels increase or reduce the amount of latent heat being made available for invigorating convective updrafts. From fig. 35 and fig. 36 it seems that mineral dust is slightly more effective in increasing or decreasing LWP and IWP. But the differences to fine mode aerosol effects are within the uncertainty ranges and moreover the MODIS type selection is not fully reliable. Unfortunately from ENVISAT no cloud water path and effective radius retrievals are available. Thus such a conclusion has to be drawn with great caution from the available data.

Cloud cover is increased under aerosol influence in almost all cases. A clear dependency on AOD very similar to the curves shown e.g. by *Small et al.* (2011) can be seen in MODIS and ENVISAT observations (exemplarily shown for MODIS observations and total aerosol in Southern Africa in fig. 37).
Nevertheless the changes in cloud cover are not correlated with any of the other cloud observables for any of the satellite datasets (neither total nor liquid water or ice clouds only). Also no preferential modes of co-variability can be identified unlike for the other cloud properties shown above. Consequently the cloud cover changes seem to be not directly related with microphysical changes of cloud properties. If they are the result of concurring microphysical and radiative effects, like suggested by *Small et al.* (2011), or if they are the result of increased AOD near clouds or in moister conditions due to swelling of aerosol particles, like suggested by *Stevens and Feingold* (2009), cannot be answered using only satellite data as done here.

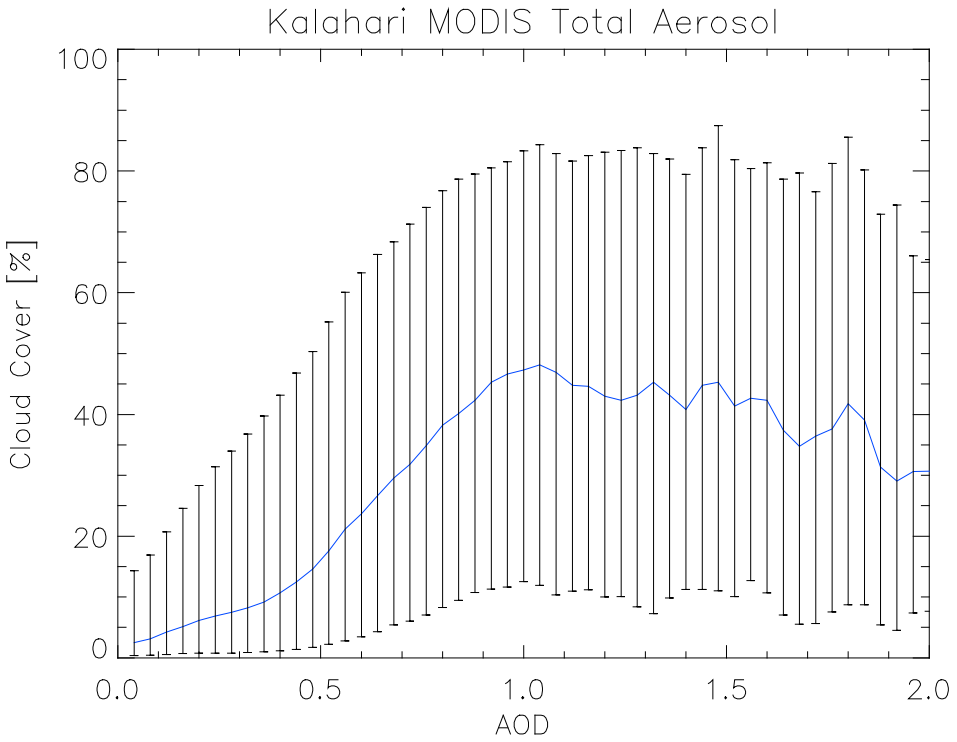

Fig. 37: Total cloud cover as a function of AOD in the Southern African Kalahari domain. The solid line represents median and the bars the 20% and 80% quantiles of the cloud cover distribution for the respective AOD bin.

Either cloud-resolving numerical modeling including microphysical aerosol-cloud-interactions and aerosol-radiation-meteorology interactions would be needed, or other reliable satellite datasets including estimates of the atmospheric radiation balance and temperature and humidity profiles (which are able to account for aerosol effects). Nevertheless from the data so far available it can be definitely excluded that the change of microphysical properties (including cloud water path), and thus the proposed Albrecht effect on cloud lifetime, is the only relevant impacting factor for changes in cloud cover under observations of increased AOD. This conclusion is in good agreement with *Quaas et al.* (2010), who compare MODIS AOD and cloud cover effects with model simulations. In their findings AOD increase due to swelling

under moist conditions is more effective in changing cloud cover then microphysical or other effects.

9.4 Relationships between aerosol and cloud phase

One of the largest uncertainties in aerosol-cloud interactions is whether aerosol influence results in early or in delayed freezing. For both kinds of interactions good arguments and evidence have been presented. From satellite observations it is generally difficult to answer the question, as only cloud top phase can determined with most passive remote sensing methods. Nevertheless the distribution of cloud phase and liquid and ice water path can help to statistically identify the impact of aerosols on cloud phase.

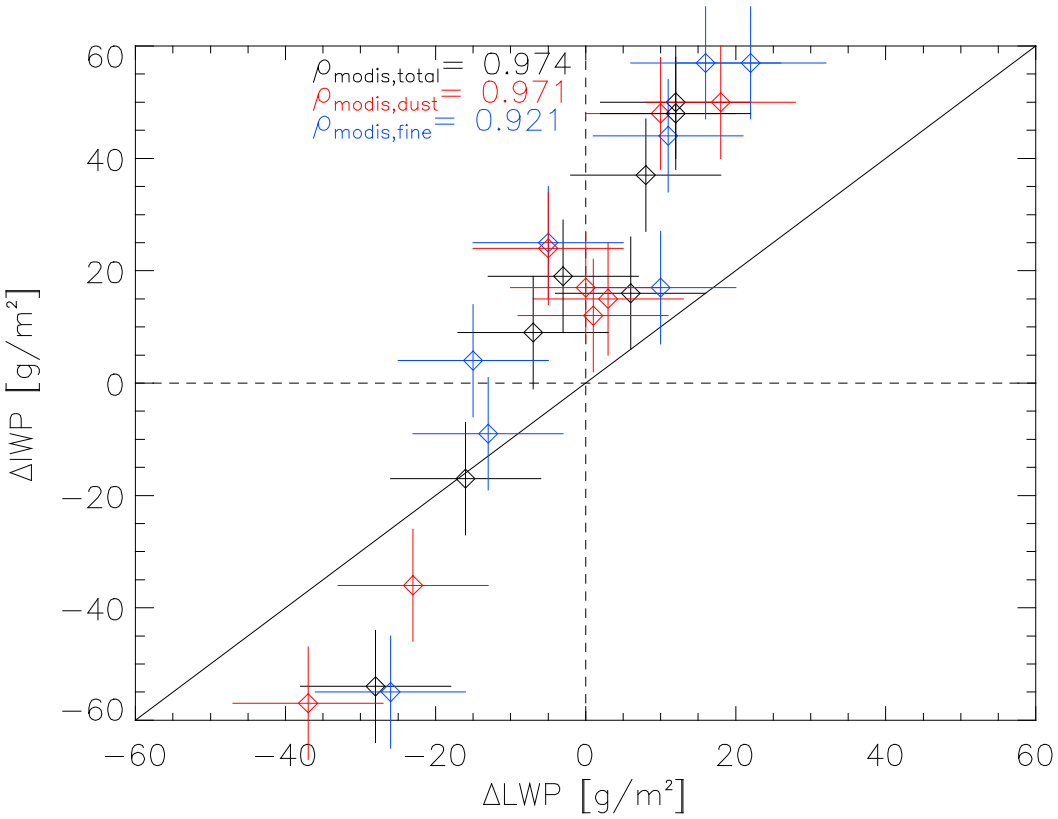

Fig. 38: Ice water path effects compared to liquid water path effects from MODIS observations for three aerosol types and all regions.

In fig. 38 ice water path deviations from background conditions are depicted in relationship to the respective LWP deviations (MODIS observations). The identity line has also been provided for helping to understand the relationships between both. For all points (aerosol effects) above the identity line the ice fraction in the cloud (in terms of condensed cloud water) gains from the liquid fraction, for points below identity vice versa. It is evident that in the majority of cases the ice water path is increased (or less decreased) at the cost of liquid water. Only in cases of strong total cloud water path reductions (all in the Sahel) ice water path is reduced stronger than liquid water path. If this is related to cloud top temperature, it is evident that the IWP reduction is mainly active at low CTT, thus the strongly reduced IWP (at increasing cloud cover) indicates an increase in anvil cirrus observed by MODIS.

If instead of IWP and LWP ice respective liquid water cloud cover is used to estimate the ice and liquid water phase relationships, the result is less clear. It is presented in fig. 39, now for MODIS and ENVISAT observations. In most cases total cloud cover (liquid water plus ice) is increased.
For total aerosol and dust observations from MODIS correlations are negative, but very weak. For MODIS fine mode and all ENVISAT observations (smaller sample size), liquid water and ice cloud cover are well correlated and the gain seems to be on the side of the liquid water clouds now.

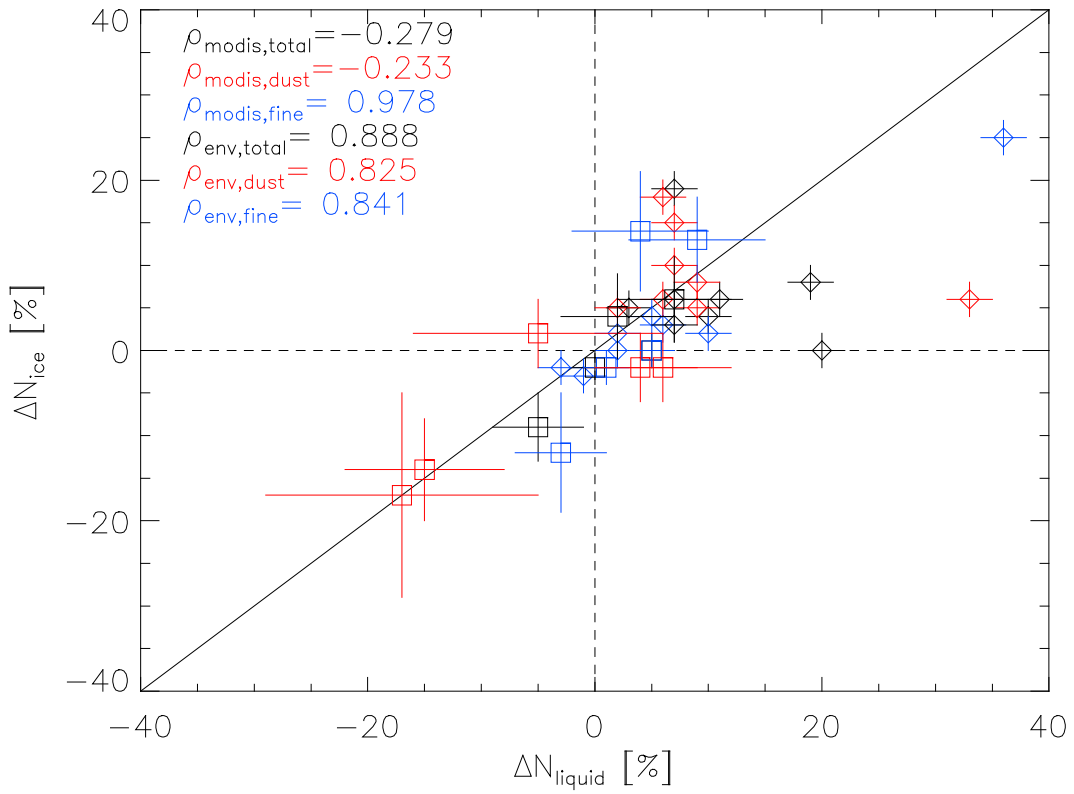

Fig. 39: Ice cloud fraction deviation compared to liquid cloud fraction deviation from MODIS (diamonds) and ENVISAT (squares) observations for three aerosol types and all regions.

IASI observations do not include liquid water clouds, thus effects on the glaciated cloud fraction cannot be inferred from those directly. Nevertheless, for all subsets the strongest increases of ice water path are observed at rather high ice cloud top temperatures, especially between 270K and 240K, thus the temperature range where freezing occurs (fig. 40). Consequently this indirectly provides evidence that glaciation (droplet freezing) sets in more early under dusty conditions than in the background samples, resulting in increased ice cloud effective radii, ice cloud optical depths and thus also ice water path. Nevertheless the IWP increase can also result from biomass burning aerosol effects in the background samples, thus it cannot be regarded as a final proof for invigorated glaciation under dusty conditions.
As a consequence from fig. 38 and fig. 39 it can be concluded that results of aerosol influence on cloud phase always depend on the phase metric to be analysed. In terms of climate and cloud dynamics the use of ice and liquid water path seems to be more relevant, but of course may lead to wrong conclusions due to higher cirrus

fractions. On the other hand using cloud cover as analysis metric does not account for condensed water mass concentrations and thus only reflects binary information about any cloudy satellite observation (water or ice, regardless of cloud depth or cloud water path). From the analysis both arguments (aerosol does not versus aerosol does influence cloud phase) could be supported depending on the definition of the analysis metric.

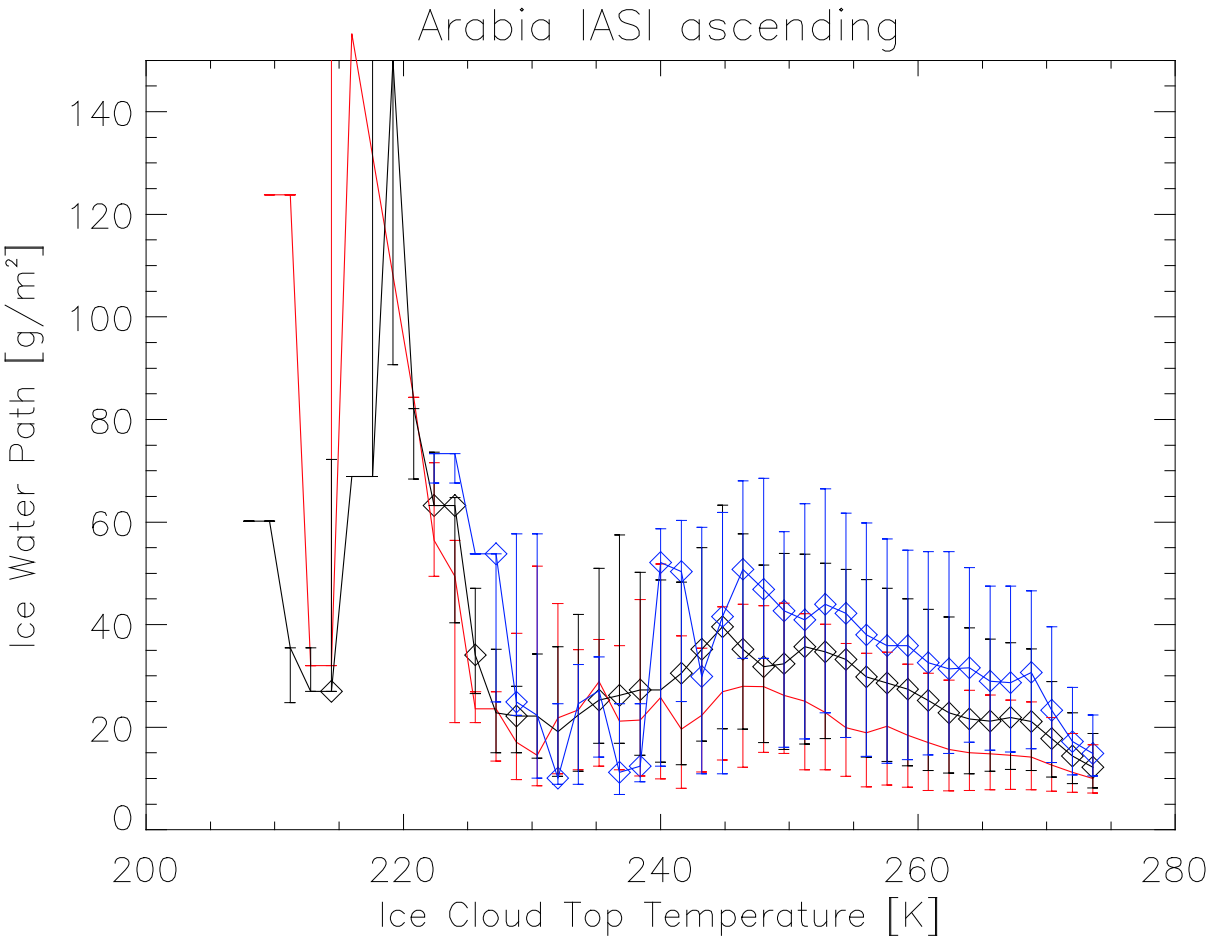

Fig. 40: Median, 20% and 80% quantiles of IASI observed ice water path as function of ice CTT for background (red), moderate (black) and high (blue) mineral dust in Arabia at ascending orbits.

Consequently the question has to be formulated specifically in order to clearly separate if one is interested in the frozen fraction of total condensed water (like is done in laboratory studies, e.g. *Broadley et al.*, 2012) or in glaciated fraction of total cloud cover (like e.g. done in *Ansmann et al.*, 2008). It yet has to be analysed which of the two would be the indirect aerosol effect on ice clouds, which could add relevant information to effects on the radiation balance and thus on climate projections, e.g. in IPCC scenarios. As has been shown that cloud optical depth (and consequently cloud albeso) is mainly constrained by liquid and ice water path, the frozen fraction of total condensed water (i.e. the ratio IWP/CWP) may be of more interest for climate related science – especially as current climate projections only include indirect effects on liquid water clouds.

10 Summary and Conclusions

So far only very few attempts of large scale statistical quantification of indirect aerosol effects over land, and especially over semi-arid or arid regions, from satellite remote sensing are available – and if so, they most often deal with liquid water clouds only (*Stevens and Feingold*, 2009). Nevertheless e.g. *Stevens and Feingold* (2009) identified ice clouds and deep convective cloud systems in subtropical and tropical land regions as being worth to be investigated in detail with respect to indirect aerosol effects. In climate projections of the IPCC so far only the cloud albedo effect for liquid water clouds is included. Also accounting for other indirect aerosol effects, especially on cloud water path, and for ice clouds will help to reduce uncertainties in indirect aerosol climate forcing in the future.
Aerosol and coud observations from three different satellite datasets have been analysed with respect to aerosol cloud interactions over four subtropical semi-arid and arid land regions. For the analysis of ice cloud indirect effects with respect to aerosol type, a new IASI retrieval algorithm for mineral dust has been developed, which is also suitable to retrieve ice cloud physical properties. Moreover a statistical method for data analysis with high sensitivity to aerosol-cloud interactions has been developed and applied.
So far this has been the first attempt to quantify aerosol-cloud interactions

- focussed on semi-arid and arid land regions,
- performing the same kind of analysis to liquid water and ice clouds at the same time with the same methods,
- comparing results from three different independent satellite datasets,
- using advanced statistical descriptions of the observed deviations from background in order to account for non-linearity and multimodal or non-Gaussian probability distributions of cloud properties,
- applying a newly developed method to account for variations in cloud top temperature affecting cloud property observations statistically,
- addressing the relevance of properly selecting the cloud phase metric to be used for inferring relationships between aerosol and cloud phase,
- introducing a newly developed dataset from IASI which is sensitive to desert dust and ice clouds only, adding information about aerosol type sensitivity of aerosol-cloud interactions.

Unfortunately the ENVISAT dataset lacks the retrieval of cloud effective radius, which is the main driver of microphysical changes of cloud properties by aerosols. From the MODIS data the "Twomey effect", an increase of cloud optical depth (and consequently albedo) due to droplet size reduction, could clearly be identified and quantified. Nevertheless cloud optical depth, as well for liquid water clouds as for ice clouds, is also subject to other influencing factors. It could be shown that in the Sahel changes in cloud water path largely impact on the resulting optical depth effect. The cloud water path can be reduced for example by increasing the convective stability due to solar heating of the aerosol layer, or by a higher anvil cirrus fraction as a consequence of invigorated convective updrafts. The first is more relevant for liquid water path and the latter for ice water path. Unfortunately, from the available satellite data it cannot finally be concluded what effect exactly is responsible for the cloud water path reduction in the specific cases. It could be shown that the cloud water path control on optical depth outweighs effective radius effects (Twomey effect) in

overall aerosol impacts on optical depth in the semi-arid and arid land regions analysed here.
It could moreover be shown that the simplification of aerosol impacts on cloud lifetime as formulated in the so-called "Albrecht effect" cannot be confirmed from these satellite data. Although cloud cover is (partly drastically) increased with increasing AOD and the relationship between cloud cover and AOD shows the typical curve also found by other investigations, the corresponding cloud cover deviations from the background state do not show correlation with any of the other cloud properties, especially cloud cover is not correlated with cloud effective radius. If the effect of prolongated cloud lifetime due to smaller droplet sizes and consequently drizzle suppression ("Albrecht effect") would be the reason for the cloud cover increase, these cloud properties should be clearly correlated, or as in the case of effective radius and cloud optical depth, distinct modes of co-variability should be identifiable. This is not the case from the available data. Consequently it can only be speculated, if cloud invigoration due to the pure presence of cloud condensation nuclei may be the reason for the increased cloud cover, or the drizzle suppression effect, or anvil cirrus outflow from deep convective systems, or if the swelling of aerosol under moist conditions just leads to higher observed AOD in conditions with higher cloud cover. Probably combinations of all result in the observed elevated cloud cover for moderate and high aerosol loads.
The MODIS data show an increase in ice fraction on the extent of the liquid fraction in terms of total condensed water, i.e. the ice water path gains on the cost of liquid water path. For mineral dust IASI observations seem to indirectly support this hypothesis as effective radius, optical depth and IWP of ice clouds are increased mainly at relatively high temperatures, i.e. between 240K and 270K. Most studies related to aerosol cloud interactions focus on implications for liquid water clouds. Nevertheless the results of MODIS and IASI observations show that large uncertainties for aerosol influence on ice clouds and deep convection still exist and further efforts are needed to completely understand the effects of especially desert dust on deep convective clouds.
A clear distinction between aerosol types is not evident from MODIS, which reflects the uncertainties in MODIS aerosol type discrimination. In terms of cloud cover, an increase in ice phase fraction is observed neither from MODIS nor from ENVISAT. Also here different contributions, especially cloud formation due to availability of CCN in the boundary layer and increasing cover of anvil cirrus from deep convective systems, may be counteracting parts of the total cloud cover increase, thus the differences are not necessarily related to the glaciation capabilities of the aerosol.
From the above analysis a list of key limitations can be identified, for which the solution of the specific problems will reduce some of the uncertainties presented.
Related to MODIS data, the key limitation is the aggregation of cloud top temperature in the 1°x1° averages. Unlike for effective radius, optical depth and cloud fraction, cloud top temperature is not differenciated between the liquid, ice and undetermined fractions of the cloud field in the gridbox. As especially the relationships between effective radius and optical depth and those of cloud water path rely on separate analysis for each cloud phase, the reprojection with one averaged cloud top temperature clearly results in higher uncertainty, as e.g. for average CTT of 220K still liquid phase cloud properties are available (from a small but not negligable liquid cloud fraction in the gridbox). This limitation can be solved by either using level 2 data (which would drastically increase the data amount to analyse and thus make it nearly impossible to analyse six years over different and large regions) or by including differentiated cloud top temperature into level 3 MODIS products. Moreover

the lack of reliable aerosol type differentiation in the MODIS data is a strong limitation for attributing aerosol effects to different aerosol types. Although the AIRS instrument is operated on the Aqua satellite, thus on the same spacecraft as MODIS, the IASI dust retrieval is not applicable to AIRS data with good quality due to a band gap between 8.2µm and 8.8µm in AIRS channels. Consequently this method cannot be used to identify airborne dust from AIRS.

The limitations of the ENVISAT dataset are mainly the sparse coverage and the incomplete cloud characterisation in APOLLO. The coverage issue is a result of the rather narrow swath of AATSR and the alternating scan mode of SCIAMACHY. Both cannot be changed. Nevertheless the Metop satellite (on which also IASI is operated) provides two similar instruments, AVHRR and GOME-2. The availability of a sufficiently large dataset of SYNAER retrievals from Metop will clearly solve the issue of sparse coverage with ENVISAT. Still for semi-arid and arid regions the "dark target" limitation remains an unsolved issue for the use of SYNAER in this kind of research. The other major limitation of the ENVISAT dataset regards the APOLLO cloud retrieval. Fixed effective radius is assumed in determination of cloud optical depth and moreover a fixed correction factor for ice cloud optical depth is used. This is clearly not sufficiently reliable information for quantification of aerosol-cloud interations. Thus for being able to use the capabilities of SYNAER and APOLLO from Metop, a simulateous retrieval of optical depth and effective radius, separated by ice and liquid water clouds, is clearly needed.

The clearly identifiable major limitations of the IASI dataset are the lack of reliable optical depth and consequently ice water path information for opaque clouds (τ>10), the (current) inability to retrieve liquid water cloud information and the insensitivity to biomass burning aerosols. Although the latter is well appreciated in terms of dust research and aerosol type classification, it is a limitation in terms of aerosol-cloud-interactions research as it is impossible to determine pristine background conditions from IASI. Consequently deviations from estimated background conditions from IASI include information about the deviation of dust affected clouds from clouds under the influence of biomass burning or other fine mode aerosols. It might be generally possible to identify biomass burning aerosols at night from IASI shortwave thermal infrared channels (around 4-5µm), a potential which has to be further investigated in the future. Such information at night together with SYNAER information at day would allow for a reliable identification of pristine background also for IASI observations.

"*We think we want information when we really want knowledge.*"

Silver, 2012

List of Symbols

a	area
AOD	aerosol optical depth
AOD_{IR}	IR aerosol optical depth (evaluated as average over 925cm^{-1} and 1125cm^{-1})
AOD_{VIS}	aerosol optical depth at visible wavelength (0.55µm)
$_b$	index for pristine background conditions
B_ν	Planck function at wavenumber ν
C_i	dust species i
CTT	cloud top temperature
D_e	effective diameter (for ice clouds)
DFS	degrees of freedom for signal
DOF	effective spatial degrees of freedom
E	event in Bayesian inference
f_v	volume fraction of dust size mode
g	assymetry parameter
$_h$	index for high amount of airborne aerosol
$\mathbf{H}$	histogram
$\hat{\mathbf{H}}$	projected histogram
$\Delta\mathbf{H}$	observation density difference
I_λ/I_ν	intensity / radiance at wavelength λ or wavenumber ν
IWP	ice water path
k_e	mass extinction coefficient
k	auxiliary variable for Two-Stream solution of RTE
$\mathbf{K}$	rank correlation matrix
L	maximum length
LWP	liquid water path
$_m$	index for moderate amount of airborne aerosol
$\mathbf{M}$	observation space
$M_\pm$	auxiliary variable for Two-Stream solution of RTE
n(r)	number size distribution
$\mathbf{P}$	2D probability matrix estimate
P_B	Bayesian probability
P_{dust}	probability of accurate dust retrieval
P_s	scattering phase function
P_x	a priori probability in Bayesian inference
P_y	a posteriori probability in Bayesian inference
P_z	false a priori probability in Bayesian inference
Q_e	extinction efficiency
r	radius
r_e	effective radius
r_m	mode radius for lognormal dize distribution
R_x	maximum reflectance in Two-Stream solution of RTE
s	path / distance
S_j	dust size mode j
T	temperature
T_{base}	baseline temperature
T_{dust}	effective dust temperature
T_{sfc}	surface temperature
v	volume
V_i	ith Eigenvector
w_i	weight of ith Eigenvector
$\mathbf{X}$	data matrix
z	vertical path / distance from surface
α	Ångström exponent

β_e	extinction coefficient
β_{scat}	scattering coefficient
δ	multiplicator for EV derived AOD_{IR}
ε_{sfc}	surface emissivity
φ_{comp}	observation estimate of dust species fraction
φ_{max}	probability that dust spectra can be reproduced by V_3-V_8
ϕ	normalized Bayesian probability for dust component and size mode
γ	IR-VIS transfer coefficient for dust AOD
λ	wavelength
Λ_i	i^{th} Eigenvalue
μ	cosine of viewing angle
ν	wavenumber
ρ_{index}	density of medium described by $_{index}$
ρ	Pearson product-moment correlation coefficient
σ	standard deviation
τ	optical depth
τ_a	absorption optical depth (theoretical dust spectra)
τ_e	extinction optical depth (theoretical dust spectra)
τ_{eqv}	equivalent optical depth
τ_{ev}	optical depth observation subspace spanned by Eigenvectors 3-8
τ_{dust}	most likely dust optical depth spectrum
τ_s	scattering optical depth (theoretical dust spectra)
ω_0	single scattering albedo

References

Ackerman, S.A.: Using the Radiative Temperature Difference at 3.7 and 11 μm to Track Dust Outbreaks, Remote Sens. Environ., 27. 129-133, 1989.

Ackerman, S.A.: Remote sensing aerosols using satellite infrared observations, J. Geophys. Res., 102, 17069-17079, 1997.

Ackerman, S.A., Toon, O.B., Stevens, D.E., Heymsfield, A.J., Ramanathan, V., and Welton, E.J.: Reduction of tropical cloudiness by soot, Science, 288, 1042-1047, 2000.

Ackerman, S.A., Kirkpatrick, K.P., Stevens, D.E., and Toon, O.B.: The impact of humidity above stratiform clouds on indirect aerosol climate forcing, Nature, 432, 1014-1017, 2004.

Ackerman, S.A., Holz, R.E., Frey, R., Eloranta, E.W., Maddux, B.C., and McGill, M.: Cloud detection with MODIS, Part II: Validation, Journal of Atmospheric and Oceanic Technology, 25, 1073-1086, 2008.

Adedokun, J.A., Emofurieta, W.O., and Adedeji, O.A.: Physical, Mineralogical and Chemical Properties of Harmattan Dust at Ile-Ife, Nigeria, Theor. Appl. Climatol., 40, 161-169, 1989.

Albrecht, F.: Theoretische Untersuchungen über die Ablagerung von Staub aus strömender Luft und ihre Anwendung auf the Theorie der Staubfilter, Phys. Z., 32, 48-56, 1931.

Albrecht, B. A.: Aerosols, cloud microphysics and fractional cloudiness, Science, 245, 1227-1230, 1989.

Alexander, J.M., Laksina, O., Meland, B., Young, M.A., Grassian, V.-H., and Kleiber, P.D.: A combined laboratory and modeling study of the infrared extinction and visible light scattering properties of mineral dust aerosol, J. Geophys. Res. Atmosp., 118, doi: 10.1029/2012JD018751, 2013.

Alpert, P. and Ziv, B: The Sharav cyclone — Observations and some theoretical considerations. Journal of Geophysical Research, 94, 18495−18514, 1989.

Anderson, E., Bai, Z., Bischof, C., Clackford, S., Demmel, J., Dongarra, J., Du Croz, J., Greenbaum, A., Hammarling, S., McKenney, A., and Sorensen, D.: LAPACK Users‘ Guide, Third EDITION; Society for Industrial and Applied Mathematics, Philadelphia, USA, 1999.

Ansmann, A., Tesche, M, Althausen, D., Müller, D., Seifert, P., Freudenthaler, V., Heese, B., Wiegner, M., Pisani, G., Knippertz, P., and Dubovik, O.: Influence of Saharan dust on cloud glaciation in southern Morocco during the Saharan Mineral Dust Experiment, J. Geophys. Res., 113, D04210, doi:10.1029/2007JD008785, 2008.

Aronson, J.R., Emslie, A.G., Smith, E.M. and Strong, P.F.: Infrared spectra of lunar soils and related optical constants, Proc. Lunar Planet. Sci. Conf. 10th, 1787-1795, 1979.

Aronson, J.R., Emslie, A.G., Miseo, E.V., Smith, E.M., and Strong, P.F.: Optical constants of monoclinic anisotropic crystals: Gypsum, Appl. Opt., 22, 4093-4098, 1983.

Ashpole, I., and Washington, R.:An automated dust detection using SEVIRI: A multiyear climatology of summertime dustiness in the central and western Sahara, J. Geophys. Res., 117, D08202, doi:10.1029/2011JD016845, 2012.

Aumann, H., H.H., DeSouza-Machado, S.G., and Behrangi, A.: Deep convective clouds at the tropopause, Atmos. Chem. Phys., 11, 1167-1176, doi:10.5194/acp-11-1167-2011, 2011.

Bayes, T.: An Essay towards solving a Problem in the Doctrine of Chances, communicated by Mr. Price, in a letter to John Canton, Philosophical Transactions (1683-1775), 53, 370-418, 1763.

Ben-Ami, Y., Koren, I., Rudich, Y., Artaxo, P., Martin, S.T., and Andreae, M.O.: Transport of North African dust from the Bodélé depression to the Amazon Basin: a case study, Atmos. Chem. Phys., 10, 7533-7544, 2010.

Bergeron, T.: On the physics of cloud and precipitation, Mém. de l'Union Géod. Geophys. Int., Lisbon, 1933.

Blumstein, D., Chalon, G., Carlier, T., Buil, C., Hébert, P., Maciaszek, T., Ponce, G., Phulpin, T., Tournier, B., Siméoni, D., Astruc, P., Clauss, A., Kayal, G., and Jegou, R.: IASI instrument: technical overview and measured performances, SPIE Denver, 5543-22, 2004.

Bohren, C.F., and Huffman, D.: Absorption and scattering of lights by small particles, Wiley, New York, 1983.

Bretherton, C.S., Widmann, M., Dymnikov, V.P., Wallace, J.M., and Bladé, I.: The effective number of spatial degrees of freedom of a time-varying field, J. Clim., 12, 1990-2009, 1999.

Brindley, H.E., and Russell, J.E.: Improving GERB scene identification using SEVIRI: Infrared dust detection strategy, Remote Sens. Env., 104, 426-446, 2006.

Bristow, C.S., Drake, N., and Armitage, S.: Deflation in the dustiest place on Earth: The Bodélé Depression, Chad, Geomorphology, 105, 50-58, 2009.

Broadley, S.L., Murray, B.J., Herbert, R.J., Atkinson, J.D., Dobbie, S., Malkin, T.L., Condliffe, E., and Neve, L.: Immersion mode heterogeneous ice nucleation by an illite rich powder representative of atmospheric mineral dust, Atmos. Chem. Phys., 12, 287-307, 2012.

Carboni, E., Thomas, G.E., Sayer, A.M., Siddans, R., Poulsen, C.A., Grainger, R.G., Ahn, C., Antoine, D., Bevan, S., Braak, R., Brindley, H., DeSouza-Machado, S., Deuzé, J.L., Diner, D., Ducos, F., Grey, W., Hsu, C., Kalashnikova, O.V., Kahn, R., North, P.R.J., Salustro, C., Smith, A., Tanré, D., Torres, O., and Veihelmann, B.: Desert dust retrieval intercomparison, Atmos. Meas. Tech. Discuss., 5, 691.-746, 2012.

Carslaw, K.S., Boucher, O., Spracklen, D.V., Mann, G.W., Rae, J.G.L., Woodward, S., and Kulmala, M.: A review of natural aerosol interactions and feedbacks within the earth system, Atmos. Cham. Phys., 10, 1701-1737, 2010.

Caquineau, S., Gaudichet, A., Gomes, L., Magonthier, M.-C., and Chatenet, B.: Saharan dust: Clay ratio as a relevant tracer to assess the origin of soil-derived aerosols, Geophys. Res. Lett., 25, 983-986, 1998.

Chaboureau, J.-P., Tulet, P., and Mari, C: Diurnal cycle of dust and cirrus over West Africa as seen from Meteosat Second Generation satellite and a regional forecast model, Geophys. Res. Lett., 34, L02822, doi:10.1029/2006GL027771, 2007.

Chylek, P., Robinson, S., Dubey, M.K., King, M.D., Fu, Q., and Clodius, W.B. : Comparison of near-infrared and thermal infrared cloud phase detections, J. Geophys. Res., 111, D20203, doi:10.1029/2006JD007140, 2006.

Clancy, R.T., Wolff, M.J., and Christensen, P.R. : Mars Aerosol Studies with the MGS TES Emission Phase Function Observations: Optical Depths, Particle Sizes, and Ice Cloud Types versus Latitude and Solar Longitude, J. Geophys. Res., 108(E9), 5098, doi :10.1029/2003JE002058, 2003.

Clarisse, L., Coheur, P.-F., Prata, F., Hadji-Lazaro, J., Hurtmans, D., and Clerbaux, C.: A unified approach to infrared aerosol remote sensing and type specification, Atmos. Chem. Phys., 13, 2195-2221, 2013.

Comstock, J.M., d'Entremont, R., DeSlover, D., Mace, G.G., Matsorov, S.Y., McFarlane, S.A., Minnis, P., Mitchell, D., Sassen, K., Shupe, M.D., Turner, D.D., and Wang, Z. : An intercomparison of microphysical retrieval algorithms for upper-tropospheric ice clouds, Bull. Am. Meteorolog. Soc., 88,191-204, 2007.

D'Agostini, G.: A multidimensional unfolding method based on Bayes' theorem, Nuclear Instruments and Methods in Physics Research A, 362, 487-498, 1995.

Davidi, A., Koren, I., and Remer, L. : Direct measurements of the effect of biomass burning over the Amazon on the atmospheric temperature profile, Atmos. Chem. Phys., 9, 8211-8221, 2009.

DeMott, P. J., Sassen, K., Poellot, M.R., Baumgardner, D., Rogers, D.C., Brooks, S.D., Prenni, A.J., and Kreidenweis, S.M.: African dust aerosols as atmospheric ice nuclei, Geophys. Res. Lett., 30(14), 1732,doi:10.1029/2003GL017410, 2003.

DeSouza-Machado, S.G., Strow, L.L., Hannon, S.E., abd Motteler, H.E.: Infrared dust spectral signatures from AIRS, Geophys. Res. Lett., 33, L03801, doi :10.1029/2005GL024364, 2006.

DeSouza-Machado, S.G., Strow, L.L., Imbiriba, B., McCann, K., Hoff, R.M., Hannon, S.E., Martins, J.V., Tanré, D., Deuzé, J.L., Ducos, F., and Torres, O.: Infrared retrievals of dust using AIRS: Comparisons of optical depths and heights derived for a North African dust storm to other collocated EOS A-Train and surface observations, J. Geophys. Res., 115, D15201, doi:10.1029/2009JD012842, 2010.

Dubvovik, O., Holben, B., Eck, T.F., Smirnov, A., Kaufman, Y.J., King, M.D., Tanré, D., and Slutsker, I.: Variability of Absorption and Optical Properties of Key Aerosol Types Observed in Worldwide Locations, J. Atm. Sci., 59, 590-608, 2002.

Dufresne, J.-L., Gautier, C., Ricchiazzi, P., and Fouquart, Y.: Longwave scattering effects of mineral aerosols, J. Atmos. Sci., 59, 1959-1966, 2002.

Dunion, P., and Velden, C.S.: The impact of the Saharan Air Layer on Atlantic tropical cyclone activity, Bull. Am. Meteorolog. Soc., 85, 353-365, 2004.

Eastwood, M. L., Cremel, S., Wheeler, M., Murray, B.J., Girard, E., and Bertram, A.K.: Effects of sulfuric acid and ammonium sulfate coatings on the ice nucleation properties of kaolinite particles, Geophys. Res. Lett., 36, L02811, doi:10.1029/2008GL035997, 2009.

Ebert, E.E. and Curry, J.A.: A parametrization of ice cloud optical properties for climate models, J. Geophys. Res., 97, 3831-3836, 1992.

Engelstaedter, S., Tegen, I., and Washington, R.: North African dust emissions andTransport, Earth-Science Reviews, 79, 73-100, 2006.

Evan, A.T., Heidinger, A., and Knippertz, P.: Analysis of winter dust activity off the coast of West Africa using a new 24-year over-water advanced very high resolution radiometer satellite dust climatology, J. Geophys. Res., 111, D12210, doi:10.1029/2005JD006336, 2006.

Evan, A.T., Heidinger, A., and Vimont, D.J.: Arguments against a physical long-term trend in global ISCCP cloud amounts, Geophys. Res. Lett., 34, L04701, doi:10.1029/2006GL028083, 2007.

Feingold, G., Cotton, W.R., Kreidenweis, S.M., and Davies, J.T.: The impact of giant cloud condensation nuclei on drizzle formation in stratocumulus: Implications for cloud radiative properties, J. Atmos. Sci., 56, 4100-4117, 1999.

Feingold, G. Remer, L.A., Ramaprasad, J., and Kaufman, Y.J.: Analysis of smoke impact on clouds in Brazilian biomass burning regions: An extension of Twomey's approach, J. Geophys. Res., 106, 22907-22922, 2001.

Findeisen, W.: Die kolloidgeometrischen Vorgänge der Niederschlagsbildung, Meteor. Z., 55, 121-133, 1938.

Fink, A.H., and Reiner, A.: Spatio-temporal Variability of the Relation between African Easterly Waves and West African Squall Lines in 1998 and 1999, J. Geophys. Res., 108(D11), doi:10.1029/2002JD002816, 2003.

Flamant, C., Knippertz, P., Parker, D.J., Chaboureau, J.-P., Lavaysse, C., Agusti-Panareda, A., and Kergoat, L.: The impact of a mesoscale convective system cold pool on the northward propagation of the intertropical discontinuity over West Africa, Q. J. R. Meteorol. Soc., 135, 139-159, 2009.

Flanigan, D.F. and DeLong, H.P.: Spectral Absorption Characteristics of the Major Components of Dust Clouds, Appl. Opt., 10, 51-57, 1971.

Foner, H.A., and Ganor, E.: The chemical and mineralogical composition of some urban atmospheric aerosols in Israel, Atm. Env., 26B, 125-133, 1992.

Formenti, P., Rajot, J.L., Desboeufs, K., Caquineau, S., Chevaillier, S., Nava, S., Gaudichet, A., Journet, E., Triquet, S., Alfaro, S., Chiari, M., Haywood, J., Coe, H., and Highwood, E.: Regional variability of the composition of mineral dust from western Africa: results from the AMMA SOP0/DABEX and DODO field campaigns, J. Geophys. Res., 113, D00C13, doi:10.1029/2008JD009903, 2008.

Fouquart, Y., Bonnel, B., Brogniez, G., Buriez, J., Smith, L., and Morcrette, J.-J. : Observations of Saharan aerosols : results of ECLATS field experiment : Part II. Broadband radiative characteristics of aerosols and vertical flux divergence, J. Clim. Appl. Meteorol., 26, 38-52, 1987.

Freud, E., Rosenfeld, D., Andreae, M.O., Costa, A.A., and Artaxo,P.: Robust relations between CCN and the vertical evolution of cloud drop size distribution in deep convective clouds, Atmos. Chem. Phys. Discuss., 5, 10155-10195, 2005.

Fu, Q., and Liou, K.N.: Parameterization of the radiative properties of cirrus clouds, J. Atmos. Sci., 50, 2008-2025, 1993.

Gillespie, D.T.: The stochastic coalescence model for cloud droplet growth, J. Atm. Sci., 29, 1496-1510, 1972.

Givati, A., and Rosenfeld, D.: Quantifying precipitation suppression due to air pollution, J. Appl. Meteorol., 43, 1038-1056, 2004.

Givati, A., and Rosenfeld, D.: Separation between Cloud-Seeding and Air-Pollution Effects, J. Appl. Meteorol., 44, 1298-1314, 2005.

Glaccum, R.A., and Prospero, J.M.: Saharan aerosols over the Tropical North Atlantic – Mineralogy, Marine Geology, 37, 295-321, 1980.

Glotch, T.D., Rossman, G.R., and Aharonson, O.: Mid-infrared (5-100µm) reflectance spectra and optical constants of ten phyllosilicate minerals, Icarus, 192, 605-622, 2007.

Göttsche, F.M., and Olesen, F.-S.: Modelling the effect of optical thickness on diurnal cycles of land surface temperature, Remote Sensing of Environment, 113, 2306-2316, 2009.

Haman, K.E.: Physical problems of weather modification, Hydrological sciences - Bulletin - des Sciences Hydrologiques, XXI, 587-602, 1976.

Han, Q., Rossow, W.B., Zeng, J., and Welch, R.: Three Different Behaviors of Liquid Water Path of Water Clouds in Aerosol-Cloud Interactions, J. Atm. Sciences, 59, 726-735, 2002.

Haywood, J., and Boucher, O.: Estimates of the direct and indirect radiative forcing due to tropospheric aerosols: a review, Reviews of Geophysics, 38, 513-543, 2000.

Heidinger, A.K., Rao, V., and Dean, C.: Using MODIS to Estimate Cloud Contamination of the AVHRR Data Record, J. Atmos. Oc. Tech., 19, 586-601, 2002.

Hess, M., Koepke, P., and Schult, I.: Optical Properties of Aerosols and Clouds: The Software Package OPAC, Bull. Am. Meteorolog. Soc., 79, 831-844, 1998.

Heymsfield, A.J., Matsorov, S., and Baum, B.: Ice Water Path-Optical Depth Relationships for Cirrus and Deep Stratiform Ice Cloud Layers, J. Appl. Meteor., 42, 1369-1390, 2003.

Highwood, E., Haywood, J., Silverstone, M., Newman, S., and Taylor, J.: Radiative properties and direct effect of Saharan dust measured by the C-130 aircraft during Saharan Dust Experiment (SHADE): 2. Terrestrial spectrum, J. Geophys. Res., 108(D18), 8578, doi:10.1029/2002JD002552, 2003.

Holben, B.N., Eck, T.F., Slutsker, I., Tanré, D., Buis, J.P., Setzer, K.A., Vermote, E., Reagan, J.A., Kaufman, Y.J., Nakajima, T., Lavenu, F., Jankowiak, I., and Smirnov, A.: AERONET - A Federated Instrument Network and Data Archive for Aerosol Characterization, Remote Sens. Environ., 66, 1-16, 1998.

Holz, R.E., Ackerman, S.A., Nagle, F.W., Frey, R., Dutcher, S., Kuehn, R.E., Vaughan, M.A., and Baum, B.: Global Moderate Resolution Imaging Spectroradiometer (MODIS) cloud detection and height evaluation using CALIOP, J. Geophys. Res., 113, D00A19, doi:10.1029/2008JD009837, 2008.

Holzer-Popp, T., Schroedter-Homscheidt, M., Breitkreuz, H., Martynenko, D., and Klüser, L.: Improvements of synergetic aerosol retrieval for ENVISAT, Atmos. Chem. Phys., 8, 7651-7672, 2008.

Hong, S.: Detection of Asian Dust (Hwangsa) over the Yellow Sea by Decomposition of Unpolarized Infrared Reflectivity, Atm. Env., doi:10.1016/j.atmosenv.2009.08.024, 2009.

Hubanks, P.A., King, M.D., Platnick, S., and Pincus, R.: MODIS atmosphere L3 gridded product algorithm theoretical basis document,
Algorithm Theor. Basis Doc. ATBD-MOD-30, NASA Goddard Space Flight Cent., Greenbelt, Md. (http://modis-atmos.gsfc.nasa.gov/_docs/L3_ATBD_2008_12_04.pdf), 2008.

Hudson, P. K., Young, M. A., Kleiber, P. D., and Grassian, V. H.: Coupled infrared extinction spectra and size distribution measurements for several non-clay components of mineral dust aerosol (quartz, calcite, and dolomite), Atm. Environ., 42, 5991-5999, 2008a.

Hudson, P. K., Gibson, E. R., Young, M. A., Kleiber, P. D., and Grassian, V. H.: Coupled infrared extinction and size distribution measurements for several clay components of mineral dust aerosol, J. Geophys. Res., 113, D01201, doi:10.1029/2007JD008791, 2008b.

Hui, W.J., Cook, B.I., Ravi, S., Fuentes, J.D., and D'Odorico, P.: Dust-rainfall feedbacks in the West African Sahel, Water Resour. Res., 44, W05202, doi:10.1029/2008WR006885, 2008.

Hulley, G.C., Hook, S.J., Manning, E., Lee, S.-Y., and Fetzer, E.: Validation of the Atmospheric Infrared Sounder (AIRS) version 5 land surface emissivity product over the Namib and Kalahari deserts, J. Geophys. Res., 114, D19104, doi:10.1029/2009JD012351, 2009.

Hunt, G.R., and Logan, L.M.: Variation of single particle mid-infrared emission spectrum with particle size, Appl. Opt., 11, 142-147, 1972.

Hsu, N.C., Tsay, S.C., King, M.D., and Herman, J.R.: Aerosol properties over bright reflecting source regions. IEEE Transactions on Geoscience and Remote Sensing, 42, 557-569, 2004.

Hsu, N.C., Tsay, S.-C., King, M.D., and Herman, J.R.: Deep Blue Retrievals of Asian Aerosol Properties Dusring ACE-Asia, IEEE T. Geoscience Rem. Sens., 44, 3180-3195, 2006.

IPCC: Climate Change 2001 - The Scientific Basis: Contribution of Working Group I to the Third Assessment Report of Intergovernmental Panel on Climate Change (IPCC). J. T. Houghton, Y. Ding, D.J. Griggs, M. Noguer, P. J. van der Linden and D. Xiaosu (Eds.), Cambridge University Press, Cambridge, UK, 2001.

IPCC: Climate Change 2007 - The Physical Science Basis: Contribution of Working Group I to the Fourth Assessment Report of the Intergovernmental Panel on Climate Change. Solomon, S., D. Qin, M. Manning, Z. Chen, M. Marquis, K.B. Averyt, M. Tignor and H.L. Miller (Eds.), Cambridge University Press, Cambridge, UK and New York, USA, 2007.

Jalloh, A., Roy-Macauley, H., and Sereme, P.: Major agro-ecosystems of West and Central Africa: Brief description, species richness, management, environmental limitations and concerns, Agric. Ecosyst. Environ., doi:10.1016/j.agee.2011.11.019, 2011.

Jenkins, G.S., Pratt, A.S., and Heymsfield, A.: Possible linkages between Saharan dust and tropical cyclone rain band invigoration in the eastern Atlantic during NAMMA-06, Geophys. Res. Lett., 35, L08815, doi:10.1029/2008GL034072, 2008.

Jeong, G.Y.: Bulk and single-particle mineralogy of Asian dust and a comparison with its source soils, J. Geophys. Res., 113, D02208, doi:10.1029/2007JD008606, 2008.

Jiang, H., and Feingold, G.: Effect of aerosol on warm convective clouds: Aerosol-cloud-surface flux feedbacks in a new coupled large eddy model, J. Geophys. Res., 111, D01202, doi:10.1029/2005JD006138, 2006.

Johnson, B.T., and Osborne, S.R.: Physical and optical properties of mineral dust aerosol measured by aircraft during the GERBILS campaign, Q. J. R. Meteorol. Soc., doi: 10.1002/gj777, 2011.

Kahlaf, F.I., Al-Kadi, A., and Al-Saleh, S.: Mineralogical composition and potential sources of dust fallout deposits in Kuwait, Northern Arabian Gulf, Sedimentary Geology, 42, 255-278, 1985.

Kandler, K., Schütz, L., Deutscher, C., Ebert, M., Hofmann, H., Jäckel, S., Jaenicke, R., Knippertz, P., Lieke, K., Massling, A., Petzold, A., Schladitz, A., Weinzierl, B., Wiedensohler, A., Zorn, S., and Weinbruch, S.: Size distribution, mass consentration and derived optical parameters of the boundary layer aerosol at Tinfou, Morocco, during SAMUM 2006, Tellus, 61B, 32-50, 2009.

Kandler, K., Lieke, K., Benker, N., Emmel, C., Küpper, M., Müller-Ebert, D., Ebert, M., Scheuvens, D., Schladitz, A., Schütz, L., and Weinbruch, S.: Electron microscopy of particles collected at Praia, Cape Verde, during the Saharan Mineral dust experiment: particle chemistry, shape, mixing state and complex refractive index, Tellus B, Accepted Article, doi:10.1111/j.1600-0889.2011.00550.x, 2011.

Kaufman, Y.J., and Nakajima, T.: Effect of Amazon smoke on cloud microphysics and albedo - analysis from satellite imagery, J. Appl. Meteorol., 32, 729-744, 1993.

Kaufman, Y.J., and Fraser, R.S.: The effect of smoke particles on clouds and climate forcing, Science, 277, 1636-1639, 1997.

Kaufman, Y.J., Tanré, D., and Boucher, O.: A satellite view of aerosols in the climate system, Nature, 419, 215-223, 2002.

Kaufman, Y.J., Koren, I., Remer, L.A., Rosenfeld, D., and Rudich, Y.: The effect of smoke, dust and pollution aerosol on shallow cloud development over the atlantic ocean, Proc. Natl. Acad. Sci. U. S. A., 102, 11207-11212, doi:10.1073/pnas.0505191102, 2005.

Kidder, S.Q., and Vonder Haar, T.H.: Satellite Meteorology: an introduction, Academic Press, San Diego, California, USA, 1995.

King, M.D., Tsay, S.-C., Platnick, S.E., Wang, M., and Liou, K.-N.: Cloud Retrieval Algorithms for MODIS: Optical Thickness, Effective Particle Radius, and Thermodynamic Phase, MODIS Algorithm Theor. Basis Doc. ATBD-MOD-05 (http://modis.gsfc.nasa.gov/data/atbd/atbd_mod05.pdf), 1997.

King, M.D., Kaufman, Y.J., Tanré, D., and Nakajima, T.: Remote Sensing of Tropospheric Aerosols from Space: Past, Present, and Future, Bull. Am. Meteorolog. Soc., 80, 2229-59, 1999.

King, M.D., Menzel, W.P., Kaufman, Y.J., Tanré, D., Gao, B.-C., Platnick, S., Ackerman, S.A., Remer, L.A., Pincus, R., and Hubanks, P.A.: Cloud and Aerosol Properties, Precipitable Water, and Profiles of Temperature and Water Vapor from MODIS, IEEE Transactions on Geoscience and Remote Sensing, 41, 442-458, 2003.

Kleiber, P.D., Grassian, V.H., Young, M.A., and Hudson, P.K.: T-matrix studies of aerosol particle shape effects on IR resonance spectral line profiles and comparison with an experiment, J. Geophys. Res., 114, D21209, doi:10.1029/2009JD012710, 2009.

Klüser, L., and Schepanski, K.: Remote sensing of mineral dust over land with MSG infrared channels: A new Bitemporal Mineral Dust Index, Rem. Sens. Environ., 113, 1853-1867, doi:10.1016/j.rse.2009.04.012, 2009.

Klüser, L., Martynenko, D., and Holzer-Popp, T.: Thermal infrared remote sensing of mineral dust over land and ocean: a spectral SVD based retrieval approach for IASI, Atmos. Meas. Tech., 4, 757-773, doi:10.5194/amt-4-757-2011, 2011.

Knippertz, P., and Todd, M.C.: The Central West Saharan dust hot spot and its relation to African easterly waves and extratropical disturbances, J. Geophys. Res., 115, D12117, doi:10.1029/2009JD012819, 2010.

Koike, C., and Shibai, H.: Optical constants of hydrous silicates from 7 to 400μm, Mon. Not. R. astr. Soc., 246, 332-336, 1990.

Kokhanovsky, A.A., and de Leeuw, G. (Eds.): Satellite aerosol remote sensing over land, Springer, Heidelberg & Berlin, Germany, 2009.

Koren, I., Kaufman, Y. J., Washington, R., Todd, M. C., Rudich, Y., Martins, J. V.: The Bodélé depression: A single spot in the Sahara that provides most of the mineral dust to the Amazon forest. Env. Res. Lett., 1, doi:10.1088/1748-9326/1/1/014005, 2006.

Koren, I., Remer, L.A., Kaufman, Y.J., Rudich, Y., and Martins, J.V.: On the twilight zone between clouds and aerosols, Geophys. Res. Lett., 34, doi:10.1029/2007GL029253, 2007.

Koren, I., Oreopoulos, L., Feingold, G., Remer, L.A., and Altaratz, O.: How small is a small cloud?, Atmos. Chem. Phys., 8, 3855-3864, 2008.

Kriebel, K.T., Saunders, R.W., and Gesell, G.: Optical properties of clouds derived from fully cloudy AVHRR pixels, Beitr. Phys. Atmosph., 62, 165-171, 1989.

Kriebel, K.T., Gesell, G., Kästner, M., and Mannstein, H.: The cloud analysis tool APOLLO: improvements and validations, Int. J. Rem. Sens., 24, 2389-2408, 2003.

Laaksonen, A., Korhonen, P., Kulmala, M., and Charlson, R.J.: Modification of the Köhler Equation to Include Soluble Trace Gases and Slightly Soluble Substances, J. Atm. Sci., 55, 853-862, 1998.

Laity, J.: Deserts and desert environments, Environmental systems and global change series, John Wiley & Sons, West Sussex, UK, 2008.

Laksina, O., Young, M.A., Kleiber, P.D., and Grassian, V.H.: Infrared extinction spectra of mineral dust aerosol: Single components and complex mixtures, J. Geophys. Res., 117, D18210, doi: 10.1029/2012JD017756, 2012.

Langmuir, I.: The production of rain by a chain reaction in cumulus clouds at temperatures above freezing, J. Meteor., 5, 175-192, 1948.

Laurent, H., d'Amato, N., and Lebel, T.: How important is the contribution of the Mesoscale Convective Complexes to the Sahelian rainfall?, Phys. Chem. Earth, 23, 629-633, 1998.

Larar, A.M., Smith, W.L., Zhou, D.K., Liu, X., Revercomb, H., Taylor, J.P., Newman, S.M., and Schlüssel, P.: IASI spectral radiance validation inter-comparisons: case study assessment from the JAIVEx field campaign, Atmos. Chem. Phys., 10, 411-430, 2010.

Legrand, M., Plana-Fattori, A., and N'doume, C.: Satellite detection of dust using the IR imagery of Meteosat, 1. Infrared Difference Dust Index. J. Geophys. Res., 106(D16), 18251-18274, 2001.

Levy, R.C., Remer, L., Matoo, S., Vermote, E.F., and Kaufman, Y.J.: Second-generation operational algorithm: Retrieval of aerosol properties over land from inversion of Moderate Resolution Imaging Spectroradiometer spectral reflectance, J. Geophys. Res., 112, D13211, doi:10.1029/2006JD007811, 2007.

Levy, R.C., Remer, L.A., Kleidman, R.G., Mattoo, S., Ichoku, C., Kahn, R., and Eck, T.F.: Global evaluation of the Collection 5 MODIS dark target aerosol products over land, Atmos. Chem. Phys., 10, 10399-10420, 2010.

Li, J., Zhang, P., Schmit, T. J., Schmetz, J. and Menzel, W. P.: Quantitative monitoring of a Saharan dust event with SEVIRI on Meteosat-8, Int. J. Remote Sens., 28, 2181-2186, 2007.

Lohmann, U., and Feichter, J.: Global indirect aerosol effects: a review, Atmos. Chem. Phys., 5, 715-737, 2005.

Longtin, E.R., Shettle, E.P., Hummel, J.R., and Pryce, J.D.: A wind dependent aerosol model: Radiative properties, AFGL-TR-88-0112, 105 pp., Air Force Geophys. Lab., Air Force Syst. Command, Hanscom Air Force Base, Mass., 1988.

Markl, G.: Minerale und Gesteine, Spektrum Akademischer Verlag, Heidelberg, Germany, 2008.

Martynenko, D., Holzer-Popp, T., Elbern, H., and Schroedter-Homscheidt, M.: Understanding the aerosol information content in multi-spectral reflecance measurements using a synergetic retrieval algorithm, Atmos. Meas. Tech., 3, 1589-1598, 2011.

Marzo, G.A., Blanco, A., De Carlo, F., D'Elia, M., Fonti, S., Marra, A.C., Orofino, V., and Politi, R.: The optical constants of gypsum particles as analog of Martian sulfates, Adv. Space Res., 33, 2246–2251, 2004.

Mathon, V., Laurent, H., and lebel, T.: Mesoscale convective system rainfall in the Sahel, J. Appl. Meteor., 41, 1081-1092, 2002.

Matsui, T., Masunaga, H., Kreidenweis, S.M., Pielke Sr., R.A., Tao, W.-K., Chin, M., and Kaufman, Y.J.: Satellite-based assessment of marine low cloud variability associated with aerosol, atmospheric stability, and the diurnal cycle, J. Geophys. Res., 111, D17204, doi:10.1029/2005JD006097, 2006.

McConnell, C. L., Highwood, E.J., Coe, H., Formenti, P., Anderson, B., Osborne, S., Nava, S., Desboeufs, K., Chen, G., and Harrison, M.A.J.: Seasonal variations of the physical and optical characteristics of Saharan dust: Results from the Dust Outflow and Deposition to the Ocean (DODO) experiment, J. Geophys. Res., 113, D14S05, doi:10.1029/2007JD009606, 2008.

McFarquhar, G.M., and Heymsfield, A.J.: The definition and significance of an effective radius for ice clouds, J. Atmos. Sci., 55, 2039-2052, 1998.

Meerkötter, R., König, C., Bissoli, P., Gesell, G., and Mannstein, H.: A 14-year European Cloud Climatology from NOAA/AVHRR data in comparison to surface observations, Geophys. Res. Lett., 31, L15103, doi:10.1029/2004GL020098, 2004.

Menke, W.: Geophysical Data Analysis: Discrete Inverse Theory, Academic Press, Waltham, MA, U.S.A, 2012

Merchant, C.J., Embury, O., Le Borgne, P., and Bellec, B. : Saharan dust in nighttime thermal imagery : Detection and reduction of related biases in retrieved sea surface temperature, Remote Sens. Env., 104, 15-30, 2006.

Miller, S.D., Kuciauskas, A.P., Liu, M., Ji, Q., Reid, J.S., Breed, D.W., Walker, A.L., and Mandoos, A.A.: Haboob dust storms of the southern Arabian Peninsula, J. Geophys. Res., 113, D01202, doi:10.1029/2007JD008550, 2008.

Mishchenko, M.I., and Travis, L.D.: Capabilities and limitations of a current FORTRAN implementation of the T-matrix method for randomly oriented, rotationally symmetric scatterers, J. Quant. Spectrosc. Radiat. Transfer, 60, 309-324, 1998.

Mogili, P.K., Yang, K.H., Young, M.A., Kleiber, P.D., and Grassian, V.H.: Environmental aerosol chamber studies of extinction spectra of mineral dust aerosol components: Broadband IR-UV extinction spectra, J. Geophys. Res., 112, D21204, doi:10.1029/2007JD008890, 2007.

Mogili, P. K., Yang, K. H., Young, M. A., Kleiber, P. D., and Grassian, V. H.: Extinction spectra of mineral dust aerosol components in an environmental aerosol chamber: IR resonance studies, Atm. Environ., 42, 1752-1761, 2008.

Möhler, O., Benz, S., Saathoff, H., Schnaiter, M., Wagner, R., Schneider, J., Walter, S., Ebert, V., and Wagner, S.: The effect of organic coating on the heterogeneous ice nucleation efficiency of mineral dust aerosols, Environ. Res. Lett., 3, doi:10.1088/1748-9326/3/2/025007, 2008.

N'Tchayi Mbourou, G., Bertrand, J.J., and Nicholson, S.E.: The diurnal and seasonal cycles of wind-borne dust over Africa north of the equator, J. Appl. Meteorology, 36, 868-882, 1997.

Nakajima, T., and King, M.D.: Determination of the Optical Thickness and Effective Particle Radius of Clouds from Reflected Solar Radiation Measurements. Part I: Theory, J. Atm. Sciences, 47, 1878-1893, 1990.

O'Neill, N.T., Eck, T.F., Smirnov, A., Holben, B.N., and Thulasiraman, S.: Spectral discrimination of coarse and fine mode optical depth, J. Geophys. Res., 108(D17), 4559-4573, doi:10.1029/2002JD002975, 2003.

Ogawa, K., Schmugge, T., Jacob, F., and French, A.: Estimation of land surface window (8-12µm) emissivity from multi-spectral thermal infrared remote sensing – A case study in a part of Sahara desert, Geophys. Res. Lett., 30, doi:10.1029/2002GL016354, 2003.

Orofino, V., Blanco, A., Fonti, S., Marra, A.C., and Polimeno, N.: The complex refractive index of limestone particles: an extension to the FIR range for Mars applications, Planetary and Space Science, 50, 839-847, 2002.

Painemal, D. and Zuidema, P.: Assessment of MODIS cloud effective radius and optical thickness retrievals over the Southeast Pacific with VOCALS-Rex in situ measurements, J. geophys. Res., 116, D24206, doi:10.1029/2011JD016155, 2011.

Pavolonis, M.J., and Heidinger, A.K.: Daytime cloud overlap detection from AVHRR and VIIRS, J. Appl. Meteorol., 43, 762-778, 2004.

Pavolonis, M.J., Heidinger, A.K., and Sieglaff, J.: Automated retrievals of volcanic ash and dust cloud properties from upwelling infrared measurements, J. Geophys. Res. Atmos., 118, 1-23, 2013.

Pearson, E.S., and Hartley, H.O. (eds.): Biometrika tables for statisticians, vol. 1,2, University Press, Cambridge, UK, 1972.

Perlwitz, J., and Miller, R.L.: Cloud cover increase with increasing aerosol absorptivity: A counterexample to the conventional semidirect aerosol effect, J. Geophys. Res., 115, D08203, doi:10.1029/2009JD012637, 2010.

Petty, G.W.: A first course in atmospheric radiation, second edition, Sundog Publishing, Madison, Wisconsin, USA, 2006.

Peyridieu, S., Chédin, A., Tanré, D., Capelle, V., Pierangelo, C., Lamquin, N., and Armante, R. : Saharan dust infrared optical depth and altitude retrieved from AIRS : a focus over North Atlantic – comparison to MODIS and CALIPSO, Atmos. Chem. Phys., 10, 1953-1967, doi:10.5194/acp-10-1953-2010, 2010.

Pierangelo, C., Chédin, A., Heiliette, S., Jacquinet-Husson, N., and Armante, R.: Dust altitude and infrared optical depth from AIRS, Atmos. Chem. Phys., 4, 1813-1822, doi:10.5194/acp-4-1813-2004, 2004.

Pruppacher, H.R., and Klett, J.D.: Microphysics of Clouds and Precipitation, Kluwer Academic Publishers, Dordrecht, The Netherlands, 1996.

Quaas, J., Stevens, B., Stier, P., and Lohmann, U.: Interpreting the cloud cover – aerosol optical depth relationship found in satellie data using a general circulation model, Atmos. Chem. Phys., 10, 6129-6135, 2010.

Quenzel, H. and Müller, H.: Optical Properties of Single Mie Particles: Diagrams of Intensity- Extinction- Scattering- and Absorption Efficiencies, Wiss. Mit. Nr. 34, Universitaet Muenchen, 59pp., 1987.

Querry, M.R., Optical constants of minerals and other materials from the millimetre to the ultraviolet, 331pp., U.S. Army, Aberdeen, Md., 1987.

Ramanathan, A., Crutzen, P.J., Kiehl, J.T., and Rosenfeld, D.: Aerosols, climate, and the hydrological cycle, Science, 294, 2119-2124, 2001.

Rashki, A., Eriksson, P.G., Rautenbach, C.J. de W., Kaskaoutis, D.G., Grote, W., and Dykstra, J.: Assessment of chemical and mineralogical characteristics of airborne dust in the Sistan region, Iran, Chemosphere, doi:10.1016/j.chemosphere.2012.06.059, 2012.

Remer, L.A., Tanré, D., and Kaufman, Y.J.: Algorithm for remote sensing of tropospheric aerosol from MODIS: Collection 005, Algorithm Theor. Basis Doc. ATBD-MOD-02, NASA Goddard Space Flight Cent., Greenbelt, Md.
(http://modis.gsfc.nasa.gov/data/atbd/atbd_mod02.pdf), 2006.

Riemer, N., and Wexler, A.S.: Droplets to Drops by Turbulent Coagulation, J. Atm. Sci., 62, 1962-1975, 2005.

Rodgers, C.D.: Inverse methods for atmospheric sounding, Theory and practice, in: Series on Atmospheric, Oceanic and Planetary Physics, vol. 2, World Scientific Publishing, Singapore, 2000.

Rosenfeld, D., and Lensky, I.M.: Satellite-based insights into precipitation formation processes in continental and maritime convective clouds, Bull. Am. Meteorol. Soc., 79, 2457-2476, 1998.

Rosenfeld, D., Rudich, Y., and Lahav, R.: Desert dust suppressing precipitation: a possible desertification feedback loop, Proc. Natl. Acad. Sci. U.S.A., 98, 5975-5980, 2001.

Rosenfeld, D.: Aerosol-cloud interactions control of earth radiation and latent heat release budgets, Space Sci. Rev., 125, 149-157, 2006a.

Rosenfeld, D., Kaufman, Y.I., and Koren, I.: Switching cloud cover and dynamical regimes from open to closed Benard cells in response to the suppression of precipitation by aerosols, Atmos. Chem. Phys., 6, 2503-2511, 2006b.

Rosenfeld, D., and Lensky, I.M.: Clouds-Aerosols-Precipitation Satellite Analysis Tool (CAPSAT), Atmos. Chem. Phys., 8, 6739-6753, 2008.

Roush, T., Pollack, J., and Orenberg, J.: Derivation of midinfrared (5-25µm) optical constants of some silicates and palagonite, Icarus, 94, 191-208, doi:10.1016/0019-1035(91)90150-R, 1991.

Rudich, Y., Sagi, A., and Rosenfeld, D.: Influence of the Kuwait oil fire plume (1991) on the microphysical development of clouds, J. Geophys. Res., 108, doi:10.1029/2003JD003472, 2003.

Ryder, C.L., Highwood, E.J., Rosenberg, P.D., Trembath, J., Brooke, J.K., Bart, M., Dean, A., Crosier, J., Dorsey, J., Brindley, H., Banks, J., Marsham, J.H., McQuaid, J.B., Sodemann, H., and Washington, R.: Optical properties of Saharan dust aerosol and contribution from the coarse mode as measured during the Fennec 2011 aircraft campaign, Atmos. Chem. Phys., 13, 303-325, 2013.

Salisbury, J.W., and Wald, A.: The role of volume scattering in reducing spectral contrast of reststrahlen bands in spectra of powdered minerals, Icarus, 96, 121-128, 1992.

Sassen, K., and Khvorostyanov, V.I.: Cloud effects from boreal forest fire smoke: evidence for ice nucleation from polarization lidar data and cloud model simulations, Environ. Res. Lett., 3, doi:10.1088/1748-9326/3/2/025006, 2008.

Saunders, R.W., and Kriebel, K.T.: An improved method for detecting clear sky and cloudy radiances from AVHRR data, Int. J. Remote Sens., 123-150, 9, 1988.

Schepanski, K., Tegen, I., Laurent,B., Heinold, B., and Macke, A.: A new Saharan dust source activation frequency map derived from MSG-SEVIRI IR channels, Geophys. Res. Lett., 34, L18803, doi:10.1029/2007GL030168, 2007.

Schönwiese, C.-D.: Praktische Statistik für Meteorologen und Geowissenschaftler, 4. Aufl., Gebr. Bornträger, Stuttgart, Germany, 2006.

Seemann, S.W., Borbas, E.E., Knuteson, R.O., Stephenson, G.R., and Huang, H.-L.: Development of a global infrared land surface emissivity database for application to clear sky sounding retrievals from multispectral satellite radiance measurements, J. Appl. Meteor., 47, 108-123, 2008.

Sekiguchi, M., Nakajima, T., Suzuki, K., Kawamoto, K., Higurashi, A., Rosenfeld, D., Sano, I., and Mukai, S.: A study of the direct and indirect effects of aerosols using global satellite data

sets of aerosol and cloud parameters, J. Geophys. Res., 108(D22), 4699, doi:10.1029/2002JD003359, 2003.

Shao, L., Li, W., Yang, S., Shi, Z., and Lü, S.: Mineralogical characteristics of airborne particles collected in Beijing during a severe Asian dust storm period in spring 2002, Sci. China Ser. D: Earth Sci., 50, 953-959, 2007.

Shenk, W.E., and Curran, R.J.: The detection of dust storms over land and water with satellite visible and infrared measurements, Mon. Weather rev., 102, 830-837, 1974.

Silver, N.: The Signal and the Noise, The Penguin Press, New York, New York, U.S.A, 2012

Sirocko, F., Garbe-Schönberg, D., and Devey, C.: Processes controlling trace element geochemistry of Arabian Sea sediments during the last 25,000 years, Global and Planetary Change, 26, 217-303, 2000.

Skonieczny, C., Bory, A., Bout-Roumazeilles, V., Abouchami, W., Galer, S.J.G., Crosta, X., Stuut, J.-B., Meyer, I., Chiapello, I., Podvin, T., Chatenet, B., Diallo, A., and Ndiaye, T.: The 7-13 March 2006 major Saharan outbreak: Multiproxy characterization of mineral dust deposited on the West African margin, J. geophys. Res., 116, D18210, doi:10.1029/2011JD016173, 2011.

Small, J.D., Chuang, P.Y., Feingold, G., and Jiang, H.: Can aerosol decrease cloud lifetime?, Geophys. Res. Lett., 36, L16806, doi:10.1029/2009GL038888, 2009.

Small, J.D., Jiang, J.H., Su, H., and Zhai, C.: Relationship between aerosol and cloud fraction over Australia, Geophys. Res. Lett., 38, L23802, doi:10.1029/2011GL049404, 2011.

Sokolik, I.N., Toon, O.B., and Bergstrom, R.W.: Modeling the radiative characteristics of airborne mineral aerosols at infrared wavelengths, J. Geophys. Res., 103, D8, 8813-8826, 1998.

Sokolik, I.N., and Toon, O.B.: Incorporation of mineralogical composition into models of the radiative properties of mineral aerosol from UV to IR wavelengths, J. Geophys.Res., 104, D8, 9423-9444, 1999.

Spearman, C.: The method of “right and wrong cases” (constant stimuli) without Gauss' formulae, British Journal of Psychology, 2, 227−242, 1908.

Spitzer, W.G., and Kleinman, D.A.: Infrared lattice bands of quartz, Phys. Rev., 121, 1324-1335, doi:10.1103/PhysRev.121.1324, 1961.

Stevens, B. and Feingold, G.: Untangling aerosol effects on clouds and precipitation in a buffered system, Nature, 461, 607-613, doi:10.1038/nature08281, 2009

Thomas, M., Gautier, C., and Richiazzi, P.: Investigations of the March 2006 African dust storm using ground-based column integrated high spectral resolution infrared (8-13µm) and visible aerosol optical thickness measurements: 1. Measurement procedures and results, J. Geophys. Res., 114, D11202, doi:10.1029/2008JD010928, 2009.

Turner, D.D.: Ground-based infrared retrievals of optical depth, effective radius, and composition of airborne mineral dust above the Sahel, J. Geophys. Res., 113, D00E03, doi:10.1029/2008JD010054, 2008.

Twomey, S.: Pollution and the planetary albedo, Atmos. Environ., 8, 1251-1256, 1974.

Twomey, S.: The influence of pollution on the shortwave albedo of clouds, J. Atmos. Sci., 34, 1149-1152, 1977.

Volz, F.E.: Infrared optical constants of ammonium sulphate, sahara dust, volcanic pumice, and flyash, Appl. Optics, 12, 564-568, 1973.

Vonnegut, B.: The nucleation of ice formation by silver iodide, J. Appl. Phys. 18, 593, doi:10.1063/1.1697813, 1947.

Wald, A.E., and Salisbury, J.W.: Thermal infrared directional emissivity of powdered quartz, J. Geophys. Res., 100, 24665-24675, 1995.

Wagner, R., Ajtai, T., Kandler, K., Lieke, K., Linke, C., Müller, T., Schnaiter, M., and Vragel, M.: Complex refractive indices of Saharan dust samples at visible and near UV wavelengths: a laboratory study, Atmos. Chem. Phys., 12, 2491–2512, 2012.

Wang, S., Wang, Q., and Feingold, G.: Turbulence, condensation, and liquid water transport in numerically simulated nonprecipitating stratocumulus clouds, J. Atmos. Sci., 60, 262-278, 2003.

Warner, J.J., and Twomey, S.: The production of cloud nuclei by cane fires and their effect on cloud droplet concentration, J. Atmos. Sci., 24, 704-706, 1967.

Warner, J.J.: A reduction in rainfall associated with smoke from sugarcane fires - An inadvertent weather modification?, J. Appl. Meteorol. 7, 247-251, 1968.

Weinzierl, B., Petzold, A., Esselborn, M., Wirth, M., Rasp, K., Kandler, K., Schütz, L., Koepke, P., and Fiebig, M.: Airborne measurements of dust layer properties, particle size distribution and mixing state of Saharan dust during SAMUM 2006, Tellus, 61B, 96-117, 2009.

Yang, P., and Liou, K.N.: Light scattering by hexagonal ice crystals: Comparison of finite difference time domain and geometric optics models, J. Opt. Soc. Am. A, 12, 162-176, 1995.

Yang, P., Wei, H., Huang, H.-L., Baum, B.A., Hu, Y.X., Kattawar, G.W., Mishchenko, M.I., and Fu, Q.: Scattering and absorption property database for nonspherical ice particles in the near- through far-infrared spectral region, Appl. Opt., 44, 5512-5523, 2005.

Yang, P., Feng, Q., Hong, G., Kattawar, G.W., Wiscombe, W.J., Mishchenko, M.I., Dubovik, O., Laszlo, I., and Sokolik, I.N.: Modelling of the scattering and radiative properties of nonspherical dust-like aerosols, Journal of Aerosol Science, 38, 995-1014, 2007.

Yuan, T., Remer, L.A., Pickering, K.E., and Yu, H.: Observational evidence of aerosol enhancement of lightning activity and convective invigoration, Geophys. Res. Lett., 38, L04701, doi:10.1029/2010GL046052, 2011.

Zhang, P., Lu, N., Hu, X., and Dong, C.: Identification and physical retrieval of dust storm using three MODIS thermal IR channels, Global Planet. Change, 52, 197-206, 2006.

Danksagung

Jedes Mal wenn ein neuer Weltklimabericht veröffentlicht wird, wird wieder einmal deutlich wie wenig wir Menschen doch über den Einfluss kleinster Partikel, eben der Aerosole, auf den Bewölkungszustand auf Skalen von tausenden von Kilometern wissen. Ebendiese Erstreckung der Phänomene über solch grundverschiedene Skalen macht die Thematik der Aerosol-Wolke-Wechselwirkungen so komplex, aber auch so spannend. In den letzten Jahren hatte ich das große Glück, an der Universität Augsburg und am Deutschen Zentrum für Raumfahrt im Rahmen dieser Doktorarbeit an dieser Thematik mitarbeiten zu dürfen.
Daher ist es an der Zeit, all jenen zu danken, die maßgeblichen Anteil am Gelingen dieses Vorhabens hatten.

Mein Dank gilt Herrn Prof. Dr. Michael Bittner für die Betreuung meiner Promotion sowie Herrn Prof. Dr. Siegfried Horn für die Begutachtung der Arbeit sowie seine Begleitung des Promotionsverfahrens von beginn an.

Ich möchte Herrn Dr. Thomas Holzer-Popp ganz besonders danken, für die fachliche Begleitung der Dissertation ebenso wie für die gute und produktive Zusammenarbeit, die vielen Diskussionen und Anregungen sowie die sehr positive Arbeitsatmosphäre.

Dem gesamten Team „Aerosole und Strahlung“ möchte ich danken für die vielfältigen Anregungen und Diskussionen sowie die Hilfsbereitschaft und Zusammenarbeit.

Meinem Kollegen Dmytro Martynenko, mit dem ich seit Beginn meiner Tätigkeit am DLR das Büro teile, danke ich ganz besonders für die gute Zusammenarbeit, für die angenehme Arbeitsatmosphäre und für die vielen, vielen Diskussionen über physikalische und mathematische Probleme, die einen sehr großen Anteil hatten am Werden dieser Arbeit.

Ich möchte all den vielen Kollegen am DLR und an anderen Institutionen danken, die mich im verlaufe der Arbeit unterstützt haben, die durch die vielen Diskussionen und Gespräche neue Ideen hervorgerufen haben, und die dafür gesorgt haben, dass die Arbeit viel Spaß und Freude bereitet.

Auch der Helmholtz-Gemeinschaft und ihrem Doktorandenprogramm „EOS“ bin ich zu Dank verpflichtet, war es doch dieses Programm, das meinen Weg auf die Fährte der Aerosol-Wolken-Wechselwirkungen lenkte.

Zu guter Letzt möchte ich mich noch bei meinen Eltern bedanken, dass sie mir nie Steine in den Weg gelegt haben, und meine Ausbildung gefördert und unterstützt haben, wo immer es nötig war.

ISSN 1434-8454

ISRN DLR-FB--2014-22